23 April 2025

Collision-energy calibration and monochromatisation studies at FCC-ee

The energy calibration, polarisation and monochromatisation working group

A. Blondel (editor)[1,2], J. Keintzel (editor)[3], J. Wenninger (editor)[3], G. Wilkinson (editor)[3,4], G.N. Arango[5], J. Bauche[3], D.P. Barber[6], A. Bogomyagkov[7], C. Carli[3], F. Carlier[3], Z. Duan[8], A. Faus-Golfe[9], D. Gaskell[10], E. Gianfelice-Wendt[11], E. Granados[3], M. Hofer[3], W. Hofle[3], P. Janot[3], R. Kieffer[3], C. Kiel[12], I. Koop[7], M. Koratzinos[14], T. Lefevre[3], A. Martens[9], N. Muchnoi[7], S. Nikitin[7], I. Nikolaev[7], K. Oide[2,3,13], T. Pieloni[12], P. Raimondi[11], S.M. Saenz[5,9], D. Sagan[15], D. Shatilov[7], R. Tomás[3], J. Tamazirt[9], E. Torrence[16], Y. Wu[14], Z. Zhang[8,9], and F. Zimmermann[3]

[1]LPNHE, Sorbonne University, Paris, France
[2]DPNC, University of Geneva, Switzerland
[3]CERN, Meyrin, Switzerland
[4]University of Oxford, UK
[5]UNAL, Bogota, Colombia
[6]Deutsches Elektronen-Synchrotron DESY, Hamburg, Germany
[7]Affiliated with an institute formerly covered by a cooperation agreement with CERN
[8]IHEP, Beijing, China
[9]IJCLab, Orsay, France
[10]JLab, Newport News, USA
[11]Fermilab, Batavia, USA
[12]EPFL, Lausanne, Switzerland
[13]KEK, Tsukuba, Japan
[14]Paul Scherrer Institute PSI, Villigen, Switzerland

[15]Newman Laboratory, Cornell University, Ithaca, USA
[16]University of Oregon, Eugene, USA

Abstract

The Future Circular Collider (FCC) technical and financial Feasibility Study (FS) includes a work package on Energy Calibration, Polarisation and Monochromatisation (EPOL), which is concerned with the precision determination of the centre-of-mass energy at the e^+e^- machine, FCC-ee. To achieve this goal it is proposed to use resonant depolarisation and possibly spin precession measurements, in conjunction with precise measurement by the detectors of the energy spread and other parameters with physics events. Beam diagnostics, provided by polarimeters and beam-position monitors, play an essential role in monitoring the polarisation level and controlling numerous beam parameters at the interaction point. Specific items of accelerator equipment include polarisation wigglers and depolarising RF-kickers. The target is to achieve a precision commensurate to the remarkable statistical precision achievable in the physics experiments. The possible monochromatisation of colliding beams in view of a measurement of the $e^+e^- \to H(125)$ process is also being studied, with the specific requirements of this procedure under investigation. A review is presented of the status of these activities at the end of the FS, together with the outlook for future work.

Contents

1 Introduction

This document is a supporting note to the discussion on the calibration of the FCC-ee collision energy that can be found in Volumes 1 and 2 of the Final Report of the Feasibility Study [1, 2]. The key sections of the Feasibility Study are also presented here, together with more extensive information on critical aspects of the calibration procedure and strategy. A status report is also given for monochromatisation studies directed at facilitating a measurement of the electron Yukawa coupling.

2 Overview

Excellent knowledge of the collision energy, E_{CM}, is vital for many of the most important measurements that will be performed at FCC-ee, in particular the determination of the Z-resonance parameters, and the mass and width of the W boson. To achieve this goal requires calibrating the mean energy of each beam around the ring, E_{b}, in principle not identical for electrons and positrons but here designated with a single symbol for simplicity. The collision energy E_{CM} can then be calculated, provided there is sufficiently good knowledge of the crossing angle of the two beams and all effects that give rise to local shifts of the energy at each interaction point.

Circular colliders have the unique attribute that transverse polarisation naturally accumulates through the Sokolov–Ternov effect, and the closed orbit spin tune, which is the ratio of the spin precession frequency to the revolution frequency, is, to first order, directly proportional to E_{b}. The closed-orbit spin tune can be directly measured by the procedure of resonant depolarisation (RDP), in which the frequency of a depolarising kicker magnet is adjusted until the polarisation is found to vanish. This technique, which has an intrinsic relative precision of 10^{-6} or better, has been exploited at many facilities, most notably at LEP in scans of the Z resonance [3] and more recently at VEPP4 in the determination of the J/ψ and ψ(2S) masses [4]. Alternatively, in a free spin precession (FSP) measurement the depolariser may be used to rotate the spin vector into the horizontal plane, and the precession frequency measured directly. The self-polarisation of the beams can be used for these measurements, but this will only be possible for Z-pole operation and at energies up to and including the W^+W^- threshold. At energies higher than these, the polarisation level will be too small for RDP and FSP measurements to be practical and the energy scale will have to be determined from physics processes at the experiments, such as $e^+e^- \to Z(\gamma)$, ZZ and W^+W^- production. Here, the Z and W masses measured with high precision at lower energies with RDP provide a calibation that can then be applied at higher energies.

The calculation of E_{CM} at each interaction point requires good knowledge of the crossing angle of the two beams, which must be measured by the experiments in real time. In addition, it is necessary to account for local energy variations from synchrotron radiation, the RF system and impedance, and to consider the effects of opposite-sign vertical dispersion.

The knowledge of E_{b} at LEP was ultimately limited by the sampling rate of RDP measurements, which were performed outside physics operation with a periodicity of around once per week. The energy was found to vary significantly between measurements due to several effects, for example earth tides and stray ground electric currents [3]. In order to enable the

much greater degree of systematic control that the vastly larger event samples at FCC-ee warrant, the operational strategy will be very different to LEP. Measurements of E_{b} will be performed several times per hour on non-colliding pilot bunches. In Z running, around 160 pilot bunches will be injected at start of fill, and wiggler magnets will be activated to speed up the polarisation time. One to two hours will be required for the polarisation to build, after which the wigglers will be turned off and physics (colliding) bunches injected. The RF frequency will be continually adjusted to keep the beams centred in the quadrupoles, thus suppressing tide-driven energy changes, which would otherwise be $\mathcal{O}(100\,\mathrm{MeV})$. A model will be developed to track residual energy variations between measurements.

3 Optics Design

The spin-modulation index is defined as

$$B = \frac{\nu_0 \sigma_E}{Q_s} \tag{1}$$

with the closed-orbit spin tune ν_0, the energy spread σ_E and the synchrotron tune Q_s. It quantifies the strength of synchrotron side bands in proximity to the closed-orbit spin tune. At a given beam energy the closed-orbit spin tune is purely defined by the beam energy and a natural constant. RDP can only be successfully performed if this index is sufficiently low, namely $B \lesssim 1.5$. Ideally this index is as low as 1.2 to 1.4. This gives, for a constant spin tune and energy spread, an upper limit on the acceptable synchrotron tune, which must be respected in the optics design.

For the FCC-ee- Z-pole measurements $\nu_0 = 103.48$, $\sigma_E = 3.9 \times 10^{-4}$ for low intensity ($\approx 10^{10}$ particles per bunch) pilot bunches, and $Q_s = 0.0288$, yielding a spin modulation index of 1.4. Assuming the same bunch intensity and, thus, energy spread, this limits the synchrotron tune to values greater than 0.02691.

At W-pair-production with $\sim$80 GeV beam energy, $\nu_0 = 181.55$ and $\sigma_E = 7.0 \times 10^{-4}$, which constrains the lower limit of the synchrotron tune to be approximately 0.0847. In the current optics design $Q_s = 0.081$ and thus the spin modulation index is 1.56, which could reduce the accuracy of RDP measurements at W-energy, compared to the Z-pole. RDP measurements at $\sim$80 GeV beam energy would benefit from a lower synchrotron tune than currently foreseen in the latest optics design.

4 Beam polarisation and optimisation

4.1 Introduction

Statistically, the emission of one in every 10^{10} photons through synchrotron radiation (SR) leads to a spin flip of the electron or positron. It has been found in Ref. [5, 6] that the probability of the occurrence of spin flip depends slightly on the initial spin state of the electron (positron), which leads to a maximum theoretical polarisation of 92.4 % anti-parallel (parallel) to the dipole magnetic field in lepton storage rings. When polarised, the leptons precess, with the spin precession under electromagnetic fields being described by the T-BMT

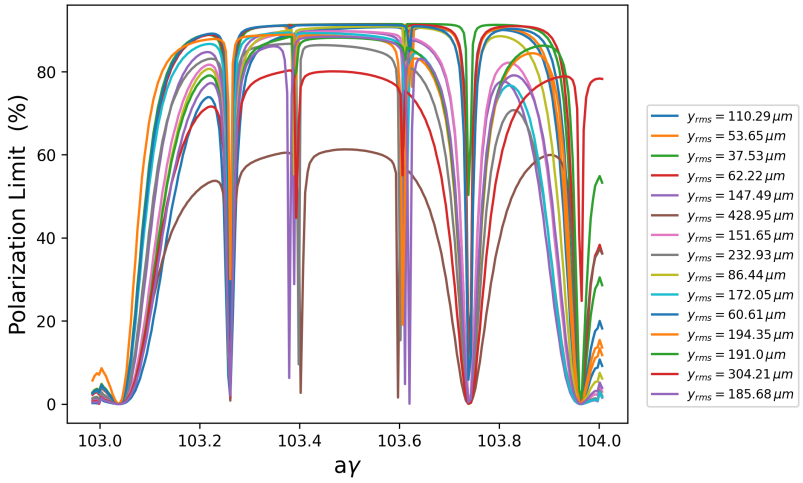

Figure 1: First order energy scan at an energy near the Z ($a\gamma = 103.48$) using Bmad [9].

equation [7, 8] with ν_0 being the number of precessions on the closed orbit, which is named the closed-orbit spin tune. In an error-free flat machine without synchrotron radiation, $\nu_0 = a\gamma$, where $a = (g-2)/2$ is the gyromagnetic anomaly and γ is the Lorentz factor. Nevertheless, the correspondence between the measured spin precession frequency using RDP and the actual beam energy will be broken by machine imperfections and energy saw tooth, which will impact the accuracy of energy determination. These systematic biases are currently being studied.

4.2 Resonances

Depolarisation happens at spin-orbit resonances when the spin precession is coherent with the perturbations from synchro-betatron oscillations

$$\nu_0 = k + k_x Q_x + k_y Q_y + k_s Q_s \quad \text{with} \quad k, k_x, k_y, k_s \in \mathbb{Z} \ , \tag{2}$$

where Q_x, Q_y are the horizontal and vertical betatron tunes and Q_s is the synchrotron tune. Meanwhile, the attainable equilibrium polarisation is restricted by the level of orbit distortions. In presence of vertical orbit distortions the invariant spin axis gets tilted, resulting in depolarisation effects [10, 11]. Figure 1 shows the first-order equilibrium polarisations near Z energy using 15 error seeds which induce different levels of vertical orbit distortion. These error seeds are created from an effective model where truncated Gaussian distributions are utilised to apply small random misalignments ($\sigma_{\mathrm{dx,dy,ds}} = 200\,\mathrm{nm}$) and angular deviations ($\sigma_{\mathrm{d}_\theta,\mathrm{d}_\phi,\mathrm{d}_\psi} = 2\,\mu\mathrm{rad}$) to all quadrupoles, sextupoles and dipoles. No orbit or optics corrections are applied [9]. As shown in Fig. 1, strong depolarisation occurs near first-order spin-orbit resonances, i.e. where Eq. (2) is fulfilled and the polarisation is almost 0. Furthermore, the attainable polarisation level at nominal energy ($\nu_0 = 103.48$) is lower with increasing rms vertical closed orbit deviation. Excellent orbit and optics corrections are, therefore, required for achieving a sufficient level of polarisation. Future studies aim to predict the polarisation level after proper orbit correction and optics tuning, and determine the maximum acceptable

closed orbit for achieving a sufficient level of polarisation, which itself remains to be defined. Complementary, recent progress of the optics tuning working group is reported in [12].

4.3 Harmonic spin bumps for depolarisation reduction

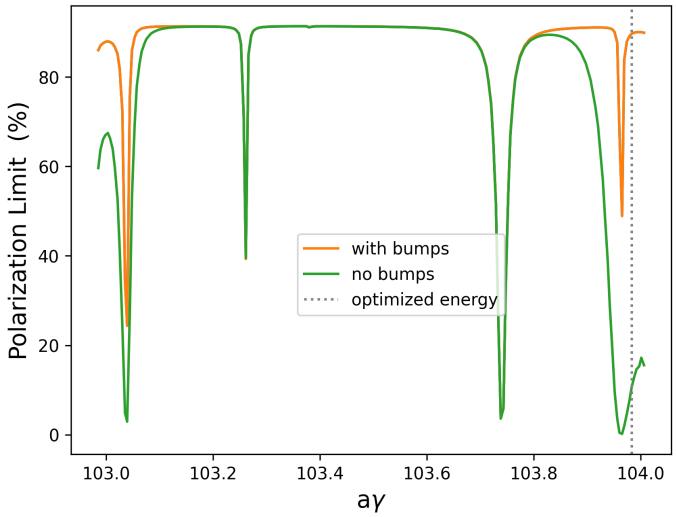

Figure 2: First order energy scan with and without harmonic bumps optimised at 45.82 GeV ($a\gamma = 103.983$) using the Rossmanith-Schmidt scheme in the V22 lattice [9].

After conventional lattice correction, one method to improve the polarisation level and alleviate the effects of misalignments is Harmonic Closed-Orbit Spin Matching (HCOSM), which uses closed vertical-orbit bumps to manipulate the stable spin direction on the closed orbit ($\hat{n}_0(s)$) and minimise the polarisation loss due to the spin diffusion. Each bump contains three individually powered vertical-orbit correctors, which are installed next to three consecutive vertically focusing arc quadrupoles. A response matrix is used to represent the linear contribution of each bump to the target harmonics. In order to correct some specific harmonics of a misaligned lattice, the bump amplitudes are predicted by calculating the inverse of the response matrix.

There are three possible HCOSM schemes that are currently under consideration: the HERA formalism [13, 14], the Rossmanith-Schmidt scheme [15, 16], and the LEP method [17]. Studies of these methods use the FCC-ee V22 lattice together with effective errors resulting in a 72 μm rms vertical closed orbit. Figure 2 [18] shows the first-order equilibrium-polarisation level at an energy near the Z-energy, before and after installing four bumps at 45.82 GeV using the Rossmanith-Schmidt scheme. We note, that at a closed orbit spin tune of 103.0 the polarisation does not vanish, which is a simulation artefact from choosing finite energy steps. Employing HCOSM, the polarisation loss near both integer resonances next to the Z-pole is significantly improved. This scheme assumes that the vertical orbit information is obtained from Beam Position Monitors (BPMs) installed at both ends of each dipole (or quadrupole), and does not consider BPM misalignments, resolution or calibration errors. Such extensive instrumentation would be costly, and is, hence, currently the main obstacle to applying HCOSM. Future investigations aim to explore possible HCOSM scheme using

fewer BPMs, and test the effectiveness of this scheme in the presence of various lattice errors, BPM misalignments, resolution and calibration errors. In addition, applying HCOSM at W energies and above will be explored with the goal of achieving a few percent polarisation at these operation points.

4.4 The question of the beam energy

In a perfectly flat circular machine with no solenoid, or synchrotron radiation, the instantaneous spin precession frequency Ω is related to the instantaneous beam energy by

$$\Omega = \Omega_0(1 + a\gamma) \tag{3}$$

where Ω_0 is the revolution frequency. However, energy sawtooth, caused dominantly by synchrotron radiation leads to a different beam energy along the synchrotron storage rings. Averaging over one revolution, the number of spin precessions along the closed orbit is determined by the average beam energy, neglecting misalignments or solenoids, namely

$$\nu_0 = \frac{\langle\Omega\rangle}{\Omega_0} - 1 = a\,\langle\gamma\rangle \tag{4}$$

where a is the gyromagnetic anomaly. In RDP measurements, the value of $a\langle\gamma\rangle$, obtained from the average beam energy of the average closed orbit deviates from ν_0 due to machine imperfections. The discrepancy between the closed-orbit spin tune, which is more readily accessible in simulations, and the value of $a\langle\gamma\rangle$ derived from the estimated average energy, is utilized to provide a preliminary assessment of the magnitude of the systematic error between measured and actual closed-orbit spin tune, and hence, the beam energy.

A method has been developed to estimate the average energy by averaging the beam energy over the bending angles. This method yielded results consistent with the closed orbit spin tune in a perfectly aligned flat machine without solenoids within below 1 keV. Figure 3 shows the rms closed-orbit spin tune shift from $a\langle\gamma\rangle$ in the presence of arc and IR misalignment up to, respectively 25 µm and 100 µm. In this range, the spin tune shift remains below 100 keV. However, the actual magnitude of the current systematic error requires further evaluation, as incorporating additional complex factors could easily push it beyond the precision target. Future studies aim at evaluating this shift considering more realistic machine errors together with dedicated tuning strategies.

5 Wigglers

The natural polarisation rise time in the FCC-ee at the Z operation mode is about 250 h, which is too long to wait at the start of physics fills before RDP measurements are performed. Therefore, the pilot bunches must either be injected in a polarised state, or the time needed for polarisation to build up in the FCC-ee must be reduced. The latter approach is the current baseline strategy, as proposed in Ref. [19]. Polarisation wigglers will be used to reduce the rise time such that sufficient transverse polarisation of about 10 % can be achieved in about 100 min. At the start of fill about 160 pilot bunches will be injected with the polarisation wigglers turned on, but no physics bunches on account of the severe synchrotron radiation

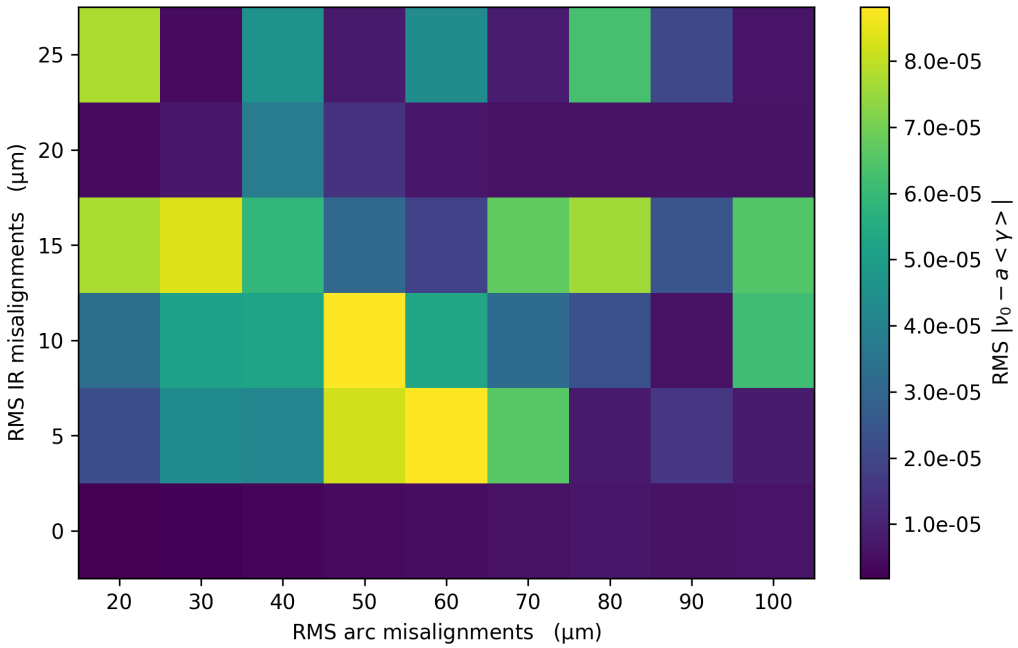

Figure 3: Colour map of the rms closed-orbit spin tune shift from $a\langle\gamma\rangle$ in the presence of varying levels of arc and IR misalignments.

during this period of operation. After sufficient polarisation is reached, currently assumed to be about 5 to 10 %, the wigglers will be ramped down, whilst keeping the polarised pilot bunches. The rest of the machine will then be filled with colliding bunches and RDP measurements will be performed on the pilot bunches at regular intervals. Assuming 160 pilot bunches and a pilot bunch life time of 20 h, this corresponds to roughly one pilot bunch being available for an RDP scan every 7.5 min. By the time the last pilot bunch has been depolarised for the first time, the pilot bunches that were depolarised first will have naturally reacquired sufficient polarisation to be measured again.

Requirements on the number and strength of the wigglers have been determined in Ref. [19], taking into account the orbit excursion and synchrotron-radiation power. While reducing the polarisation time, the energy spread is increased, which could lead to polarisation loss and an increased spin-modulation index. Developing wiggler specifications must, therefore, aim to limit the introduced energy spread. The wiggler design for FCC-ee follows the three-pole design of the LEP damping wigglers [20]. The current FCC-ee lattice design foresees the installation of the wigglers in a short straight section downstream of each IP. Wigglers will be grouped in packages of three units, and two packages will be installed in consecutive 16 m long drift-spaces. The required number of polarisation wigglers and first specifications are given in Table 1.

The alternative approach of injecting polarised beams would have the advantage of making more time available for physics operation. This option is under investigation.

Table 1: Initial specifications for the polarisation wigglers.

Parameter	Value
Number of units per beam	24
Central field B_+ [T]	0.7
Central pole length L_+ [mm]	430
Asymmetry ratio $r = \frac{B_+}{B_-} = \frac{L_-}{L_+}$	6
Critical energy E_c [keV]	968

6 Injection of polarised bunches

The current operational scenario foresees the injection of unpolarised pilot bunches, which will naturally polarise over time in the collider rings thanks to the Sokolov-Ternov effect. Even with foreseen wigglers, achieving 5 to 10 % polarisation requires roughly 90 min at the Z-pole. During that time, no physics bunches can be circulating in the machine. Since beam energy measurements are foreseen to take place in parallel to physics experiments, this waiting time is required after every beam dump.

Availability studies [21] including failures of systems such as e.g. RF-systems or power converters suggest a great improvement of total integrated luminosity if pre-polarised bunches could be injected into the collider rings. Although no complete study has been performed so far, first thoughts and preliminary results are described here.

6.1 Generation of polarised bunches

Whereas polarised electrons could, in principle, be generated by a polarised source, this is not possible for positrons. Thus, a ring is needed to generate polarised bunches at low energy. Such a polarisation and Damping Ring (PDR) would have some similarities with the damping ring. An important difference is that, in order to achieve significant polarisation levels, the wigglers have to be asymmetric with higher fields over shorter distance deflection in one direction (typically inwards) and lower fields over longer regions deflecting in the opposite direction.

The polarisation build-up time constants are in the order of minutes for an optimised low energy ring and, thus, significantly shorter than the baseline scheme polarisation build-up in the collider prior to filling with physics bunches. As the polarisation build-up at low energy is long compared to synchrotron radiation damping times in the damping ring, the latter cannot be used and a dedicated ring is needed. The proposed low energy polarisation ring could be used for the generation of both polarised positron and electron bunches.

6.2 Transmission to end of the LINAC

The polarised bunches with a vertical equilibrium polarisation are extracted from the PDR and injected into the linac with their vertical polarisation. The vertical polarisation is maintained throughout the linac.

6.3 Transfer line and booster injection

To date, no complete optics is available for the Transfer Line (TL) from the end of the linac to the injection point of the booster. The TL lattice has only been matched for the main segments, matching between the segments has not been completed. The TL geometry with all the dipoles that are relevant for spin transport in the absence of imperfections is however available. This information was used for first estimates of the transmission of vertical polarisation to the booster injection.

The TL geometry for electrons and position is presented in Fig 4. Electrons and positrons share most of the line, only the last sections differ since the two species are injected in opposite directions into the booster.

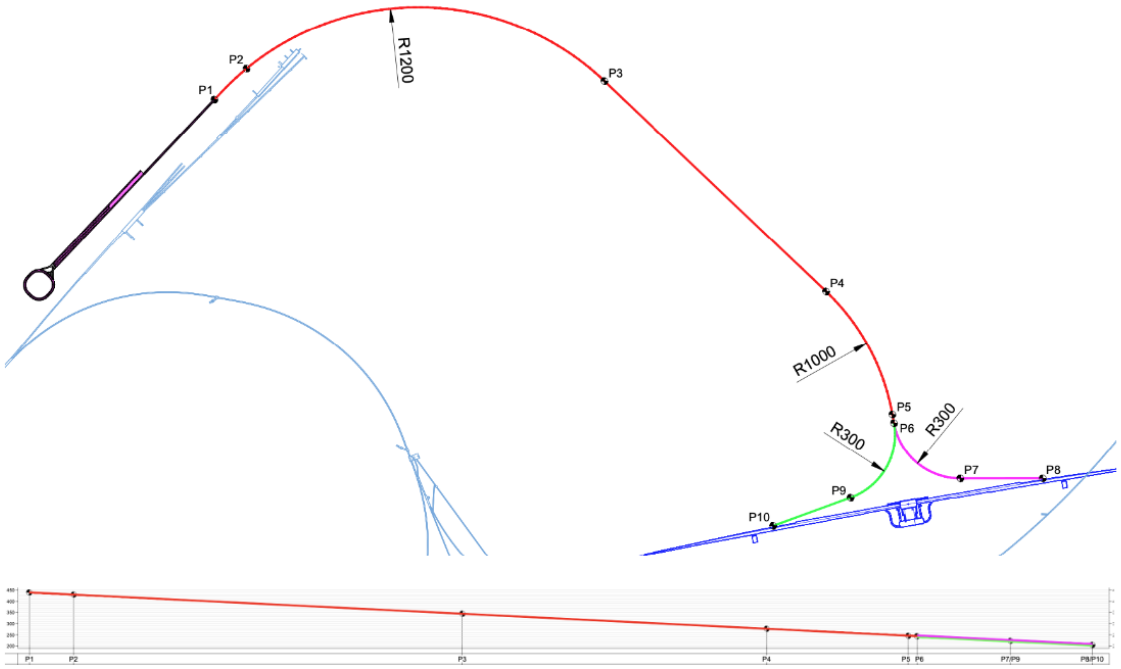

Figure 4: Geometry of the roughly 5.5 km long transfer line from linac to booster. Bottom: vertical cut with a height difference of 230 m between linac and booster.

The transport of polarisation through the TL was investigated assuming an initial vertical polarisation of the beam [22]. The vertical bends at the beginning of the TLs rotate the polarisation away from the vertical direction. Along most of the TL length, the polarisation (spin) vector precesses around the vertical axis before the last bends rotate it back the vertical. Due to the spin phase advance between the vertical bends at start and end of the TL, the polarisation may not be restored.

At the nominal momentum of 20 GeV, $a\gamma = 45.388$. The total spin phase advance in the horizontal (bending) plane of the TL is 25.2 $[2\pi]$ for the part leading to the green branch and 5.0 $[2\pi]$ for the magenta branch of the TL (see Fig. 4). The large difference is due to the fact that in the magenta branch, the bending changes sign in the last section and the spin precesses "back". This difference is also reflected in the fact that the total bending in the green branch is larger that 180° while it is around 45° for the magenta branch (with respect

to the direction at the exit of the linac).

By adjusting slightly the energy at the end of the linac (and of course at booster injection) to 19.873 GeV, $a\gamma = 45.099$, the total spin phase advance of both TL segments can be brought close to an integer: 25.04 $[2\pi]$ for the green branch and 4.97 $[2\pi]$ for the magenta branch. Under such conditions the vertical bends at the end of the TL can effectively restore the initial polarisation direction. The results of polarisation tracking though the two branches of the TL are presented in Figures 5 and 6: the polarisation is very well preserved, with only a loss of a few %. The only side effect of this energy adjustment is a spin tune at injection into the booster that is close to the integer, i.e. $a\gamma = 45.099$.

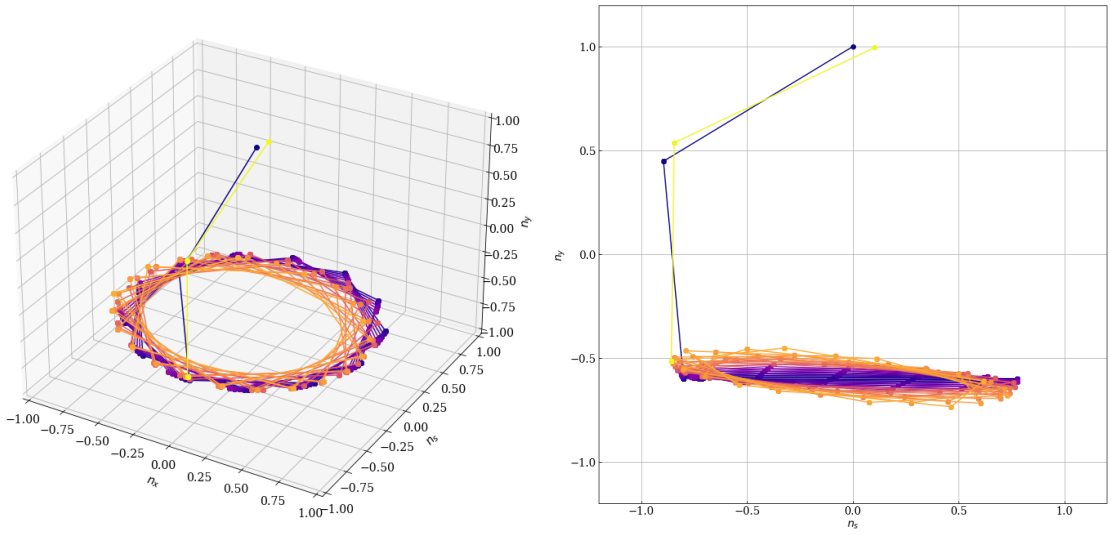

Figure 5: Polarisation transport through the green branch of the TL. The polarisation is initially vertical (dark blue point). Each point represents the polarisation direction in one elements of the line, color-coded from dark blue to yellow. The final orientation of the polarisation is given by the yellow point. Left: three dimensional representation (x,s,y). Right: projection in the s-y plane.

The estimated bunch energy spread at the exit of the linac is 0.01%, while the shot-to-shot energy jitter is estimated to 0.03%. Assuming that the later corresponds to two standard deviations, the convoluted rms spin tune spread at the entrance of the TL is estimated to be $\sigma_{a\gamma} = 0.083$. A convolution of the spin tune spread with the polarisation transport efficiency as a function of the spin tune results in a $\approx 97\%$ transmission of the polarisation.

The combination of horizontal bending on a transfer line with a slope leads to a rotation of the coordinate system. While this effect is usually very small for short lines, it cannot be ignored for transfer lines of many kilometres. This coordination system rotation affects for example the transfer lines from the SPS to the LHC ([23]). For the FCC-ee TL the effect is small for the magenta branch (due to the reversed bending in the last segment), but it is important for the green branch, with a tilt of the coordinate system of almost 10° degrees. The effect must be properly analysed in future simulations, but the potential impact on the vertical polarisation will not exceed a few percent.

Those results will have to be refined once a complete optics becomes available.

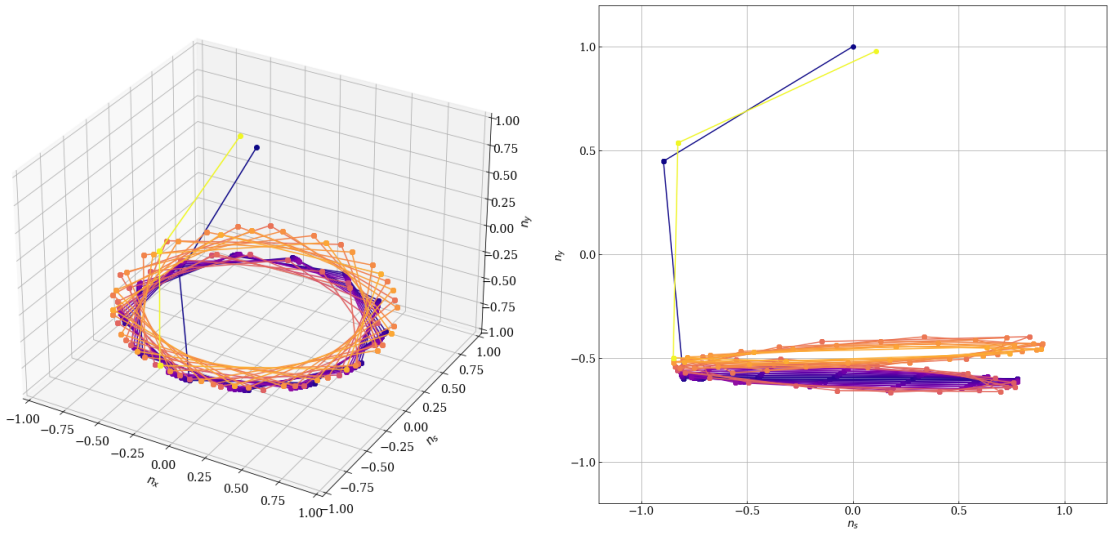

Figure 6: Polarisation transport through the magenta branch of the TL. The polarisation is initially vertical (dark blue point). Each points represents the polarisation direction in one elements of the line, color-coded from dark blue to yellow. The final orientation of the polarisation is given by the yellow point. Left: three dimensional representation (x,s,y). Right: projection in the s-y plane.

The booster injection will have little impact on the vertical polarisation: the septa bend horizontally, and the vertical deflection of the injection kicker is very small, with negligible impact on the vertical polarisation.

6.4 Booster energy ramp

As the beam energy ramps in an electron (positron) booster ring, so is the closed orbit spin tune ν_0 and the amplitude-dependent spin tune ν_s among beam particles since $\nu_s \approx \nu_0 \approx a\gamma$. The crossing of the underlying spin resonances could lead to beam depolarisation. The polarisation loss during crossing of a single, isolated spin resonance $\nu_0 = K$ can be estimated with the Froissart-Stora formula [24]

$$P_f/P_i = 2e^{-\frac{\pi|\tilde{\omega}_K|^2}{2\alpha}} - 1 \ , \tag{5}$$

P_i and P_f are the beam vertical polarisation before and after crossing the resonance, $\tilde{\omega}_K$ is the spin resonance strength, $\alpha = \frac{da\gamma}{d\theta}$ is related to the energy ramping rate. There are two families of important spin resonances in this context: the imperfect resonances $\nu_0 = k, k \in \mathbb{Z}$, mainly driven by horizontal magnetic fields due to vertical orbit offsets in quadrupoles and dipole roll errors, and the intrinsic resonances $\nu_0 = k \pm Q_y, k \in \mathbb{Z}$ with Q_y the vertical betatron tune, driven by the horizontal magnetic field due to vertical betatron oscillations in quadrupoles. Adjacent imperfection resonances are spaced by 440 MeV, hundreds of spin resonances of these two families will be crossed in the acceleration of FCC-ee high energy booster (HEB) from injection energy at 20 GeV to extraction energies of 45.6 GeV, 80 GeV, 120 GeV and 182.5 GeV. Since the HEB operates in a fast ramping manner, α is on the

order of 0.01, only if the spin resonances are so weak that $|\epsilon| \ll 0.005$ then the depolarisation when crossing each resonance is much less than 1%, the beam polarisation could be mostly preserved. It is therefore essential to evaluate the spectrum of spin resonances of the HEB lattices.

The spin resonance spectra of two different HEB lattices, i.e., the FODO 90 lattice and the HFD lattice were evaluated [25]. Both feature a super-periodicity of $P = 8$ with interleaved arc and straight sections. Each arc section contains $M = 175$ standard cells, the vertical betatron tunes are $Q_y = 416.29$ and $Q_y = 382.29$ respectively, and the total contribution from these arc sections to the vertical betatron tune is 350 and 320 respectively. These lattices have effectively a very large super-periodicity of $PM = 1400$. Following previous studies for the CEPC booster [26], the super strong intrinsic and imperfection resonances are located near $(kPM \pm \nu_B)/\eta, k \in Z$, η is the fraction of the total bending angle of all standard arc cells in 2π, which equals to 0.9486 for both lattices. Therefore, the first super strong resonances are located near $\nu_0 = 369$ and $\nu_0 = 337$ for these two lattices, corresponding to a beam energy of 162.6 GeV and 148.8 GeV respectively. This suggests strong depolarisation in the acceleration to the ttbar energy, while the spin resonances can be relatively weak in the acceleration up to the HZ energy [25].

To evaluate the transmission of beam polarisation during the acceleration process, a cosine shape energy ramping curve was assumed, following

$$E(t) = E_{\text{inj}} + \frac{(E_{\text{ext}} - E_{\text{inj}})}{2}\left(1 - \cos\left(\frac{\pi t}{t_{\text{ramp}}}\right)\right) \ . \tag{6}$$

It should be noted that this is an inefficient ramp compared to a standard Parabolic-Linear-Parabolic (PLP) ramp shape. A PLP is efficient because the ramp is mostly linear and matched to the ratings of the large power converters (ramp and acceleration rates). A cosinus shaped ramp does not make good use of the ramp rate performance, respectively requires much more performant power converters with a significant impact on cost. Since the depolarisation mostly occur near the higher energy end with generally stronger spin resonance strengths and a slower energy ramping rate which inevitably decreases to zero, assuming cosine shape ramp shape could provide a reasonable estimates of the polarisation transmission, before more detailed energy ramp design is available taking into account various engineering complexities.

The booster parameters are taken from the mid-term report of the FCC Feasibility Study. Imperfect lattices were generated and closed orbit corrections were conducted, for the evaluation of strengths of imperfection resonances. The intrinsic and imperfection spin resonance strengths were evaluated using the DEPOL code [28] for both lattices, as shown in Fig.7.

The coloured curves show the spin resonance strength with 99% polarisation transmission. Those spin resonances above these curves lead to more substantial depolarisation. Assume there is no correlation between the crossings of multipole spin resonances, the Froissart-Stora formula are repetitively used to estimate the cumulative effects of the depolarisation due to the crossing of each intrinsic and imperfection resonances. Up to 120 GeV, intrinsic resonances cause negligible depolarisation, and some stronger imperfection resonances together with the slower ramping speed at the higher energies would lead to some depolarisation. In the acceleration to 182.5 GeV, more severe depolarisation is expected mainly due to the large number of stronger imperfection resonances.

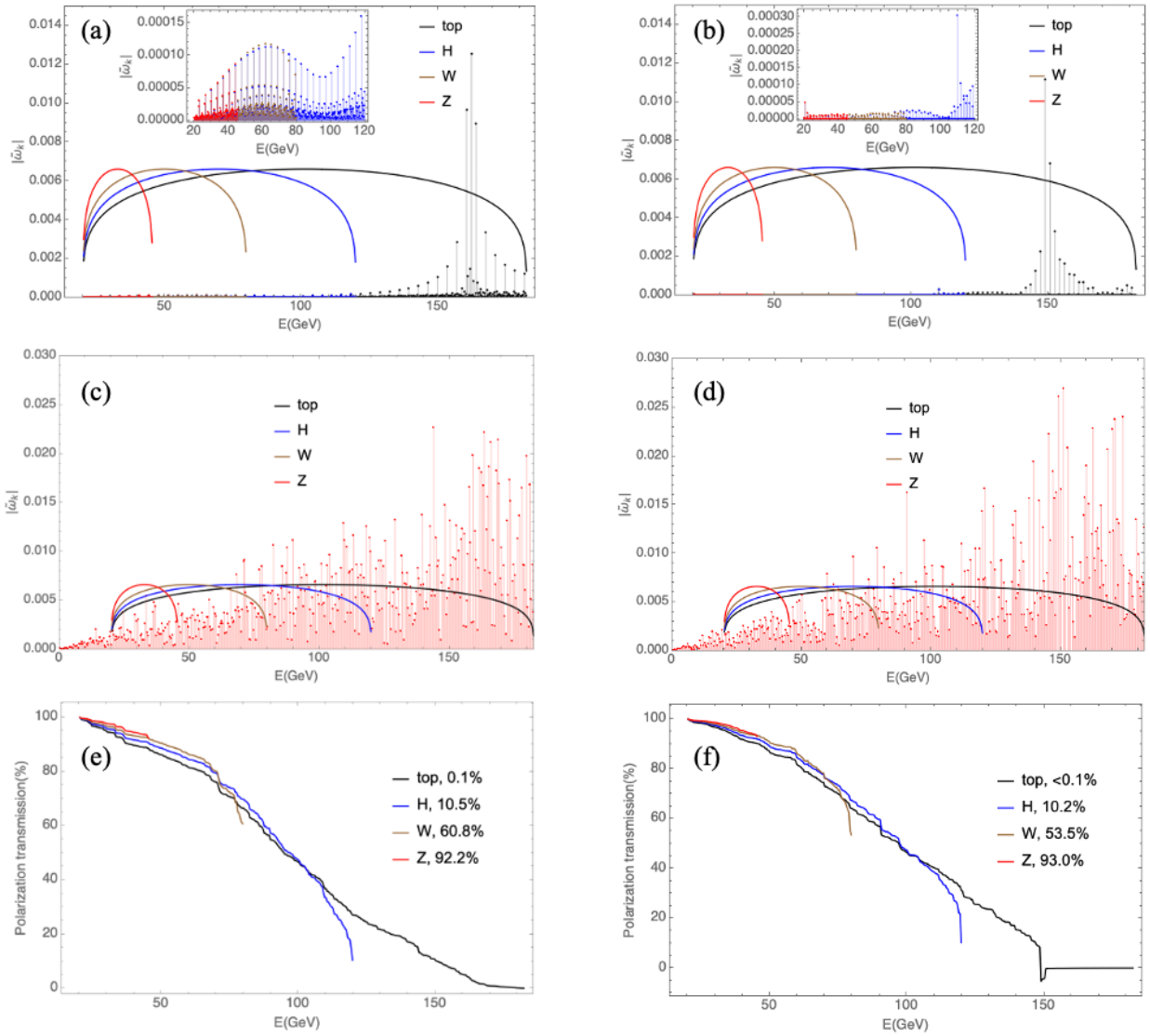

Figure 7: Spin resonance spectra for the two HEB lattices [25, 27]. For the FODO 90 lattice, (a), (c) and (e) are the spectra of intrinsic resonances of the bare lattice, the spectra of the imperfection resonances of an imperfect lattice seed, and the polarisation transmission as estimated by repetitive usage of the Froissart-Stora formula. (b), (d) and (f) are the corresponding results for the HFD lattice.

More random imperfect lattice seeds were generated for both lattices for the evaluation of the polarisation transmission, as shown in Fig. 8. Assuming 100% polarisation at the injection energy, the extracted beam polarisation is typically about 90% at 45.6 GeV, about 60% at 80 GeV, about 15% at 120 GeV and zero at 182.5 GeV, no major difference between the two HEB lattice is seen.

These studies were based on the error settings and correction schemes still under development, and more comprehensive error sources and more sophisticated error correction schemes are yet to be included. The ramping curve can be in principle optimized to partially reduce the depolarisation, but the more realistic PLP ramp yields a bit worse polarisation trans-

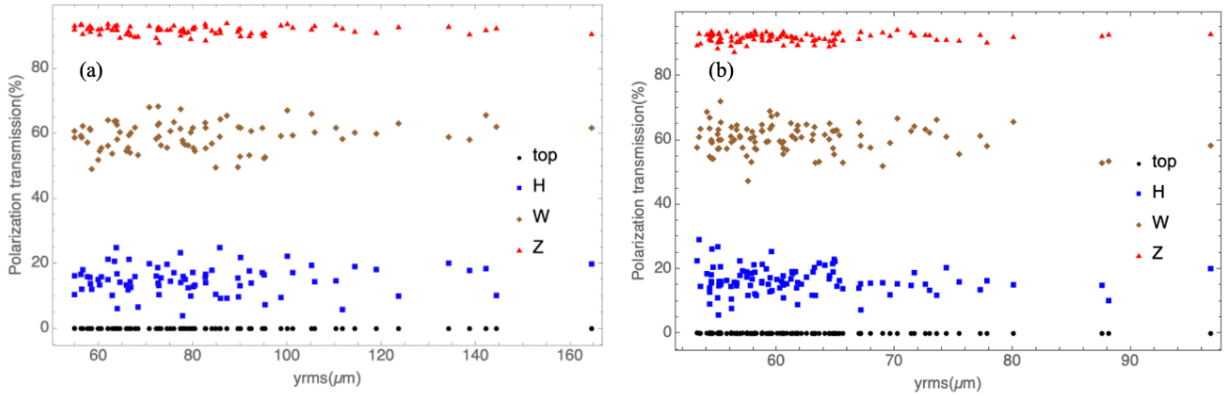

Figure 8: Estimated polarisation transmission to different extraction energies [27]. (a) shows the polarisation transmission as a function of the vertical rms closed orbit distortion for 79 random seeds of the FODO 90 lattice; (b) shows the corresponding result for 100 random seeds of the HFD lattice.

mission for the Z-mode, compared to the result obtained by assuming the cosine ramp. The polarisation transmission was estimated by repetitive usage of the Froissart-Stora formula, and previous comparison between estimates and tracking simulations showed good agreement in the polarisation transmission if the depolarisation is small, while tracking simulations are necessary to quantitatively evaluate the preserved polarisation level after acceleration to higher energies like HZ. In summary, this preliminary study suggests the polarisation can be well preserved in the booster acceleration to Z and W energies, if highly polarised beams are prepared from the source and injected into the booster with the proper vertical polarisation direction.

6.5 Collider injection

No details are available for the geometry of the transfer between booster and collider rings. It has however been agreed that vertical and horizontal bending will not be interleaved, thus no issues are expected at this stage of the study.

7 FCC powering

The main dipole magnets define the beam energy on the central orbit (*i.e.* which is centred on average in all quadrupoles). The stability of the magnetic field must match the desired accuracy of a single energy measurement, at least on the time scale of a single RDP measurement, else the depolarising resonance width will be enlarged by the magnetic field ripple.

For a target accuracy of 10 keV for example, the intrinsic magnetic field stability at 45 GeV should be at the level of 0.2 ppm (excluding uncontrolled external perturbations). This translates into the same stability of the power converters feeding the main dipoles magnets. This stability requirement applies for a time scale of one hour which should be sufficient even for slow RDP scan (see below).

8 Depolarisers System

It is foreseen that the depolariser systems will be used for all bunches. On the one hand polarised pilot bunches are depolarised regularly to determine the beam energy. On the other hand, colliding bunches build up polarisation over time, which has the potential to bias measurements of electroweak observables, and therefore these bunches must be depolarised too. Considerations presented here on the depolariser focus on requirements for RDP scans.

8.1 Placement considerations

In the FCC-ee without a solenoid or misalignments, the polarisation vector is oriented fully vertically. RDP aims to destroy this polarisation by rotating the spin away from the vertical axis which requires excitation of the vertical orbit. To avoid a propagating vertical orbit and forced vertical betatron oscillation through the machine, even for the pilot bunches, these orbit bumps must be closed, realised by either two kickers with $n \times \pi, n \in \mathbb{N}$ phase advance between them, or three kickers with less stringent phase-advance constraints. Furthermore, a closed orbit bump without any dipole magnets in-between resembles a closed spin-orbit bump without any net rotation. The depolarisers must, therefore, be integrated in the arc structure. In Ref. [29] a 2π-bump solution is proposed, namely applying a vertical kick of 10 µrad, which is closed over four FODO cells, as shown in Fig. 9.

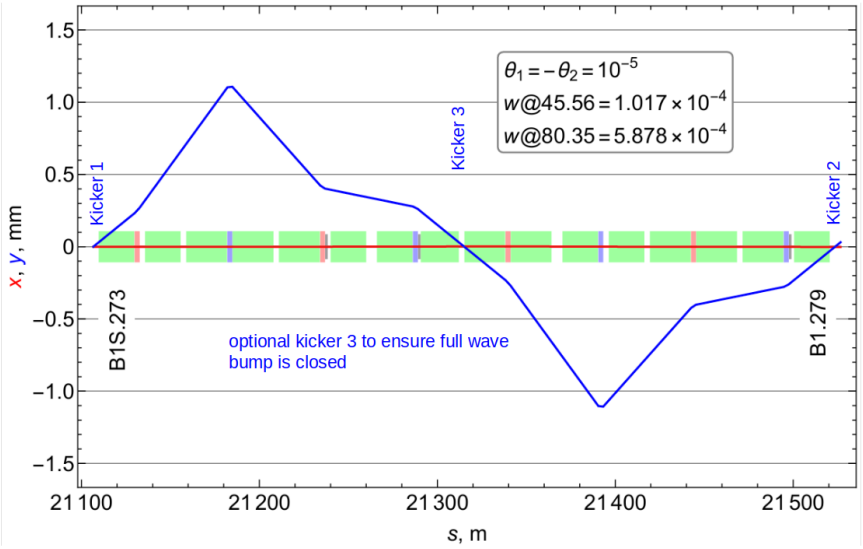

Figure 9: Proposed vertical closed-orbit kick in the arcs.

Efforts have started to implement spin dynamics in Xsuite [30]. One particle with an initially vertically aligned spin is tracked through the proposed 2π-bump. When propagating through the lattice the spin is rotated out of the vertical axis, into horizontal and longitudinal directions. The spin projection over this region is shown in Fig. 10 with the starting point marked as blue and the end as yellow. Preliminary results find that the deviation from the vertical axis is only approximately 1.4 times larger, compared to a single kick deflection,

stemming from a very small dipole bending angle over this region resulting in a rather low spin precession.

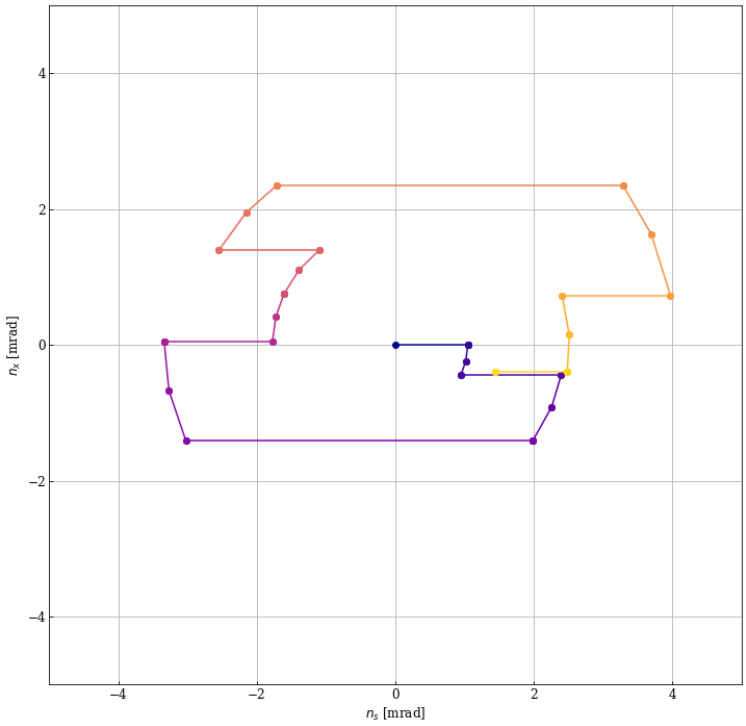

Figure 10: Horizontal and longitudinal components of the spin vector over the 2π bump.

The same bump is applied at higher beam energies, which feature a larger spin tune. It is shown in Fig. 11 that the effective spin rotation over this bump increases with increasing spin tune. This is expressed as the amplification factor, which gives the enhancement of spin rotation with respect to applying a single kick.

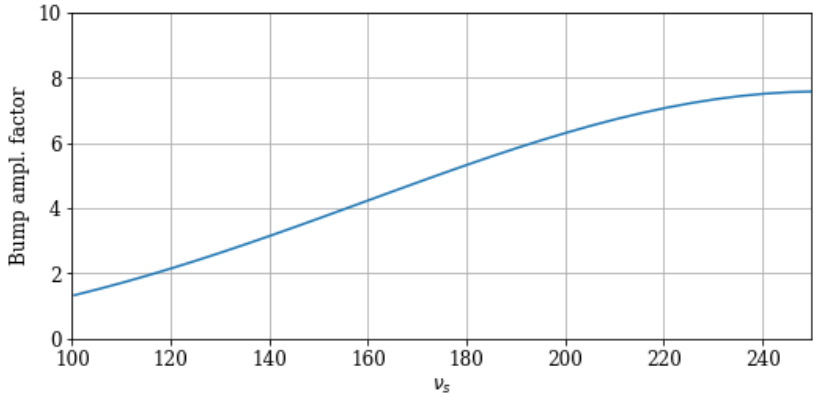

Figure 11: Amplification factor from 2π-bump over various spin tune ν_s.

If one does not impose a kicker system in the form of at least one closed bump, but rather relies on a single kicker, and, therefore, a propagating orbit through the machine, the

performance of the depolariser could be reinforced significantly by the full FCC-ee lattice. It should however be pointed out that this option is not recommended due to the large betatron oscillation of the kicked bunches. The gain from the optical structure itself, calculated here using the ASPIRRIN program [31] as a modulus of the spin-orbit response function $|F_3|$, can be many thousands and even tens of thousands units as seen in Fig. 12 for the Z-lattice at 45.1358 GeV, corresponding to ν_0 of 102.45.

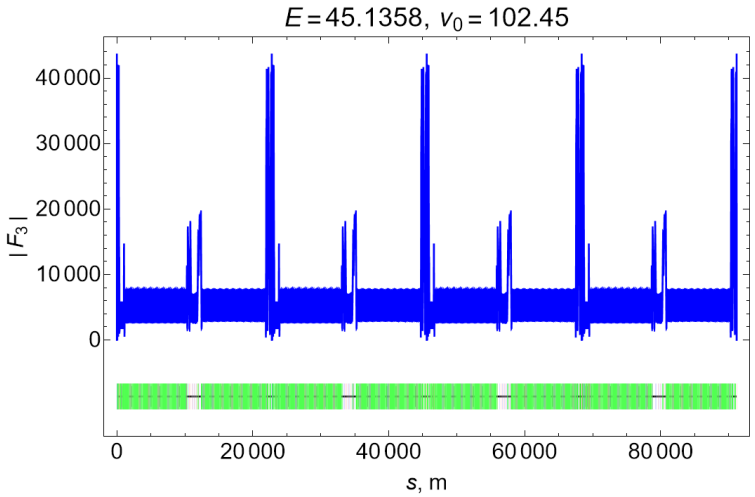

Figure 12: Spin-orbit response function $|F_3|$ for the closed-orbit spin tune 102.45 of the machine circumference.

8.2 Simplified model

A simplified simulations framework is generated to study the RDP process, based on one-turn matrices. A more detailed description is given in [32]. The precession of particle spin is governed by the Thomas-BMT equation

$$\frac{d\vec{S}}{ds} = \vec{\Omega} \times \vec{S}\,, \tag{7}$$

where the spin rotation frequency in units of inverse metre is related to the electromagnetic fields as [33, 34]

$$\vec{\Omega} = -\frac{1}{(B\rho)_0}\left((Q+1-\delta)\left(\vec{B} - \hat{\vec{v}} \times \frac{\vec{E}}{c}\right) - Q\hat{\vec{v}}(\hat{\vec{v}} \cdot \vec{B})\right)\,. \tag{8}$$

Assuming only a vertical magnetic field, $\vec{\Omega}$ has solely a vertical non-zero component. Further, in the absence of transverse particle motion, the spin motion is simply a precession around the vertical axis with a closed-orbit spin tune ν_0 [35]. The one-turn spin matrix, therefore, becomes

$$\begin{pmatrix} S_x \\ S_y \\ S_z \end{pmatrix}_{n+1} = \begin{pmatrix} \cos 2\pi\nu_0 & 0 & -\sin 2\pi\nu_0 \\ 0 & 1 & 0 \\ \sin 2\pi\nu_0 & 0 & \cos 2\pi\nu_0 \end{pmatrix} \begin{pmatrix} S_x \\ S_y \\ S_z \end{pmatrix}_n\,. \tag{9}$$

The excitation through the depolariser, before or after every turn, is described by

$$\Delta\vec{S}(n) = \begin{pmatrix} \theta_x(n) \\ 0 \\ 0 \end{pmatrix} \times \begin{pmatrix} S_x \\ S_y \\ S_z \end{pmatrix}_n , \tag{10}$$

where

$$\theta_x(n) = \theta_s \sin(Q_{\mathrm{dep},0} 2\pi n + \tilde{q}_{\mathrm{dep}} \pi n^2) , \tag{11}$$

with instantaneous depolariser tune

$$Q_{\mathrm{dep}}(n) = Q_{\mathrm{dep},0} + \tilde{q}_{\mathrm{dep}} n . \tag{12}$$

We note that ν_0 and θ_s depend on a particle's relative energy deviation $\delta \equiv \Delta E/E$ as $Q_0 \to \nu_0(1+\delta)$. At 45.6 GeV beam energy, a single depolariser deflects the particle bunch by about 10 μrad, and rotates the spin by about $a_e\gamma$ this amount, that is by about 10^{-3} rad in a single passage. Furthermore, the kicks of the depolarizers are summarized here in one effective kick.

Simulations without synchrotron oscillation, for a single on-energy particle, with initial spin oriented towards the positive vertical direction ($S_{y_{\mathrm{initial}}} = 1$) are performed, assuming a tune sweep velocity, $\tilde{q}_{\mathrm{dep}}$ and kick strength θ_s. The scan is performed in both directions. It can be seen in Fig. 13 that the spin is fully flipped at $Q_{\mathrm{dep}} = \nu_0$.

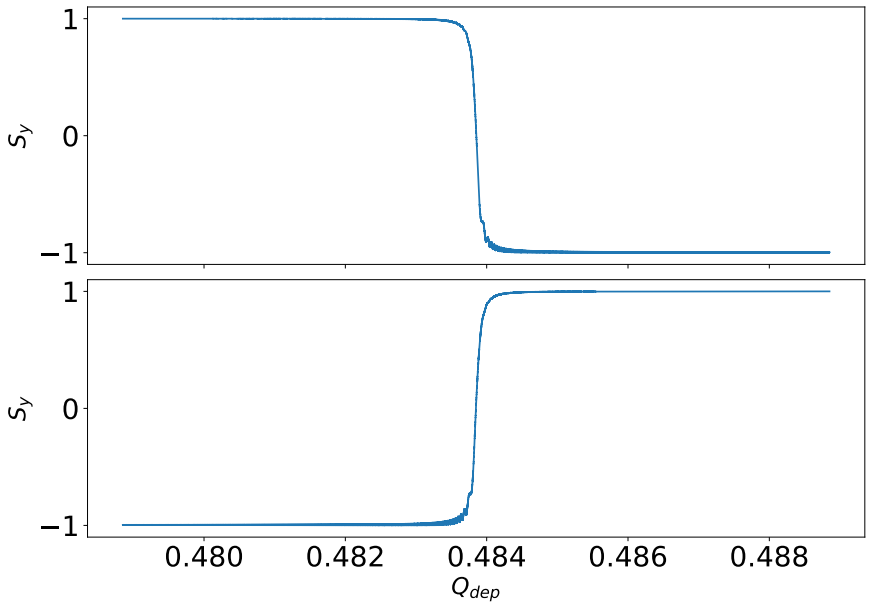

Figure 13: RDP scan for a single on-energy particle with $\tilde{q}_{\mathrm{dep}} = 10^{-8}$ and $\theta_s = 10^{-3}$. The scan is performed from lower to higher depolarising frequencies (top) or in the opposite direction (bottom).

Next we consider particles with an initial relative energy offset of a few times 10^{-4}, while executing synchrotron oscillations. In this scenario synchrotron sideband resonances appear around the spin tune ν_0 at locations $Q_{\mathrm{dep}} = \nu_0 \pm mQ_s$ and $Q_{\mathrm{dep}} = 1 - \nu_0 \pm mQ_s$, where Q_s denotes the synchrotron tune and m is an integer, as is illustrated in Fig. 14.

In this figure, the first resonance on the left corresponds to the sideband $Q_{\mathrm{dep}} = \nu_0 - Q_s$, followed by $Q_{\mathrm{dep}} = 1 - \nu_0 - 2Q_s$. The main resonance is then crossed at 0.484, followed by the sideband at $Q_{\mathrm{dep}} = 1 - \nu_0 - Q_s$. Each time a resonance is crossed the spin is rotated in or out of the vertical plane to a greater or lesser degree.

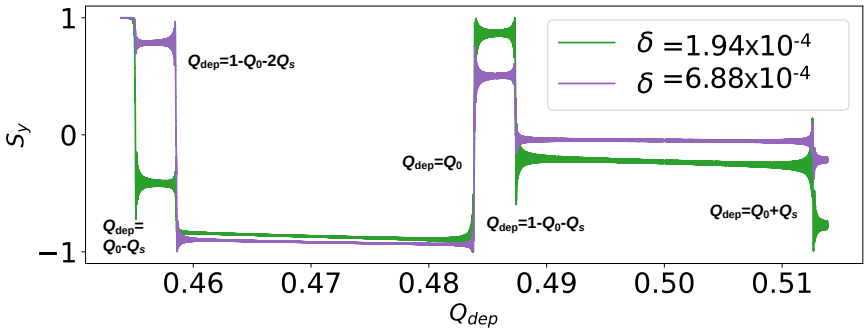

Figure 14: RDP scans for single particles undergoing synchrotron oscillations with $\tilde{q}_{\mathrm{dep}} = 10^{-8}$, $\theta_s = 10^{-3}$, and two different initial energy offsets. We note that in this plot Q_0 denoted ν_0.

We note that this simulation framework represents an idealistic, simplified description of the RDP process, neglecting betatron oscillations, detailed machine description, synchrotron radiation, energy drifts, etc. Nevertheless, it can be seen as a starting point to fully understand the RDP process and could be extended in future studies. Results assuming one Gaussian bunch with synchrotron oscillations are given in [32].

8.3 Considerations for RDP scans

We assume that the main mode of the RDP procedure should be a continuous monotonic scanning of the kicker frequency with the following considerations.

- The natural width of the spin line, caused by the energy spread of the beam, is about 200 keV at 45 GeV and 1.4 MeV at 80 GeV due to the radiative diffusion of the spin precession and influence of a quadratic non-linearity of the guide field at FCC-ee.
- To determine the spin resonance with an uncertainty much smaller than the width of the spin line, it is proposed to perform RDP scans in both frequency directions.
- In general, the main spin resonance may drift in time. As shown by preliminary Monte-Carlo simulation, scanning two bunches in opposite directions at the same time, allows determining the beam energy with an accuracy better than 10 keV, relative to a certain point in time together with the speed and direction of the collider energy drift.
- Given the accuracy requirements, the relevant scan rate should be in the order of 1 keV/s in energy units, or 0.007 Hz/s in the frequency scale. The corresponding resolution of the kicker-synthesizer in terms of the frequency tuning step should be no worse than 10^{-4} Hz, if taken with a margin.

- The depolariser is assumed to be implemented as a stripline that creates a TEM wave propagating towards the beam, as shown in Fig. 15. In this case, the depolarising effect is exerted by the horizontal magnetic and vertical electric fields of the wave together.

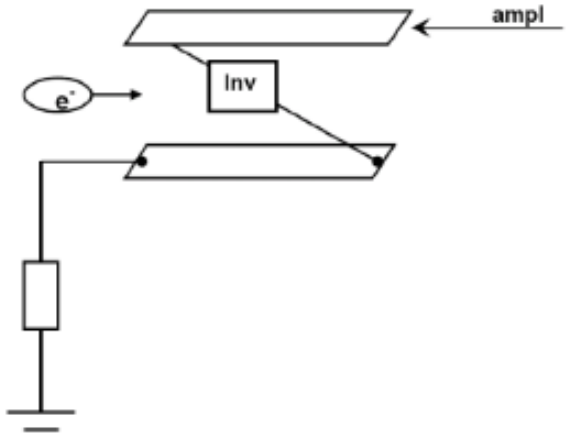

Figure 15: TEM wave-based depolariser conceptual design: "ampl" is an amplifier of signal from the synthesizer; "inv" is the signal inverter.

8.4 Depolariser design

A depolariser kickers stripline design supplied by RF power, counter propagating the beam offers both the required bandwidth for bunch selective RDP scans and the possibility to inject a signal to prevent polarisation build up on the physics bunches as needed. Integrating the system together with the kickers needed for the transverse feedback remains to be studied in detail, including machine protection considerations. While increasing the length of a stripline kicker increases the power efficiency, the maximum length permitted for a kicker will be defined by space considerations and the required bandwidth for bunch selective kicking of the pilot bunches spaced by 100 ns in the gaps of the beam. It is therefore suggested that the basic building block for the kickers has an active length of 1 m.

Since one closed orbit bump of 10 µrad would lead to a vertical peak orbit above 1 mm, it is proposed to distribute it over four closed-orbit bumps per beam, each providing 2.5 µrad. At least two kickers per orbit bump are required, constraining the phase advance to 180°. A weaker third kicker would ease this constraint. Hence, a total of 16 to 24 kickers are required. The third correction kicker could be designed as a slightly shorter strip-line with less RF power installed, as it only has to provide corrections to the bump.

Each kicker providing 2.5 µrad features a strip-line design of 1 m length with four electrodes, operating around 40 MHz. Keeping the nominal vacuum chamber diameter of 70 mm requires an RF power per kicker port (electrode) of 35 kW, and it is therefore suggested to reduce the vacuum chamber at the kicker to 26 mm with electrodes at a distance of 9 mm from the beam. This reduces the RF power per kicker port to 2.26 kW (9.04 kW per kicker).

Studies are underway to ensure that the overall impedance remains at an acceptable level. Table 2 shows the configuration in point PA, where one-quarter of the necessary depolariser kickers are proposed to be installed. Similar configurations are proposed in the other three experiment points. All or part of the depolariser kickers can also be used as kickers for transverse feedback systems for instability mitigation.

Table 2: Possible configuration of depolariser kickers in point PA generating a local 2.5 μrad bump, assuming that the depolariser kicker system will be distributed over all four experiment points in a similar way to provide the total effect required for RDP. A shorter kicker is used for bump correction between the two main depolariser kickers.

Location	Beam	Function	Kicker length	Power per kicker
Point PA left	electron	open bump	1.0 m	9.04 kW
Point PA left	electron	correction	0.75 m	4.5 kW
Point PA left	electron	close bump	1.0 m	9.04 kW
Point PA right	positron	open bump	1.0 m	9.04 kW
Point PA right	positron	correction	0.75 m	4.5 kW
Point PA right	positron	close bump	1.0 m	9.04 kW

As a complementary technique FSP is being investigated, where the spin is flipped into the horizontal plane, and the coherent (free-spin) precession is then observed, ideally turn-by-turn. The spin tune is then retrieved by a Fourier transform, which also yields the full spin spectrum of the spin motion. This technique would require a kicker pulse about ten times stronger than that planned for the RDP measurement. Achieving this requires an by about a factor 10 larger value for the kicker and remains to be studied in detail.

9 Polarimeter

9.1 Physics requirements and measurement techniques

The stringent demands of the beam-energy measurement at FCC-ee imposes several requirements on the polarimeter system. Most of these requirements are driven by Z-pole operation. The needs for such precision beam-energy information at the W^+W^- and ZH modes need further consideration. At $t\bar{t}$ the polarisation of the pilot bunch cannot be maintained since the beam energy spread is overlapping with depolarisation resonances, nevertheless Z calibration runs are still foreseen to be performed occasionally.

- It will be necessary to perform measurements of equal precision and frequency on both the electron and positron beams. This requires a separate polarimeter for each beam. Considerations of systematic robustness and system availability may motivate installing more than a single pair of polarimeters, perhaps with differing attributes, but this is not yet considered to be part of the baseline plan.

- The polarimeters will be mainly used for resonant depolarisation beam-energy calibration (RDP hereafter) applied to the pilot bunches, providing a precise measurement

of the average spin tune of both lepton beams. Given the relation between the average spin tune and the average beam energy, this information will be combined with the boosts measured at each experimental IP by the physics detectors to infer a precise knowledge of the collision energy conditions in each experiment.

- A second task for the polarimeter instruments will be to provide a precise knowledge of the polarisation state of the colliding bunches. Both transverse and longitudinal polarisation levels need to be measured with high precision, this is to insure absence of bias in the expected physics cross-sections at the experiments level.

- The bunch polarisation will be measured through the experimental process of inverse Compton scattering. This type of event will be produced by colliding rather dense laser pulses onto selected lepton bunches of the train. Measurements of the full polarisation vector are required, rather than only the transverse component, as was monitored at LEP. This requirement is motivated by FSP measurements, which are best performed having rotated the polarisation vector to the horizontal plane, and for placing limits on the size of any longitudinal polarisation that may exist in the colliding physics bunches. Measuring the full polarisation vector necessitates detecting both the scattered electron [1], and the back-scattered photon. On each bunch crossing we expect about 1000 Compton collision to happen. The Compton pattern obtained with 10 million events (about 3 seconds of data acquisition) is presented in Figs. 16. These patterns are finally fit with a convolution of the Born Compton cross-section with a two dimensional resolution function to extract the polarisation levels [36]. Systematic uncertainties arising from radiative corrections are expected to be of few per-mille at most at 45 GeV [37]. Toy Monte-Carlo studies have been performed at high statistics (100 million scatters) so far to investigate possible fit biases. Results are shown for the most important observables in Fig. 17.

- It is also possible to build left-right asymmetries by flipping the helicity of photons in the initial state. This technique is more robust against QED radiative corrections [37] but assumes excellent stability of all experimental parameters. This technique is still under conceptual study. Only preliminary work has been recently done.

- RDP energy calibration measurements would be performed every 10-15 minutes selecting one bunch of the pilots train. These frequent RDP measurements are essential to guard against any residual energy drifts from uncorrected tide effects or other mechanisms of energy change in the machine [38]. The baseline RDP method of operation would be to change an electromagnetic depolarising signal applied to the selected bunch by the kickers. The sweep excitation of the bunch would happen in steps over several machine turns. Each step will be followed by shining the laser on the selected bunch, for a few seconds of Compton scattering to happen providing the current polarisation level. When the depolarisation occurs, the frequency of the excitation signal at that step of the sweep is then used to provide the beam-energy calibration. A baseline goal

[1] For convenience, only the electron polarimeter will be described, with the assumption that the positron polarimeter will have identical attributes.

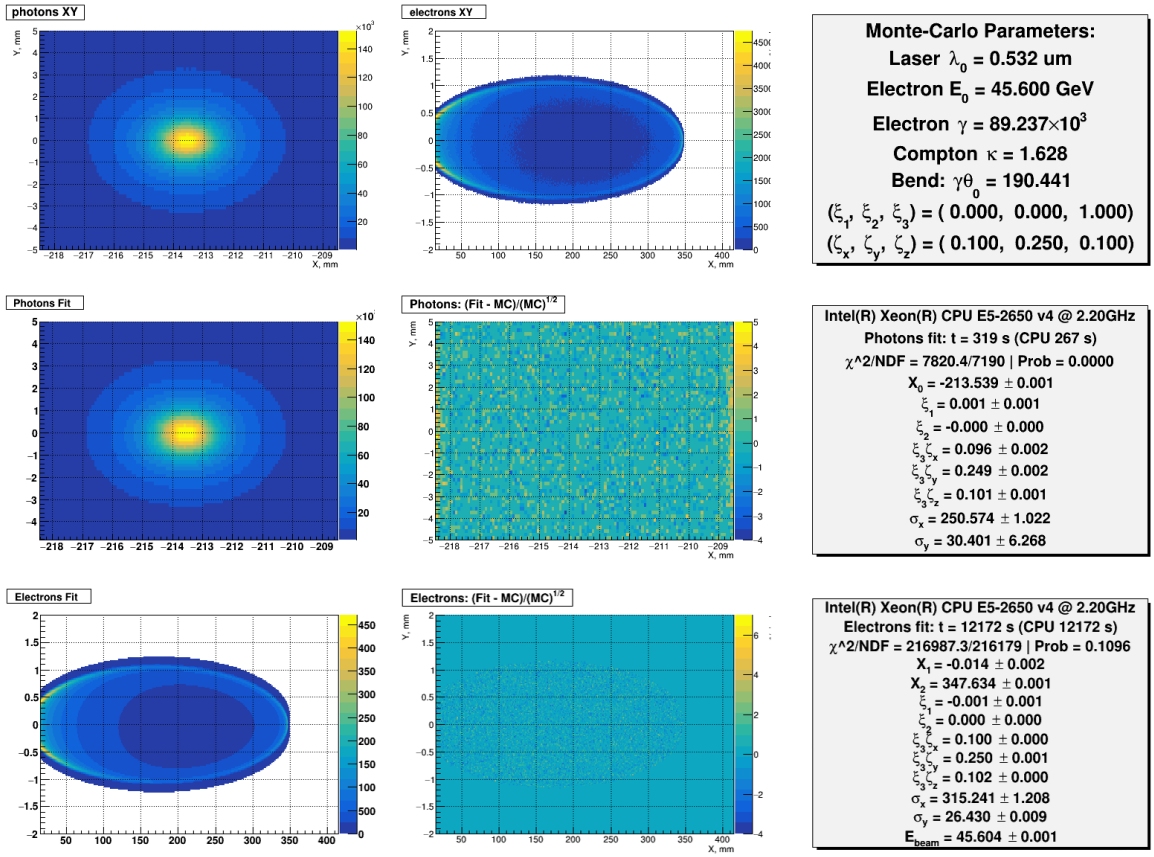

Figure 16: (Top) Simulated distributions of scattered (left) photons and (middle) electrons as they could be measured in a perfect detector. Electron beam emittance and dispersion is included in the simulation. Relevant parameters are shown in the top right box. Fit results are shown on the second line (distribution on the left, residuals in the middle, relevant parameters on the right). Similar results for electrons on the bottom line. Statistical precision on the polarisation parameters is within a per-mille.

for these measurements would be to achieve a 1% statistical precision every second, but this target requires further investigation.

- A complementary way to measure the beam-energy is to perform a so-called free spin precession (FSP) measurement. It is based on the rapid resonant rotation of the electrons bunch' spins into the horizontal plane of the collider ring and following their subsequent free rotation around the equilibrium vertical direction [39].This type of measurement can be made very quickly (few thousand turns) and could follow directly after the RDP measurement, in which the depolariser will have rotated the polarisation vector into the horizontal plane, rather than actually depolarising the bunch completely. It is possible that in the FSP measurement, the bunch will require an increased laser pulse intensity than during the RDP measurement to reduce statistical errors, but this requires further investigations.

- Monitoring of level of the longitudinal polarisation of the colliding bunches is necessary

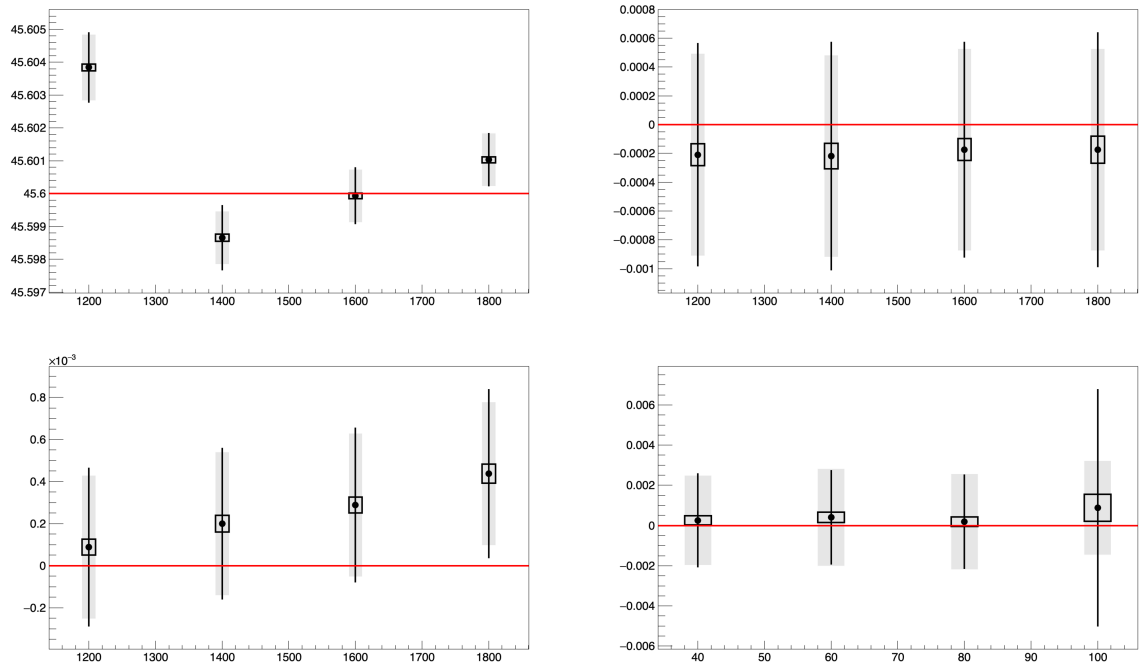

Figure 17: Results of a toy Monte-Carlo (100 experiments of 100 million scatters each) for (Top-left) the direct extraction of beam energy (in GeV) from scattered particles profiles, (Top-right) vertical electron beam polarisation measured with electron detector, (Bottom-left) longitudinal electron beam polarisation measured with electron detector and (Bottom-right) horizontal electron beam polarisation measured with the photon detector. Red-line show the generated value. Dots represent the mean of the fit results and the box its uncertainty. The grey band is the average of the single fit uncertainties, and the black line is the standard deviation of single fit values. The horizontal axis represent different choices of the number of horizontal pixels of the electron detector (photon detector for the bottom-right plot). The electron (photon) detector size is taken to be 400 mm^2 (10 mm^2). Simulated pixel numbers correspond to $(1200 \times 40, 40 \times 40)$, $(1400 \times 60, 60 \times 60)$, $(1600 \times 80, 80 \times 80)$, and $(1800 \times 100, 100 \times 100)$ for the electron detector (horizontal$\times$vertical axis and photon detector respectively).

as any longitudinal polarisation will 'pollute' the electroweak observables at the Z pole. Preliminary studies suggest that this component of the polarisation vector should be known to 10^{-5} absolute, or known to be less than this level. This extremely demanding requirement is somewhat softened on the assumption that the longitudinal component will always be much smaller than the transverse component, and therefore constraining the latter to, say a few 10^{-4}, will probably therefore be sufficient. The polarimeter should be designed such that 10^{-4} systematic uncertainty is a feasible goal. We retain 10^{-5} as the target for the statistical precision, which should be the average uncertainty over all the colliding bunches during some reasonably short period of time. The choice of parameters for the scattering rate per bunch, and the number of bunches probed at the same time will be decided at a later stage. It will result from a compromise between the ability to keep accurate control and monitoring of the laser polarisation under relatively large laser power due to thermal effects, the need to have enough scatters per bunch crossing to keep sensitivity to polarisation parameters, especially due to background contributions. RDP and FSP energy calibration using one of the pilot bunches could eventually happen at the same time as for several physics bunch polarisation measurement. Nevertheless, feasibility still needs to be investigated.

- Physics places some requirement on the position of the polarimeters. For example, the concerns related to the level of longitudinal polarisation in the colliding bunches mean that the orientation of the polarisation vector, ν_0, should not be allowed to evolve significantly between the measurement and the experiments, and motivates placing the polarimeters close to one of the interaction regions. However, other considerations might instead point to a location before the beam passes through the RF system (*i.e.* upstream) as being more suitable. Background sources and levels need careful studies prior finalizing the polarimeters location. The question of desired full-time access to the laser source (24h/7d) is also a strong constraint on the polarimeter integration concerning civil engineering. Studies are ongoing to resolve this question and find the best suited position on the rings to install both polarimeters.

- Knowledge of the relative positions of the scattered electrons, back-scattered photons, and electron beam allows for a real-time measurement of the beam energy [36]. This measurement is valuable for many applications, and may be essential for some studies. For example, when running at $E_{\mathrm{CM}} = 125$ GeV it will be essential to track any energy variations of the order of 10^{-4}, in order to keep the collision energy sufficiently close to the pole of the Higgs resonance. According to the polarimeter design outlined in Ref. [40] this precision can be obtained with around 10s of data taking, which is at the higher end of what is required. However a dedicated study still has to be performed at 125 GeV center of mass. The estimates must also be updated once a realistic implementation of the polarimeter in found, since it is expected to slightly depend on the distance between the edge of the detector with the nominal beam position.

- Another requirement is being able to switch between energy modes without physical intervention on the polarimeter instrument itself. We would need to extend the polarimeter chamber width with increasing energy range expected from the instrument. Indeed the polarimeter is a spectrometer and the Compton electron pattern enlarges

with increasing beam energies. Therefore the much larger size of the needed instrument and the more stringent constraint on background due to higher SR critical energy may lead us to consider the use of the polarimeter for the $t\bar{t}$ mode operation. It will nevertheless be maintained for some short interleaved Z calibration fills.

9.2 Technical specification and challenges

A schematic of the FCC-ee polarimeter is shown in Fig. 18. A dedicated laser/lepton-beam interaction chamber of two meters provides Compton collisions for the polarisation measurement. The 26 m dipole magnet used as a spectrometer to separate the Compton collision products from the main beam, is already part of the magnets of the collider ring optics. This 2 mrad bending magnet provide both a way to steer the main beam, while separating the Compton electrons from it since they have lost energy during the collision process. On the other hand we can detect the Compton photons that have not been deflected and are coming straight from the laser IP. The Compton scattered electrons and photons will travel under vacuum for about 100 m to be separated in a field-free region before heading out of vacuum through an extraction window to be detected outside. Thanks to the relatively large beam to beam transverse separation at 830 m upstream of the experimental IPs, and the presence of a long field-free region following the last dispersion suppression dipole, this layout can be accommodated in the baseline collider optics design.

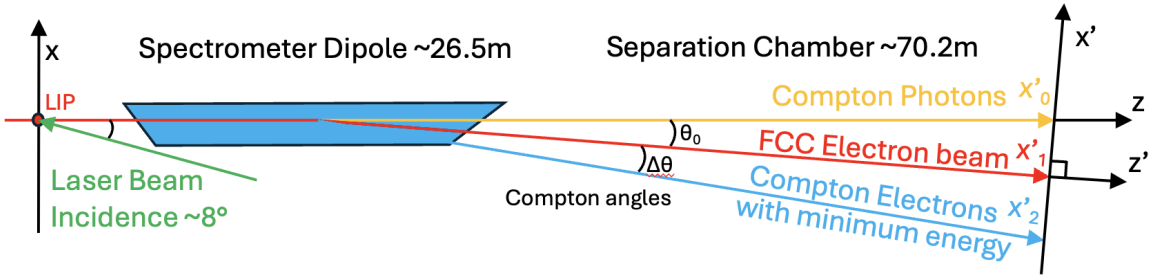

Figure 18: Schematic drawing of the FCC-ee polarimeter. Laser interaction point at xz reference frame. Compton products sensors at x'z' frame, more details in reference [40].

9.2.1 Laser

Physics requirements for the polarimeter mean that the laser system be reliable, remotely operable, and versatile in terms of laser intensity and temporal pattern of train of pulses. It is currently planned to use a laser with a wavelength in the green, as a compromise between the required length of the field-free region and the reliability of the laser system itself. Indeed a UV laser system would provide a much more compact polarimeter but would be much more risky in terms of reliability and versatility. Use of an infrared laser would also provide the reliability and would likely be easier to operate but would induce a twice larger free-field drift to measure the scattered particles with the necessary precision. Control and real-time monitoring of the laser polarisation will be needed with on-line calibrations, for example as already performed at JLAB [41]. However, an optical enhancement cavity was used there,

which allowed to more simply use optical reversibility theorems which facilitates the absolute calibration of the circular laser polarisation [42]. Such a system cannot be used in the case of FCC-ee since one must be able to hit single bunches. A careful conceptual study of the absolute calibration of the laser polarisation has to be realized. The calibration of the circular laser polarisation at the interaction point must be ensured at 10^{-3} for pilot-bunch measurements for RDP and FSP. The monitoring of the longitudinal polarisation however demands an accuracy down to a level of 10^{-4} or below that is unprecedented and will require careful evaluation of possible systematic biases. It will also necessitate experimental validation to confirm feasibility and robustness. Attention must be paid to possible major difficulties arising from multiplication of optical elements in the beam line, and the difficulty to calibrate the laser polarisation at the Compton IP. Detailed modeling and experimental studies remain to be done and must be planned for the next phase of the project.

Two possible laser systems are currently under consideration. Initially a Q-switched Nd:YAG laser system at 532 nm delivering few nanosecond pulses triggered at 3kHz was proposed for probing the pilot bunches for RDP and FSP measurements [19]. Operation of this laser with the colliding bunches would require probing a single bunch at a given time. Changing the phase of the trigger would be necessary in order to allow a different bunch to be probed. An alternative choice of laser system, which would not have this complication, would be an Yb based laser system seeded by a mode-locked oscillator. This oscillator would have a frequency that matches a sub-harmonic of the RF frequency of the collider and would be permanently locked to it. It could seed various amplification stages in parallel to deliver laser pulses at 3 kHz (a sub-harmonic of the RF) for the RDP and FSP with pilot bunches and bursts of laser pulses for the colliding bunches possibly at a higher repetition frequency. Optical pulse picking elements would be employed to ensure a proper time structure of the pulses. After amplification, frequency doubling would be implemented to deliver laser pulses at approximately 515 nm. Such a system would typically provide a few to several tens of picosecond laser pulses with a spectral bandwidth of a nanometre, or a little below.

It would be mandatory to have a dedicated, radiation-shielded and air-conditioned laser room installed in a bunker near to the Compton interaction point, which will host the laser system and electronics. The latest civil engineering studies point toward an integration of this laser hutch in the first big alcove of the arc. Control and monitoring of the laser position, pointing, profile, energy and polarisation will be implemented, with a transport line towards the interaction region, most likely under vacuum (or inert gas) in order to minimize perturbations. Moreover, the implementation of a relay imaging may likely be required. The optics that compose it require careful consideration. The length of this laser transport line will ideally be below 50 m, but will depend on the required crossing angle between the lepton and laser beams, the actual location of the laser room with respect to the interaction point and constraints related to the overall integration and operations of the system.

The choice and optimisation of the laser system depends on the following parameters:

- the pulse duration, its center wavelength and corresponding spectrum [36];
- the choice of the interaction plane and the value of the crossing angle of the two beams will affect the luminosity of the interaction and is therefore coupled to the choice made on the pulse duration;

- the transverse beam size at the interaction point that will affect the luminosity of the interaction and the (in-)homogeneity of the interaction probability among leptons within the bunch, which is also dependent on the crossing angle and the laser pulse duration;
- the single pulse energy of the laser for pilot and colliding bunches, which affects the scattering rates and thus the statistical precision of the measurements;
- the laser polarisation in-homogeneity on the wavefront which must not exceed 10^{-4};
- the beam quality, for which a specification remain to be set.

This optimisation will also depend on the parameters of the lepton beam at the interaction point.

As demonstrated in Ref. [36], the beam energy can be extracted directly from the measurement of the distribution of the scattered electrons and the position of the photon beam on the detector. It is shown that it may be possible to do so with a relative precision and accuracy of few 10^{-5}. This measurement, being continuous and available in real time, is complementary to those performed with RDP and FSP. It also opens the possibility to monitor beam-energy variations with the same apparatus for pilot and colliding bunches continuously, even at energies beyond the WW threshold, where RDP and FSP measurements are no longer possible. However at higher energies, a significantly larger separation chamber width as well as a larger electron pixel detector will be needed.

The direct energy measurement may be affected by energy spread in the lepton beams and also the spectral bandwidth of the laser. In the absence of any frequency chirp, the RMS relative laser intensity spectral bandwidth is

$$\frac{\sigma_\lambda}{\lambda_0} = \frac{\lambda_0}{4\pi c \sigma_t}, \tag{13}$$

where σ_t is the rms intensity laser pulse duration. This quantity reaches 10^{-5} for $\sigma_t = 10$ ps, thus disfavouring smaller pulse durations. Larger pulse durations may be obtained by either cutting off part of the laser spectrum before amplification or by inducing a time-frequency chirp in the Yb laser pulse. The pulse duration is naturally of a few nanoseconds for Q-switched Nd:YAG technology. The requirements on the absolute stability of the spectrum implies controlling the average laser wavelength within a range of few hundreds of picometres. This may be done with commercial high accuracy wavelength meters [43]. If pursuing the modelock Yb laser oscillator approach, this control could be achieved by locking its spectrum on an atomic clock distributed over an optical fibre network, following the frequency-comb technology [44], as recently made available at CERN by the T-REFIMEVE [45].

The choice of the crossing plane of the lepton and laser beam must satisfy two contradictory requirements. On one hand, the horizontal plane has the disadvantage of being the one in which the synchrotron radiation is generated.

On the other hand, it is desirable to optimise the luminosity of the interaction, which, for a crossing angle in the horizontal plane, has the following dependence:

$$\mathcal{L} = \frac{f_{\text{rep}} N_l N_e}{2\pi\sigma_x\sigma_y\sqrt{1+\frac{\sigma_z^2}{\sigma_x^2}\tan^2\frac{\theta}{2}}}.$$

Here N_l (N_e) is the number of particles in the laser (lepton) beam, $f_{\rm rep}$ is the frequency of collisions (here 3 kHz), $\sigma_i = \sqrt{\sigma_{i,l}^2 + \sigma_{i,e}^2}$ with $i = x, y, z$ is related to the laser and electron RMS beam sizes in the three coordinates of the reference frame of the lepton beam, and θ is the crossing angle in between the two beams ($\theta = 0$ for contra-propagating beams). In order to avoid large variations over their phase space of the interaction probability, it is advisable to choose the laser beam size to be two to three times larger than that of the leptons. Given the small vertical emittance of the lepton beams at FCC-ee, the vertical lepton beam size is small. Reflecting this ellipticity on the laser beam is possible to some extent thanks to the use of cylindrical lenses. However the Piwinski contribution to the luminosity, $\frac{\sigma_z^2}{\sigma_x^2}\tan^2\frac{\theta}{2}$ would induce a large luminosity reduction for a crossing in the vertical plane. These considerations lead to the decision to implement crossing angle in *both* the horizontal and vertical planes.

For the Q-switched Nd:YAG laser option, the pulse duration of several nanoseconds imposes that the crossing angle should not exceed a few milliradians, in order to maintain a sufficiently high luminosity. It implies that the laser must be injected through the spectrometer dipole which imposes some additional integration constraints. The shorter pulse of the Yb modelock laser allows for crossing angles of several degrees. The choice of the crossing angle and pulse duration combination also affects the stability of the luminosity due to possible jitters in the laser direction of up to 100μrad. Indeed the luminosity variations for given angular fluctuations of the crossing-angle θ, for beams crossing either in the horizontal or vertical planes, reads

$$\frac{\sigma_{\mathcal{L}}}{\mathcal{L}} = \frac{\frac{\sigma_z^2}{\sigma_{x,y}^2}\tan\frac{\theta}{2}}{1+\cos\theta+\frac{\sigma_z^2}{\sigma_{x,y}^2}(1-\cos\theta)}\sigma_\theta. \tag{14}$$

The numerical calculation is represented in Figure 19. It shows that for 100 μrad pointing stability, a relative luminosity fluctuation of about 2.5% is expected for the Q-switch option while it is a factor 100 smaller for the modelock laser option, despite a much larger crossing angle.

The laser arrival of the laser pulse at the Compton interaction point must be correctly adjusted relatively well. The luminosity indeed scales as $\exp\left(-\frac{\delta t^2}{2\tilde{\sigma}^2}\right)$ where $\tilde{\sigma} = \frac{\sqrt{\sigma_x^2+\sigma_z^2\tan(\theta/2)^2}}{c\tan(\theta/2)}$ and δt is the systematic laser pulse delay with respect to the lepton beam. Fluctuations of arrival time of the laser at the interaction point Δt further induce, in average, a reduction of luminosity of $\frac{\tilde{\sigma}}{\sqrt{\tilde{\sigma}^2+\Delta t^2}} \approx 1 - \frac{1}{2}\frac{\Delta t^2}{\tilde{\sigma}^2}$. These two contributions are shown in Fig. 20. As expected, it is sufficient to require that the temporal jitter and systematic timing error are both much smaller than the laser pulse duration.

The values of the beam parameters depend on the location of the polarimeters. Close to the IP, the beam size is expected to be $\sigma_{x,e} = 525\,\mu$m and $\sigma_{y,e} = 11\,\mu$m. The bunch length is expected to be 4.3 mm for pilot bunches and 15.4 mm for bunches in collision. Table 3 shows a tentative set of parameters for both choices of laser, and for both pilot and colliding bunches in the case of the modelock Yb technology. The parameters assume a location for the polarimeter close to the IP, and populations of 10^{10} for the pilot bunches and 25×10^{10} for the colliding bunches. Here ten colliding bunches are probed, but this number can be increased if higher laser power is available. If the polarimeter is located close to the interaction point then the parameters would have to be adjusted to match the reduced horizontal beam size.

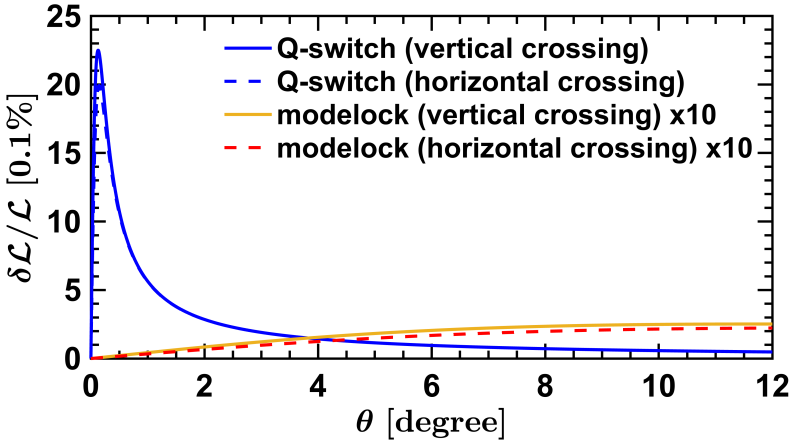

Figure 19: The relative variation of luminosity for the two types of considered lasers ($\times 10$ for the modelock option for better visualization) and their related configuration of interaction region for an angular pointing stability of 100 μrad. It is shown assuming either beams crossing either in horizontal or vertical planes. Results are similar since effective beam size is dominated by the laser beam size.

The relative luminosity defined as $(1 + \frac{\sigma_z^2}{\sigma_x^2} \tan^2 \frac{\theta}{2})^{-1/2}$ for the two laser options are shown on Fig. 21. The crossing angle for the modelock laser can be adjusted according to integration constraints on a few degrees range.

9.2.2 Vacuum chambers and magnet

Monte Carlo simulation models are under development to evaluate and optimize the expected polarimeter capabilities. It comprises the design of the laser/beam interaction chamber, the separation chamber of almost 100 m, and the detector systems foreseen to record the Compton products. While a preliminary estimation have been performed by the means of a Toy Monte Carlo model as used in Ref. [36]. Complementary models have recently been developed using BDSIM Ref. [46], a Geant4 based software performing Monte-Carlo particle-matter interactions. The design of the instrument is being optimized thanks to these models.

- The laser/beam interaction chamber (LIP), see Fig. 22, will be made out of a typical FCC beam pipe profile, and feature two tapping tubes on a diagonal axis holding viewing ports to allow the laser beam in (and out) the chamber. The design will be very close to the one developed for the SuperKEKB Compton polarimeter [47]. The crossing design angle in the horizontal plane is expected to be (8-12 deg). The vertical angle is not yet defined, but might be similar. This laser interaction chamber will be placed right before the spectrometer dipole magnet. An optical table will be installed underneath the LIP chamber to support the laser mirrors in the most stable way, materially decoupled from the beam pipe which could transport vibration from elsewhere (water cooling, etc.).

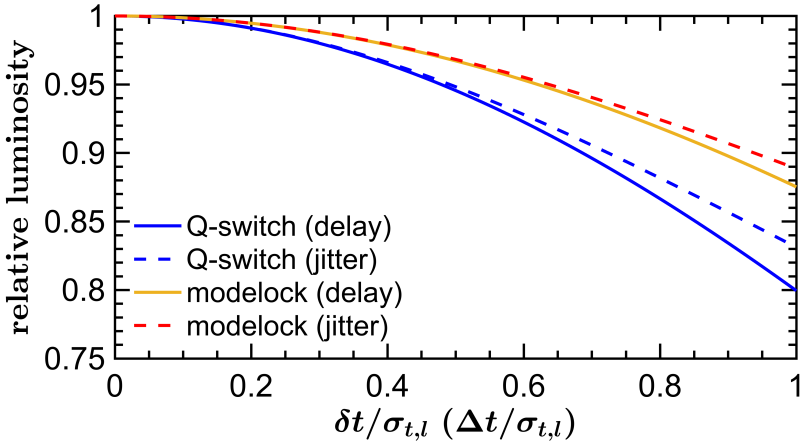

Figure 20: The relative luminosity of the Compton interaction as function of the (solid lines) systematic delay of arrival of the center of the laser pulse at the interaction point with respect to the center of the electron beam; and (dashed lines) temporal jitter of the laser beam for a perfectly well synchronized laser. It is shown for both Q-switch laser (blue lines) and modelock laser (red and orange lines).

- After the LIP the so-called separation chamber begin. The geometry of this chamber basically starts from the FCC profile beam pipe, and goes over almost 100 m with the winglets enlarging along the path. Thanks to the dipole field present over the first 26 m, the Compton photons and electrons will channel through the winglet and be separated from the main beam along the way. For now it is assumed that a standard dipole in the FCC-ee lattice will be adequate, but it is possible that requirements on field homogeneity *etc.* will demand a custom-made solution.

- Following this dipole field region, the Compton products will continue their drift on about 75 m in free field propagation. Along this path the winglets continue to expand transversely up to about 300 mm from the main beam axis. Mu-metal shielding might be needed along this free field region to get rid of the earth geomagnetic field, and other local machine related magnetic fields that might disturb the Compton electron propagation.

- The Compton products will eventually cross the extraction windows to get detected out of vacuum. The thickness of this exit window is a compromise between the extinction ratio of incoming synchrotron radiation (SR) background, and the scattering of the signal from the Compton products generating a loss of information. Due to the very large amount of SR generated by the bunch when crossing a few upstream magnets, a dedicated study is ongoing to optimise the exit window thickness. Together with the use of SR radiation absorbers upstream of the laser interaction point to reduce the contribution of SR photons from upstream magnets ongoing internal reflections and reaching the extraction window. To give the reader an order of magnitude, without absorbers, each electron from the bunch will radiate about 2 photons reaching the extraction window surface. According to the bunch population of the order of 10^{11},

Table 3: Preliminary laser parameters for pilot and colliding bunches. Note that single bunch charges are different for pilot and colliding bunches.

Technology	Q-switch	Modelock Yb	Modelock Yb
Bunch type	Pilot	Pilot	Colliding
Repetition frequency	3 kHz	3 kHz	3 kHz
number of targeted bunches	1	1	10
Pulse energy	3 mJ	3 mJ	50 μJ
Average power	9 W	9 W	1.5 W
Pulse duration	3 ns	30 ps	30 ps
Beam width ($\sigma_{x/y,l}$)	1 mm	1 mm	1 mm
Crossing angle	2 mrad	8 deg	8 deg
Scatters per bunch crossing	260	290	94
Scatters per second	8 10^5/s	9 10^5/s	28 10^5/s

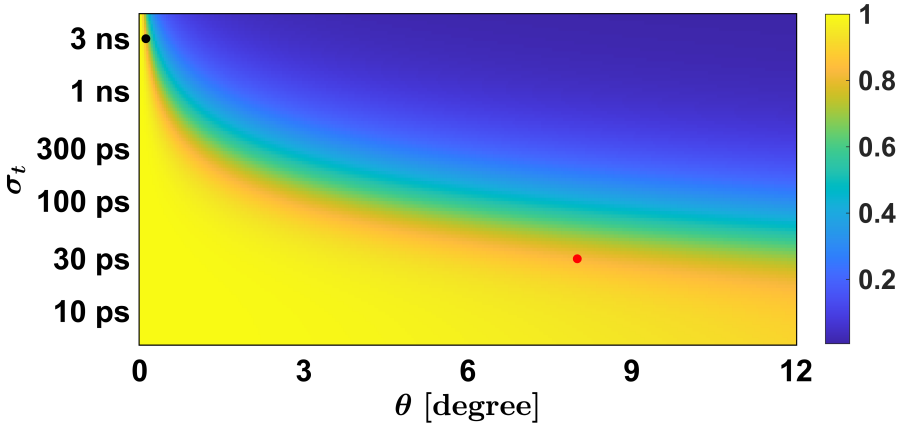

Figure 21: The relative luminosity as function of the laser pulse duration and the crossing angle for interaction with pilot bunches. The solutions listed in Table 3 are shown with the black (red) dots for Q-switch (modelock) lasers.

selecting a few hundreds Compton products into this important SR background seems to be a challenging task. Mitigation of this background will also come from the detector design itself.

- The effect of the polarimeter's vacuum chamber, and the extraction window shape on the collider ring beam-impedance has been evaluated using CST Studio Suite electromagnetic simulation software. First results on the most advanced chamber models have shown a minor contribution of the polarimeter chamber to the overall impedance budget of the FCC-ee machine. As shown in Fig. 24, the impedance fall bellow 0.01% of the total machine impedance. In turn, the ongoing design is not constrained by such aspects and that allows some welcome freedom for further geometrical optimisations. One of the polarimeter chamber geometries simulated in CST is shown in Fig. 23.

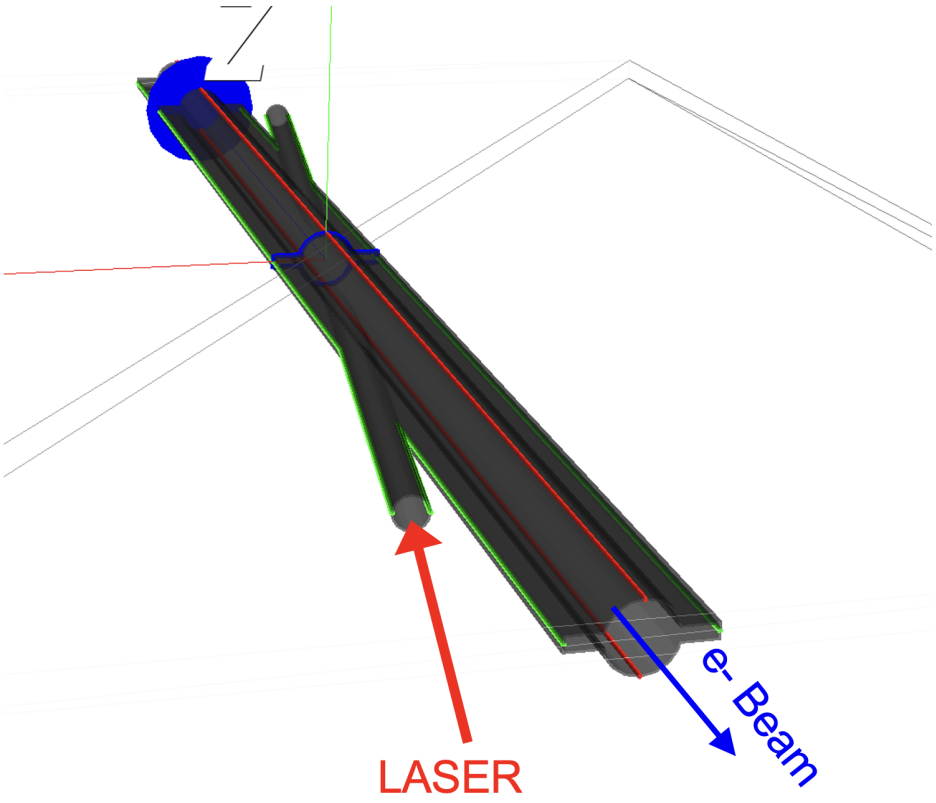

Figure 22: Pre-Design of the laser interaction chamber used for simulations.

9.2.3 Sensors

Two types of detector assemblies are needed for the polarimeter. The first one aims to record the transverse ellipse of the Compton scattered leptons over a surface of about $5 \times 300\,\mathrm{mm}^2$ for the Z mode and twice this width for the W mode. The second sensor will record the peak shaped distribution from the Compton gammas on a detector of about $10 \times 10\,\mathrm{mm}^2$ transverse area, probably organised as for a multilayer sampling calorimeter. The baseline design for the Compton polarimeter detectors aim to use pixelated sensors to record precisely both photons and electrons transverse distribution patterns ($18 - 50\,\mu$m pitch). These sensors will be developed thanks to the recent advances in calorimeters and silicon detector development for HL-LHC and future FCC experiments. No choices have been made concerning the exact type of sensor substrate and design. This will come out of a study benchmarking with existing sensor responses using the appropriate digitisation software to compare them for the polarimeter application needs. Monolithic active pixel sensors (MAPS) recently developed for the ALICE ITS3 upgrade [48] could be a good choice for fitting the electron ellipse pattern into a single sensor unit (for the Z mode) see Fig. 25.

A particle matter interaction software named BDSIM [46] has been used to get closer to a real data set as compared to the ideal pattern presented before as simulated by the Toy Monte Carlo model used to develop the polarimeter concept and the fitting procedure. The BDSIM model simulate the Compton interaction between the lepton beam and the laser then it propagate the Compton products through the bending spectrometer dipolar field under vacuum up to the extraction window. The material thickness making this window is a

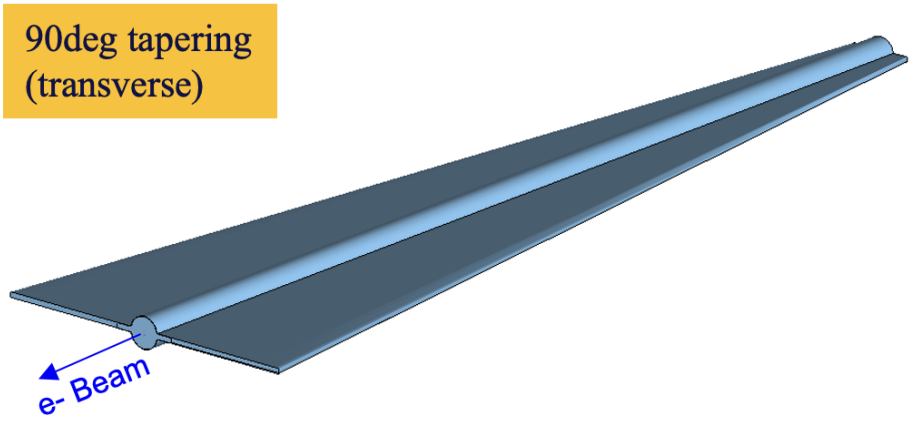

Figure 23: Design geometry of the separation chamber the extraction window is the flat surface (bottom-left) as simulated in CST studio suite. The FCC-ee lepton beam (in blue) would circulate from the top-right to the bottom-left sides of the object.

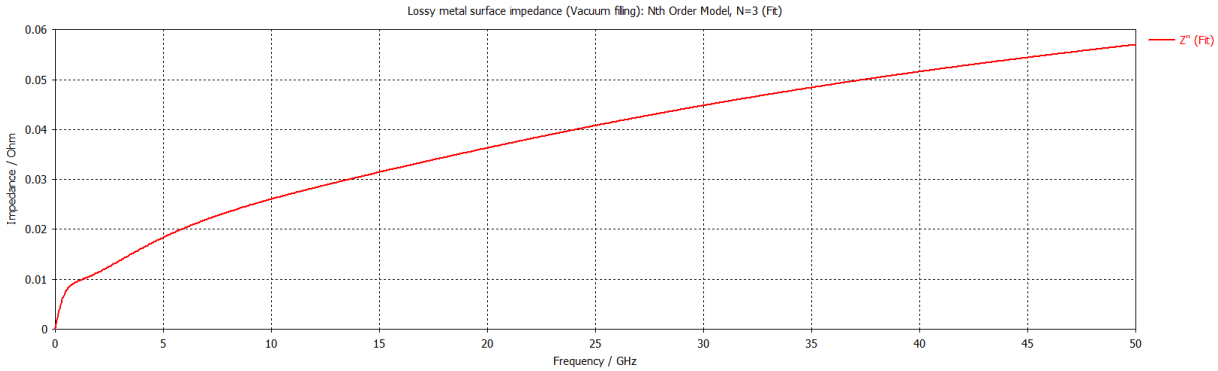

Figure 24: Impedance of the polarimeter separation chamber as simulated using CST studio suite.

compromise between the detrimental effect of multiple scattering of the Compton products, and the shielding against lower energy background particles. The first outcomes of this study on the Compton electrons shows that crossing 1 mm of copper window would not degrade much the expected pattern in the silicon sensor if it is installed close enough.

The model also simulate and record the pattern obtained from the energy deposition in a silicon layer used as sensor volume just subsequent to the extraction window. Event by event the deposited energy is computed and stored in a 3D mesh. A post processing code to model the silicon device behaviour is then applied to this dataset to simulate the sensor response and efficiency. Manly a threshold that select when to trigger a pixel on, and the dead zones of the MAPS sensor (reticulated set of pixel matrixes with gaps). The final picture shows what we should expect as signal from the sensor in order to apply the fit, see Fig. 26. The background in this image is produced by the scattering of the Compton products in the exit windows. Yet other backgrounds from the machine need to be considered to get the full picture.

At this stage the second sensor dedicated to the Compton photons is not yet modelled.

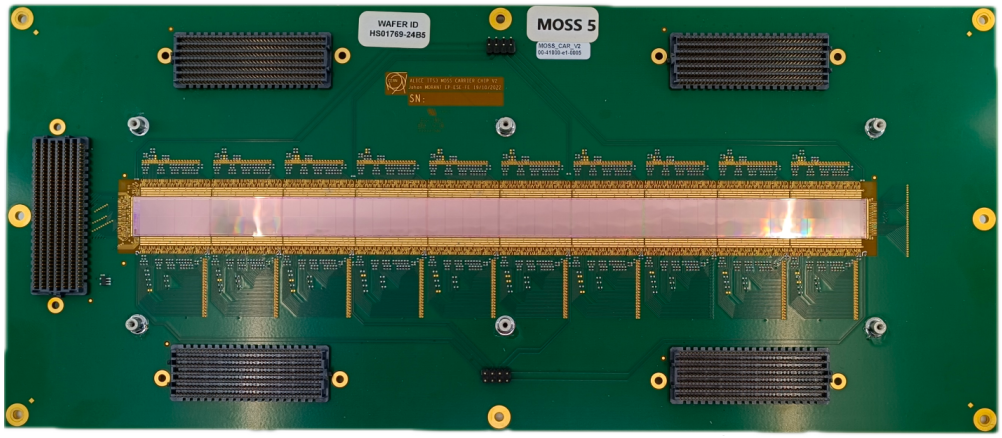

Figure 25: MAPS sensor development for the ALICE ITS3 upgrade.

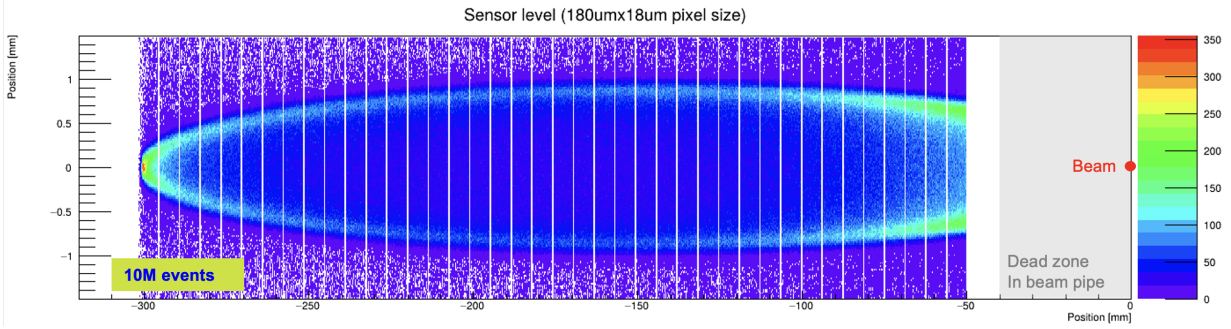

Figure 26: Simulated Compton electrons energy deposition in a MAPS silicon sensor. The vertical polarization level of the bunch is set to 0.5 creating an up-down asymmetry. White lines corresponds to dead zones of the sensor.

Since these photons are of very high energy they will need to undergo conversion in absorber materials layered with sensors planes in order to develop an electro-magnetic cascade. Since we expect between 300-1000 Compton events per bunch crossing they will most probably all fall into the same time-stamp. In that case we do not plan to perform single photon calorimetry but more aim toward building the best possible energy deposition profile.

9.2.4 Background mitigation

As introduced before, a strong synchrotron radiation (SR) background is expected to reach the extraction window as shown Fig. 27. For the measurement of the scattered electrons, techniques using multilayered pixelated sensors could be used in order to perform basic tracking over a few layers and get rid of the photon background in the sensors. This kind of mitigation techniques could be an option to improve on the signal to noise ratio of the Compton profiles. If it is not sufficient, technologies of lower spatial resolution but much less sensitive to SR photons such as the ones based on Cherenkov radiation by charged particles, could be another way of performing the Compton electron detection with greater selecting power, as initially planned at ILC [49]. Such a device would allow to perform energy

calibration like RDP and FSP, but might be weak for direct energy measurement techniques and precise knowledge of the polarisation vector. Other sources of background like beam-gas Bremsstrahlung, Compton interaction on the thermal photons and backgrounds coming from nearby experiment's IP will also deserve careful consideration.

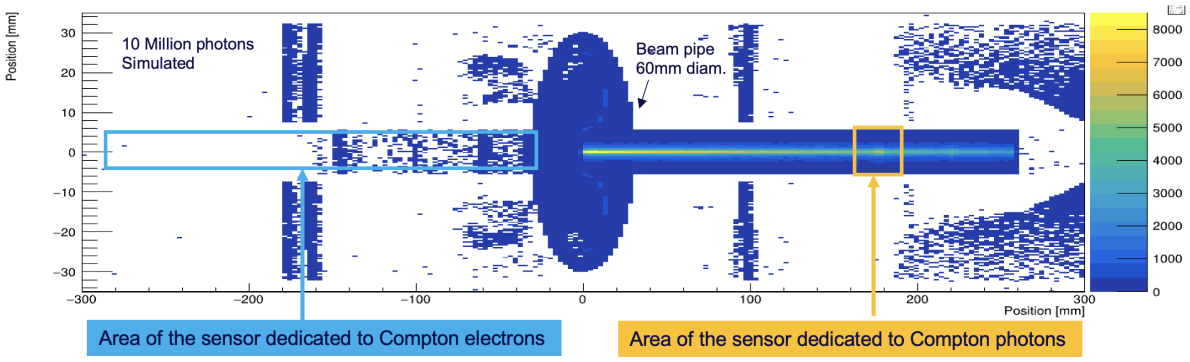

Figure 27: Synchrotron radiation background expected in the transverse plane at the location of the polarimeter sensors.

9.2.5 Polarimeter system availability and efficiency

The Compton polarimeter availability for RDP energy calibration is required to reach 95% for the Z and WW modes of operation. Such an unprecedented goal is a real challenge and work is still on going to make sure we can reach such instrument uptime. Up to now the most critical part of the polarimeter has been identified to be the laser source and the transport of the laser beam toward the interaction point with the lepton beams, with the related high accuracy monitoring of the laser polarisation to ensure the level of systematic uncertainty. Multiple radiation-compatible systems will have to be developed to monitor the circular polarisation level along the laser transport line. The objective is to have a fully remotely controlled system, where we could steer, monitor and re-adjust each of the optical elements. Radiation levels expected in the tunnel represent a major constraint since off-the-shelf optical devices are not radiation hard.

Despite modern laser technology having gained in robustness and performance, operational constraints at FCC-ee and in general in accelerator environments are specific. In particular, some parts of the foreseen laser system may require interventions from time to time to ensure the performance and operational constraints are met. For reference, experience at the LEP and other facilities have proven that full time access to the laser hutch while the beam is circulating is a must to allow a smooth set-up of the instrument to the best working conditions and guarantee system availability. For that purpose, a dedicated tunnel to access the polarimeter laser hutches on a 24h/7d basis while the machine is running would be an asset. In order to overcome this difficulty it is planed to develop a mock-up system of the full laser line in the pre-TDR phase, and attempt to run it over long periods with desired circular polarisation precision to gain experience. That would be a way to optimise the whole set of remotely controlled actuators in order to be able to assert the best up-time performance for the FCC polarimeter laser system. Nevertheless, the unavoidable downtime

due to access needs of the polarimeter laser still needs to be evaluated for a laser system similar to that of FCC-ee polarimeters.

Another solution to overcome this challenge wouldbe to invest in redundancy, having polarimeters in two experimental IPs for each beam. In case one is failing we can still rely on the second instrument before having a long enough access to fix any problem. This approach is adopted as baseline for the Feasibility Study. Another possible redundancy level could be to have a duplication of laser systems in each hutch and to be able to switch between two laser sources by remotely inserting a mirror on the optical path. But in any case the commissioning of the system without access still requires dedicated studies, if it is not revealed to become a showstopper for the required availability of the energy calibration.

10 Polarisation studies at KARA storage rings

Beam-energy measurements based on resonant depolarisation (RDP) were carried out at various previous collider rings, including VEPP-2M [50], VEPP-4M [51, 52], CESR [53], and LEP [54]. The change in polarisation occurs when the slowly varied excitation frequency f_{dep} of the depolariser, modulo an integer multiple of the revolution frequency f_{rev}, coincides with the spin precession frequency $f_{\mathrm{spin}} = f_{\mathrm{rev}}\nu_0$,

$$f_{\mathrm{dep}} = (k \pm \nu_0)\, f_{\mathrm{rev}} \quad \text{with} \quad k \in \mathbf{Z} \quad , \tag{15}$$

where the ideal spin tune ν_0 depends on the average beam energy, or Lorentz factor γ, according to

$$\nu_0 = a_e\, \gamma \ , \tag{16}$$

with $a_e = (g_e - 2)/2 = 1.159652... \times 10^{-3}$ the anomalous magnetic moment of the electron (with g_e the g-factor). The studies presented here have been carried out at KArlsruhe Research Accelerator.

10.1 KARA Machine Description

Located at Karlsruhe Institute of Technology (KIT), KARA is a synchrotron light source and test facility with a circumference of 110 m and an 500 MHz RF system. KARA is a machine ramping in beam energy from 0.5 to 2.5 GeV. It features a four-fold super-periodicity, where each sector consists of two double bend achromat (DBA) cells, with straight sections in-between, hosting, the RF system, injection magnets or other insertion devices. The double DBA optics for one quarter of the KARA ring is shown in Fig. 28.

No polarimeter is currently installed in KARA, however, depolarisation can be detected through a sudden change in the beam lifetime, and in the associated local beam losses. The reason is that the KARA beam lifetime is dominated by the Touschek effect, and the underlying Möller cross section and resulting local beam losses depend on the degree of beam polarisation. In a high-energy storage ring, beam polarisation increases the Touschek lifetime, by up to 23% [55, 56]. More details have already been reported in [57, 58]. Complementary to RDP scans, measurements characterizing the machine orbit and optics have been performed where a detailed summary is given in [59].

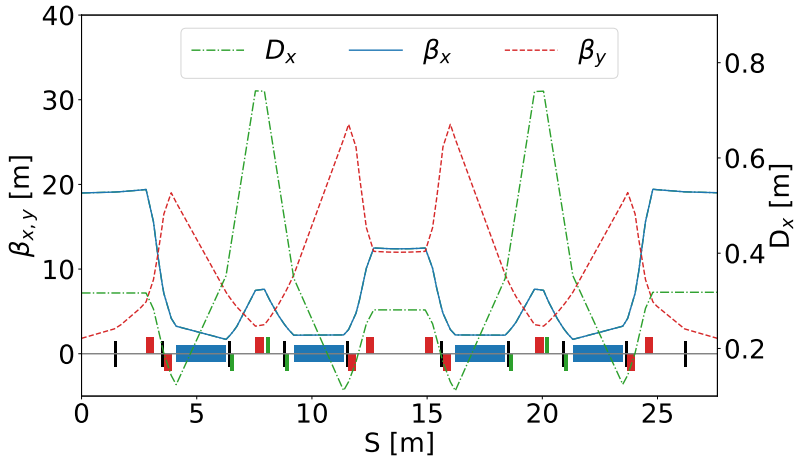

Figure 28: β-functions and lattice of the first quarter of KARA light source. Focusing (defocusing) elements are shown above (below) the horizontal axis.

10.2 RDP measurement set-up

Measurements presented here were performed at 2.5 GeV beam energy, where the Sokolov-Ternov polarization time is roughly 10 min. In order to a achieve sufficient level of polarization to perform RDP scans it is found necessary to wait at least 20 min in-between scans. The total beam current during measurements of 35 to 65 mA has been distributed over roughly 30 bunches with a filling pattern shown in Fig. 29. From the average reading of the BPMs a rms closed orbit of 125 and 125 m has been measured, respectively, for the horizontal and vertical plane.

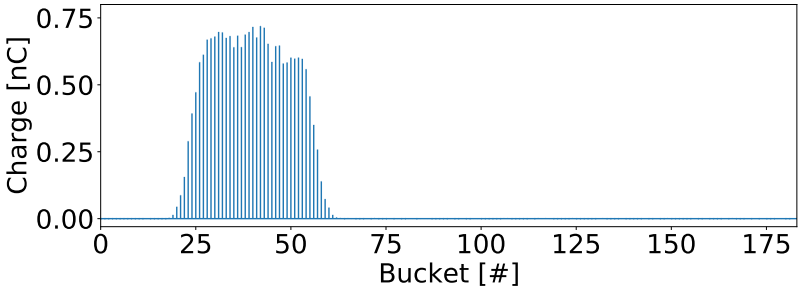

Figure 29: Bunch filling pattern during optics measurements.

Figure 30 presents a typical scan result, where the depolariser frequency is swept from 1.705 to 1.735 MHz over 650 s and we observe the change in the local loss rate. The depolarising frequency, f_{dep}, at which the loss rate changes gives the spin tune via Eq. (15), so that f_{dep} can be converted to an equivalent beam energy E using Eq. (16). For the example of Fig. 30, f_{dep} is 1.7139 MHz, with an equivalent beam energy of roughly 2.48 GeV. To simplify the plots, we omit plotting the frequency and only show the corresponding beam energy. Furthermore, since initial measurements indicated a beam energy of about 2.48 GeV, we now vary the depolariser frequency only from 1.705 to 1.725 MHz. The measured loss

rates as a function of E are fitted to

$$F(E) = F_0 + (h/2)\ \mathrm{erf}\left((E - E_0)a\right) + bE + cE^2\ , \tag{17}$$

where the fit parameter E_0 corresponds to the centre of the step, and, hence, to the inferred beam energy. For the fitting, we used the Python function *curve_fit*, available from the *scipy* package [60], which implements a nonlinear least-squares method based on the Levenberg-Marquardt algorithm. The parameters a, b, c, h and F_0 are also determined by this fit, including the respective errors. To suppress these numerical uncertainties, we introduced a moving average over 3 successively measured loss-rate data for further analysis, resulting in a very low fitting error in the order of a few keV (10^{-6} relative accuracy).

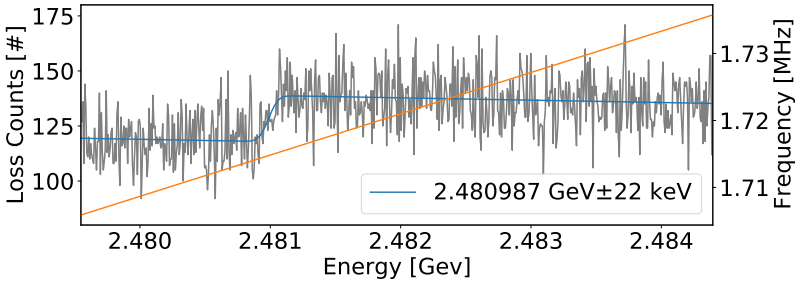

Figure 30: Typical depolarising scan result at KARA. Measured local beam losses versus the energy corresponding to the depolariser frequency. The stored beam current was approximately 35 mA. The orange line shows the applied Frequency in MHz (see right axis).

10.3 Dependence on the scan direction

The dependence of the result on the scan direction is of interest with regard to systematic errors. We executed measurements where the frequency either increased or decreased, while scanning the same range between 1.705 and 1.725 MHz. Here, we present results for scanning in either directions with a 400 s scan duration. Loss rates from these two scans are displayed in the top and bottom pictures of Fig. 31, respectively. Notably, the scan towards higher frequencies yields a significantly steeper change of loss counts, than the scan in the other direction. These findings are consistent with FCC simulations [61] for the case of a negative energy drift. When scanning towards higher frequencies the beam energy is drifting towards the depolarising frequency (on-coming), and, thus, the time required to complete the resonant depolarisation process is shortened compared to sweeping towards lower frequencies. For the latter case, the depolariser frequency is catching-up with the energy drift. Furthermore, we note that the beam energy inferred from the (later) downward scanning is 14 keV lower than for the (earlier) upward scan, which also hints at a negative energy drift.

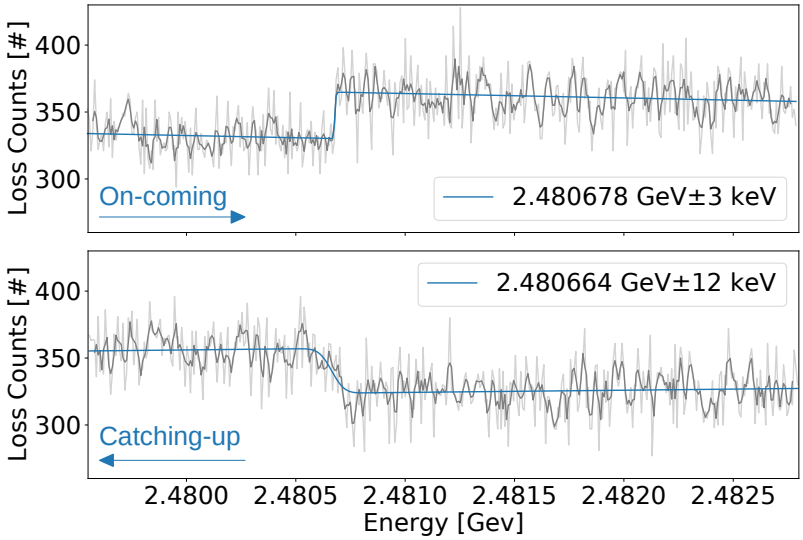

Figure 31: Scan results for increasing (top) and decreasing depolariser frequency (bottom) with the respective fit results shown. The different shape of the fitted function is consistent with a downward drift in beam energy.

11 From resonant depolarisation to centre-of-mass energies

The base measurement in the FCC-ee centre-of-mass determination is that of the spin tune by RDP as described in Section 8 [2]. The spin tune is directly related to beam energy

$$\nu_0 = E[\mathrm{MeV}]/440.6485 \tag{18}$$

for a perfectly flat machine without solenoids. This average energy determination is independent of the location of either the depolariser or the polarimeter, since it represents the average over the guiding magnetic field. We call $E^{\pm}_{\mathrm{RDP}}$ the energy obtained assuming a perfect machine by RDP. The relationship between $E^{\pm}_{\mathrm{RDP}}$ and the correct beam-energy average, $< E^{\pm}_{b} >$, comprises at least two sources of corrections and uncertainties:

- The corrections to spin tune due to alignment and magnetic imperfections in the lattice;
- The corrections to the RDP frequency due to the interference of spin resonances with the depolariser-induced resonance.

Both of these corrections are potentially spin-tune dependent, leading to possible point-to-point uncertainties. They must be studied, on one hand, by performing spin tracking simulations, where first results are given in Sec. 4. On the other hand, detailed simulations of the RDP process must be performed, and evaluated with the goal of finding workarounds to minimise or evaluate their effect and the resulting uncertainties. The result of these investigations could lead to modified experimental procedures or operating energies.

[2]The discussion in this section is equally applicable for a spin tune measured by FSP.

In order to go from the determination of $< E_b^{\pm} >$, to the centre-of-mass determination at each of the interaction regions, the following corrections and sources of uncertainties must be considered:

- The energy losses and gains around the ring, which include the losses from synchrotron radiation (40 MeV per turn at the Z pole) and the losses from longitudinal impedance (a few MeV per turn, depending on bunch population and bunch length);
- The beamstrahlung losses, which depend on the exact bunch population and thus are luminosity dependent;
- The combined effect of beam collision offsets and parasitic opposite sign vertical dispersion (OSVD);
- The beam-beam collective electromagnetic interaction effects, which modify the crossing angle and the centre-of-mass energy.

This section discusses these items, with the exception of the electromagnetic interaction effects, which are addressed in Sec. 12.

11.1 Energy losses and their control

Considering that there is only one common RF section for the electron and the positron ring, it is useful to define ${E_0}^{\pm}$ as the average energy of the electron or positron beam in that RF section. If the energy losses are distributed evenly around the ring, (or according to the four-fold symmetry) this number is nearly equal to $< E_b^{\pm} >$. In FCC-ee with the electron and positrons circulating in different magnetic lattices the energies of the two beams can be different.

The approximate size of the energy losses at the Z pole is as follows:

- The overall SR loss is $\Delta_{SR} \approx$39 MeV at the Z-pole with 45.6 GeV;
- The losses due to longitudinal impedance are summarised in Fig. 33, ranging from a fraction of MeV to 5 MeV, depending on bunch intensity and bunch length;
- The difference between the energy loss in the inside and external rings is commensurate with the beam crossing angle, $(\Delta E_{\rm SRi} + \Delta E_{\rm LIi}) - (\Delta E_{\rm SRe} + \Delta E_{\rm LIe}) \approx \frac{\alpha}{2\pi} \times 8\Delta_{\rm SR} \simeq 0.19$ MeV, with energy losses from synchrotron radiation (SR) or longitudinal impedance (LI) from the inside (index i) or external (index e) octants respectively, or from the beamstrahlung (BS);
- Further energy losses arise for colliding bunches from beamstrahlung and are up to 0.31 MeV per IP and per beam at the Z-pole.

The energy losses around the ring are sketched on Fig. 32. The total energy loss around each ring is equal to the energy gain from the RF-cavities

$$\Delta E_{\rm RF} = 4(\Delta E_{\rm SRi} + \Delta E_{\rm LIi}) + 4(\Delta E_{\rm SRe} + \Delta E_{\rm LIe}) + 4\Delta E_{\rm BS}. \quad (19)$$

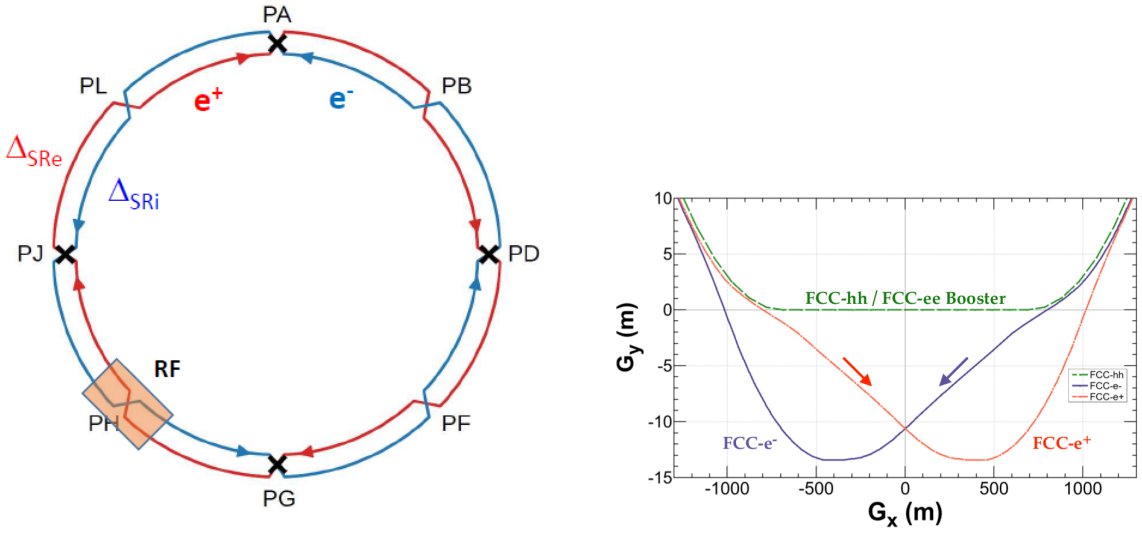

Figure 32: Left: Overview of the energy losses around the FCC-ee ring. Electrons circulate anti-clockwise and positrons clockwise. The beams enter the interaction regions from the inside. $\Delta_{\mathrm{SR_e}}$ and $\Delta_{\mathrm{SR_i}}$ correspond to the energy losses along the external and outside rings. Plot adapted from [62]. Right: Layout of the asymmetric layout of interaction regions with the beams entering from the inner side and outgoing on the external side with a larger deflection.

In practice it is be difficult to separate the longitudinal impedance and synchrotron radiation distributions, so we define $\Delta E_{\mathrm{Arc,i(e)}}$ as the energy loss along the inner or outer arc respectively, keeping in mind that these numbers will be different for nominal intensity colliding bunches, low-intensity polarisation pilot bunches or pilot bunches with higher intensity (orbit pilot bunches). The beam energies at the IPs are expressed as

$$E_J^- = {E_0}^- + \Delta E_{\mathrm{RF}}/2 - \Delta E_{\mathrm{Arc,i}} - \Delta_{\mathrm{BS}}/2 \ , \tag{20}$$

$$E_J^+ = {E_0}^+ + \Delta E_{\mathrm{RF}}/2 - 4\Delta E_{\mathrm{Arc,i}} - 3\Delta E_{\mathrm{Arc,e}} - 7\Delta_{\mathrm{BS}}/2 \ , \tag{21}$$

$$E_A^- = {E_0}^- + \Delta E_{\mathrm{RF}}/2 - 2\Delta E_{\mathrm{Arc,i}} - \Delta E_{\mathrm{Arc,e}} - 3\Delta_{\mathrm{BS}}/2 \ , \tag{22}$$

$$E_A^+ = {E_0}^+ + \Delta E_{\mathrm{RF}}/2 - 3\Delta E_{\mathrm{Arc,i}} - 2\Delta E_{\mathrm{Arc,e}} - 5\Delta_{\mathrm{BS}}/2 \ . \tag{23}$$

The energies at points G (resp. D) are similar to those for J (resp. A) above, and are obtained by exchanging the positive and negative particles. It follows from these equations, eliminating the total energy loss using Eq. 19, that

$$E_A^+ + E_A^- = E_J^+ + E_J^- = {E_0}^+ + {E_0}^- + \Delta E_{Arc,e} - \Delta E_{Arc,i}, \tag{24}$$

assuming that all energy losses are identical between similar arcs, and beamstrahlung at the IPs too, and hence, **all centre-of-mass energies are the same**. This is an important feature of the FCC-ee design which requires only one RF section for operation at the energies of the Z-pole, s-channel Higgs, and up to W-pair-production. Of course, achieving the desired precision will require careful assessment, by means of calculations and measurements,

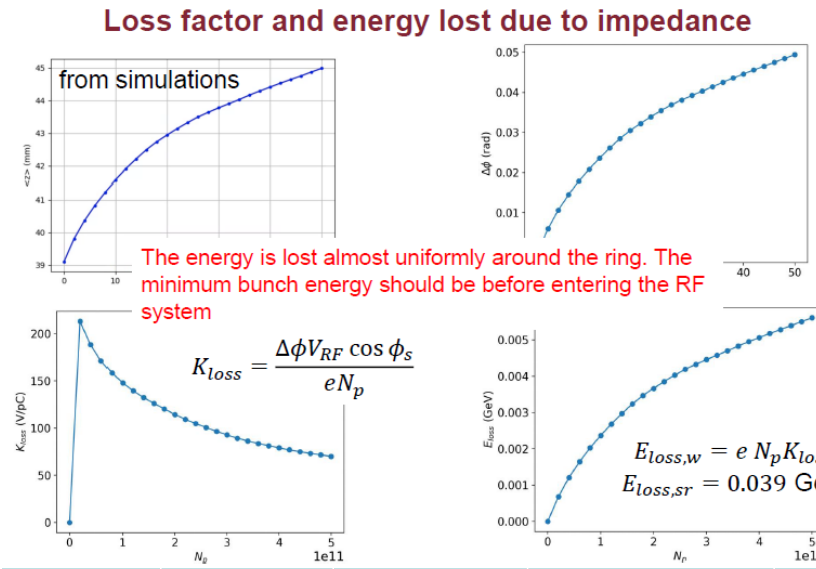

	Pilot bunch (3×10^{10} ppb)	Nominal intensity (2.6×10^{11} ppb)	Nominal intensity and beamstrahlung (2.6×10^{11} ppb)	SR
Energy spread	0.039 %	0.045 %	0.143 %	0.039 %
Energy loss	0.8 MeV	4.2 MeV	~ 1.6 MeV	39 MeV
Bunch length	5 mm	8.3 mm	17.2 mm	4.4 mm

Figure 33: Top: Calculation of energy losses from longitudinal impedance as a function of energy, beam intensity and bunch length. Bottom: summary for two categories of pilot bunch (polarisation and orbit pilot bunches) and for the colliding bunches. (from [63])

of all unavoidable variations from the above assumption. For example, the fact that SR is proportional to E^4 amounts to a few keV correction, as can be seen in Fig. 34 [64]. Furthermore, other effects resulting from energy losses in quadrupoles and other lattice elements must be considered, since misalignment and field errors are unique for each element, resulting in variations between the electron and positron machines, and from one octant to another.

A second observation is also of interest, namely

$$E_J^+ - E_J^- = {E_0}^+ - {E_0}^- - 3\Delta E_{Arc,i} - 3\Delta E_{Arc,e} - 3\Delta_{BS} \ , \tag{25}$$

$$E_A^+ - E_A^- = {E_0}^+ - {E_0}^- - \Delta E_{Arc,i} - \Delta E_{Arc,e} - \Delta_{BS} \ . \tag{26}$$

As previously the boosts for points G (resp. D) are similar to those for J (resp. A), by exchanging the positive and negative particles. It is remarkable that the boost in point J and G represents, in addition to the (measured) difference between the average energies of the two beams, 3/4 (resp 1/4) of the total energy losses around the ring. The difference in boosts between the two pointsJ and G (resp. A and D) represent 3/4 (resp 1/4) of the sum of e^+ and e^- losses. The boosts can be measured from studying the topology of di-fermion events in the experiments, as summarised in chapter 8 of ref. [19] and Sec. 12. with a precision of $\pm 1.5 10^{-6}$ on the boost $x_\gamma \simeq (E^+ - E^-)/(E^+ + E^-)$.

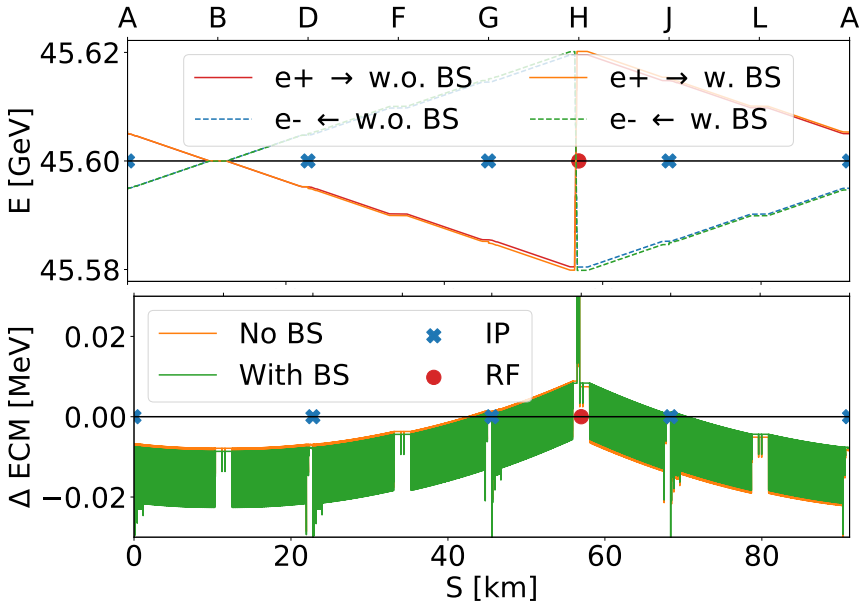

Figure 34: Beam energies (top) and E_{CM} (bottom) at the Z-pole with and without beamstrahlung (BS) at the IPs with a RF-section in PH [64].

11.2 Energy losses for pilot and colliding bunches

Continuous energy losses around the lattice occur from Synchrotron Radiation (SR), beamstrahlung and longitudinal impedance. The Colliding and non-colliding beams, having the same revolution frequency, and travelling through the same magnetic channel, have the same **average** energy, it's being given by the average of the energy over the guiding magnetic field. This **revolution frequency constraint**, RFC, for the case of a storage ring with RF acceleration situated in one single location, compensates many of the small differences arising between colliding and non-colliding beams when comparing the spin precession frequency to the collision energy. However, while SR losses are identical for pilot and colliding bunches, (40 MeV at 45.6 GeV), the beams do not have the same local energy.

Beamstrahlung at the collision points has several consequences.
Beamstrahlung energy losses have been estimated by D. Shatilov in [19] to be as large as 620 keV at full intensity at the Z pole. It was noted also that in itself it does not affect the center of mass energy, this energy loss being compensated by RF acceleration, given the RFC constraint.

Beamstrahlung modifies the energy spread and the bunch length. Longitudinal Impedance losses increase with increasing bunch intensity, and decrease with increasing bunch length (see Fig.33. The main contribution to longitudinal impedance stems from resistive wall impedance, which has recently been estimated at the Z-pole to be 0.8 MeV and 4.2 MeV per revolution, respectively, for 3×10^{10} and 2.6×10^{11} non-colliding bunch population. The Beamstrahlung-induced colliding bunch lengthening reduces the latter number from 4.2 MeV down to 1.6 MeV Further energy losses arise for colliding bunches from beamstrahlung and

are about 0.31 MeV per IP at the Z-pole The sum of all losses are compensated by the RF-cavities, where one crucial requirement is that all RF-cavities must be located in the same straight section.

The RFC constraint only works, of course, for a perfect machine, where the energy losses are spread symmetrically around the ring and at the same location for positrons and electrons. Given that the effects in question are as large as several MeV, i.e. three orders of magnitude larger that the target accuracy, it is essential to devise means of diagnosis and monitoring.

In equations 25 and 26 it was stressed that the centre of mass boost at the four IPs can be used to measure the energy losses.

The measurement of the average centre of mass boost in each of the IPs can be done using muon pairs as described in [19](Sec 8.1). The quantity $x_{\text{boost}} = \frac{E^- - E^+}{E^- + E^+}$ can be determined on an event by event basis[3] and the average extracted from the distribution shown in Fig. **??**. For a sample of 10^6 muon pair events and for a boost of 10^{-3},

$$\langle x_{\text{boost}} \rangle = (0.9991 \pm 0.0015) \times 10^{-3}, \tag{27}$$

which corresponds to a measurement of the energy difference with a precision of 140 keV. Such a sample can be collected in 600 seconds in each experiment at the Z pole in FCC-ee with the Feasibility Study luminosity of $140{\times}10^{34}/cm^2/s$. At the 88.6 and 93.9 GeV energy points, (spin tunes of 100.3 and 106.5 respectively), where the cross-section is lower, the required time to achieve this precision is longer, 2500 and 1600 seconds respectively. Integrated over a 'typical 8hr shift' (resp. the full duration of the run, with exposures of 10/ab, 31/ab, and 10/ab) in each experiment at the considered scan points, samples of 17, 85 and 29 10^6 (resp. 3, 43 and 5 10^9) muon pairs will be collected, providing statistical precisions on the local boost of 32, 15 and 26 keV (resp. 2.5, 0.7 and 2 keV) respectively. This high statistical precision on the boosts will be an effective way to monitor the stability of the system, and identify possible variations in the energy losses, and, by studying correlations with luminosity and other environmental parameters, help identify the sources of the energy losses.

NB: Here the measurement of the bunch length using the time distribution of interaction events (using any annihilation event) could be mentioned. Since all Z decays can be used, a resolution of 0.1% of 30 ps can be obtained in less than one minute.

11.3 Dispersion and collision offsets

11.3.1 Introduction

A potentially significant source of bias in the centre-of-mass energy determination arises from the combined effect of collision offset and opposite sign vertical dispersion (OSVD). For head-on collisions, *i.e.* without a crossing angle, the centre-of-mass energy shift is [19]

$$\Delta E_{CM} = -2u_0 \frac{\sigma_E (D_{u,B1} - D_{u,B2})}{E_0(\sigma_{B1}^2 + \sigma_{B2}^2)} \ , \tag{28}$$

[3]For historical reasons this quantity is noted x_γ in [19]

where the dispersion at the IP for both beams is $D_{u,B1,B2}$, and the beam-energy spread is σ_E assumed to be identical between electrons and positrons. Furthermore, are beam sizes $\sigma_{B1,B2}$, reference energy is E_0 and the transverse offset u_0. Assuming 1 µm OSVD at the IP and 0.13 % energy spread at 45.6 GeV beam energy, which are indicative values consistent with recent tuning studies, the collision energy is shifted by roughly 100 keV per nm offset ($\approx 0.03\,\sigma_y$). Reducing the centre-of-mass energy shift, therefore, requires minimising the collision offsets at the IPs and the OSVD. Because the beams collide at an angle in the horizontal plane, each beam samples the full energy distribution of the other; therefore the horizontal opposite sign dispersion creates a much smaller potential shift in the the centre-of-mass energy. We therefore restrict our discussion to vertical offsets.

The operational strategy proposed in Ref. [19] included regular (about once per hour) luminosity scans (varying the vertical collision offset) to measure the luminosity maximum and a possible vertical collision offset. By performing the same measurement for different RF frequencies, a measurement of the vertical dispersion at the IP can be obtained. At LEP this procedure was executed during data taking with large collisions offsets that reduced the luminosity by half. At FCC-ee this procedure might be risky because of the high beam charges and beam-beam tune shift, meaning that a reduced amplitude of collision offset should be employed.

11.3.2 Beam-beam deflection

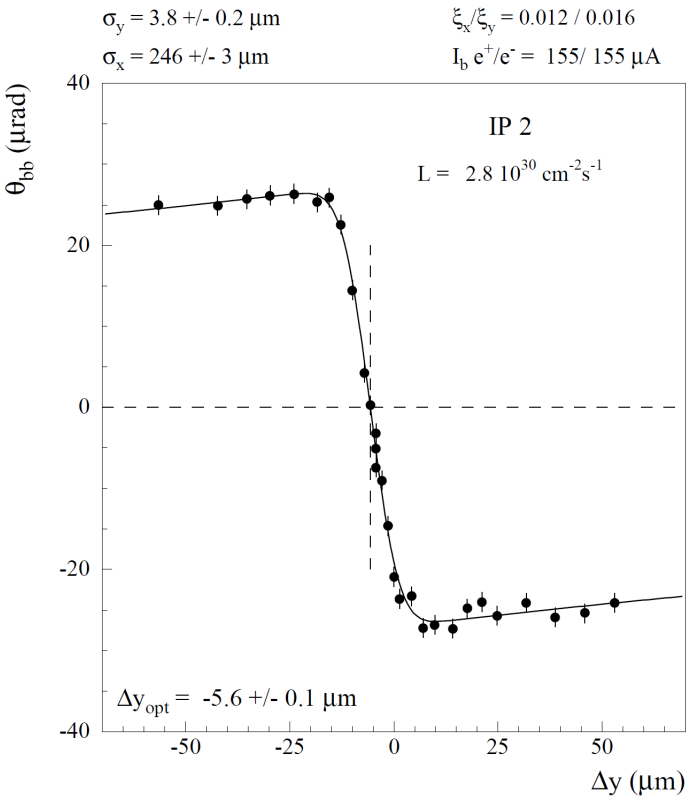

Figure 35: Beam-beam deflection scan performed at LEP in 1996 [65].

Giving the potential difficulty with luminosity scans, an alternative proposal is to measure the beam-beam deflection, rather than measuring the collision offset from a scan of the same parameter. The high bunch charge and small beam sizes open the possibility to monitor with great sensitivity the collision offsets, as had also been demonstrated at LEP [65]. An example measurement using this technique, showing the beam-beam kick versus beam separation is presented in Fig. 35. In the limit of collision offsets that are small compared with the beam size, the beam-beam kick ($\theta_{\rm bb}$) is proportional to the separation u according to

$$\Delta\theta_{\rm bb} = -\frac{4\pi\xi_u}{{\beta^*}_u}u. \tag{29}$$

Given typical FCC-ee parameters of beam-beam tune shift $\xi_y = 0.14$, ${\beta^*}_y = 0.8$ mm and $\sigma_y = 30$ nm, a vertical collision offset of 10 % of the vertical beam size (3 nm) will lead to a beam-beam deflection angle of 6.6μrad. The layout for a beam-beam deflection experiment is sketched on Fig. 36. We note that a beam-beam collision offset creates a distinctive pattern of movements of the beams, resulting in an orbit change.

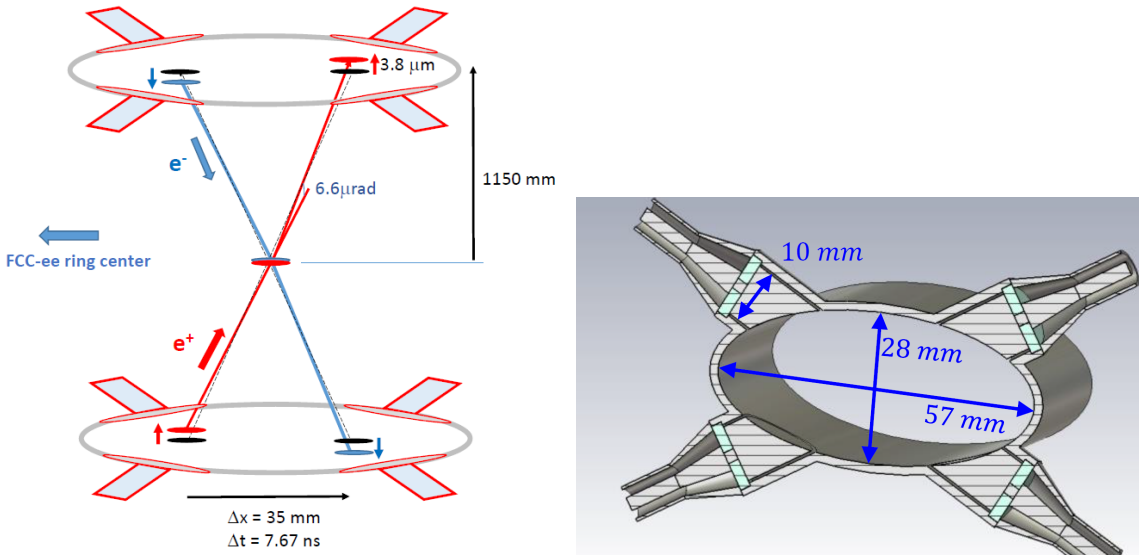

Figure 36: Sketch of the principle of the beam-beam deflection measurement at FCC-ee, by comparison of the vertical displacement of the colliding beams with respect to high intensity pilot bunches, as measured in the same Beam Position Monitors, shown on the right.

The intention is to measure the beam movements using the recently proposed LumiCal BPM pickups [66] located 1.15 m away from the interaction points, which could be installed directly behind the experimental luminosity monitors, as shown in Fig. 37. The beam-beam kick will lead to a shift in the beam position of 3.7 µm in each of the two BPMs. Assuming a BPM resolution of 1 μm for 10^8 bunch passages, which can be acquired in 3 seconds for the 10^4 bunches of each beam, the relative difference of 7.6μm between the e^+ and e^- bunches induced by the considered collision offset can be measured with a precision of 1μm, giving a precision of 0.4 nm on the collision offset (1.3 percent of the beam size).

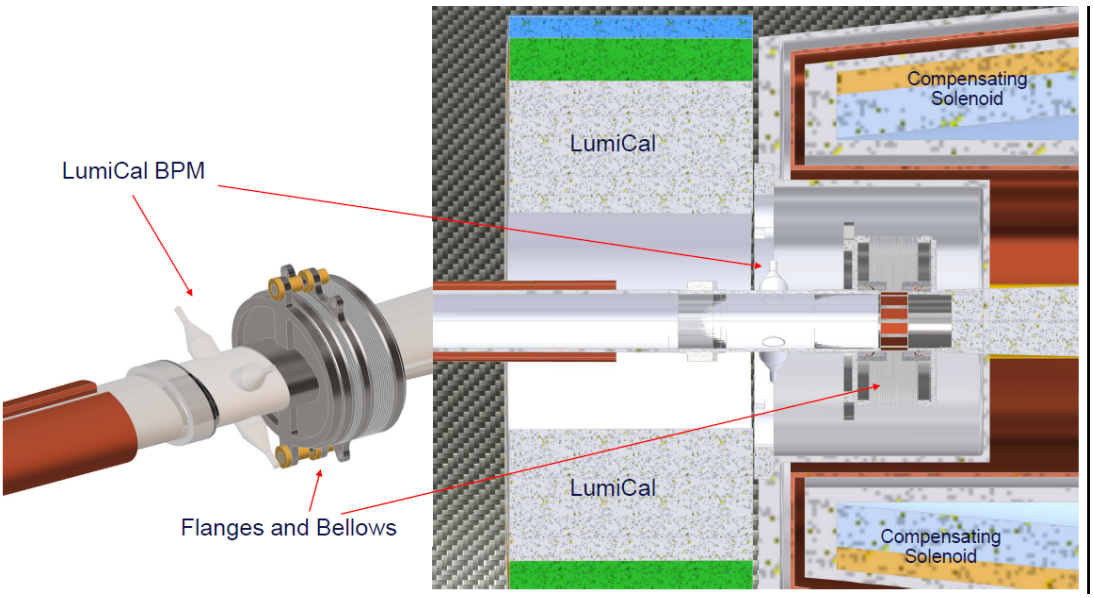

Figure 37: Proposed Lumical BPM location [66, 67].

In isolation this measurement is of limited use, since the two beams are circulating in two different rings with different imperfections. Hence a normalisation is necessary. Here two methods are under consideration:

1. Perform occasional studies of the relation between luminosity and the beam-beam collision offset using beam separator scans. This will provide a secure way of verifying that the maximum luminosity corresponds to a null collision offset. Separator scans have been discussed in [19].

2. Perhaps more promising is the use of dedicated, non-colliding, 'orbit' pilot bunches, with an intensity somewhat lower than that of the colliding bunches to ensure a similar longitudinal impedance. With these the beam position can be measured in the absence of beam-beam collisions. Assuming that 100 such bunches circulate in the machine, the time necessary to obtain a measurement of the collision offset with the above precision is about 15 minutes.

11.3.3 Opposite sign vertical dispersion measurement

The OSVD can be directly estimated by varying both beam energies with a modification of the revolution frequency. However, although this method was successful at LEP, the feasibility of performing this procedure during physics operation at FCC-ee remains to be demonstrated. Furthermore, this could lead to a cross-talk between the IPs, due to their individual collision offsets and OSVD, which remains to be investigated. For a modification of the energy by 10^{-3}, the above measurement of collision offsets with a precision of 0.4 nm corresponds to a measurement of OSVD with a precision of $\pm 0.6\,\mu$m, or altogether a precision on the combined effect of collision offsets and OSVD on the centre-of-mass energy with an accuracy of 20 keV every 30 minutes. If a four times smaller relative excursion of energy of 2.5×10^{-4} is preferred, the same result will be obtained after 16 such measurements,

providing a precision of 20 keV on the centre-of-mass energy every 8 hours, which would constitute a perfectly acceptable solution.

It has recently been proposed to use the horizontal orbit correctors to modify the path length, an an alternative to adjusting the RF frequency. This technique could only be performed on non-colliding pilot bunches. It would therefore be necessary to assume that these pilots possess the same OSVD as the colliding bunches.

11.3.4 Discussion and requirements

The above estimates assume implicitly that the movements of the beam are independent between interaction points, which is certainly not the case, since the beam-beam interaction generated by a collision offset at one IP will certainly generate a beam motion all around the ring, and in particular at the other IPs. Deciphering the source of the observed beam-beam kicks and thus correcting them will require the development of a correction procedure involving all four IPs, probably using as input the BPM readings of both colliding and non-colliding bunches. This procedure is likely to require dedicated correction knobs to adjust both the vertical beam positions and the vertical dispersion at the IP with the a resolution of, typically, one tenth of the expected statistical precision, *i.e.* 0.04 nm (position) and 0.4 μm (dispersion).

In conclusion, the beam-beam deflection measurements give access to high-precision measurements of the collision offsets, as well as a unique measurement of the opposite sign vertical dispersion at the interaction points. The availability of high precision BPMs at a location where they can measure both beams at once is essential. The feasibility of regular energy shifts of 2.5×10^{-4} will be required for the measurement of OSVD.

12 Input from the experiments

The experiments operating at FCC-ee will themselves provide measurements that are essential input to the calibration of the collision energy and related quantities. A full discussion of these measurements can be found in Ref. [19]. Here, a brief summary is given, together with some recent updates. The principal data set for performing these measurements is the very large sample of dimuon events that each experiment will collect, arising from the process $e^+e^- \to \mu^+\mu^-(\gamma)$, where γ indicates the possible presence of initial-state radiation (ISR). Analysis of the topology of these events, constrained by the total energy and momentum conservation in the final state, allows several important quantities to be determined. This analysis is, in general, based on the knowledge of the muon directions, which in turn imposes demands on the performance of the tracking system.

12.1 The crossing angle α

The nominal value of the crossing angle is $\alpha = 30\,\text{mrad}$, but the true value must be determined throughout data-taking so that the collision energy can be calculated to the required precision. At the Z pole, more than 10^6 dimuon events will be collected every 10 minutes in each detector, which will allow this parameter to be measured with a statistical uncertainty of 0.3 μrad, which is sufficient for the physics goals, since a precision of 15 μrad leads to an

uncertainty of 10 keV on E_{CM}. The statistical precision will be worse at higher energies, where the production rate is lower, but will not compromise the physics measurements that are targeted in these regimes.

There is an important subtlety in the crossing-angle determination that must be accounted for. The electron and positron bunches experience mutual electric and magnetic fields that accelerate (decelerate) the bunches before (after) the collision and also increase (decrease) the crossing angle. The collision energy is invariant, but the change in crossing angle from this effect (estimated to be a relative 0.6% modification) must be known so that the measured crossing angle can be corrected back to the unaffected quantity and used together with beam energies as determined from RDP to calculate E_{CM}.

The magnitude of the variation in α depends on parameters such as the bunch population and the spread in collision energy $\delta_{E_{\mathrm{CM}}}$. It is found empirically, from simulation studies, that α is proportional to $\mathcal{L}^{1/2} \,/\, {\delta_{E_{\mathrm{CM}}}}^{1/6}$. By measuring $\mathcal{L}$, α, and $\delta_{E_{\mathrm{CM}}}$ from dimuon events for different bunch intensities, it will be possible to extrapolate to zero intensity and determine the value of α in the absence of these effects. A good opportunity to perform these measurements would be in the period that top-up injection is taking place. It is therefore important that the detector can operate during this period and that the beams are stable. A simulated study of the measurement of α against $\mathcal{L}^{1/2} \,/\, {\delta_{E_{\mathrm{CM}}}}^{1/6}$ is presented in Fig. 38.

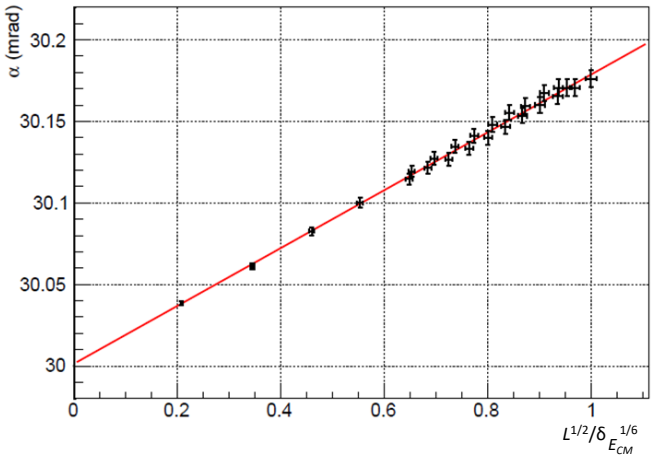

Figure 38: Change in the measured crossing-angle α vs. $\mathcal{L}^{1/2} \,/\, {\delta_{E_{\mathrm{CM}}}}^{1/6}$, at various points during the top-up injection. Extrapolation down to $\mathcal{L}^{1/2} \,/\, {\delta_{E_{\mathrm{CM}}}}^{1/6} = 0$ allows the crossing-angle to be determined in the absence of bunch-bunch effects [19].

12.2 The longitudinal boost and the collision-energy spread

The dimuon topology allows the longitudinal boost to be determined on an event-by-event basis. When averaged over a suitable sample size, this provides invaluable information to constrain the model of the energy loss around the ring and to calculate the local collision energy at each interaction point. The width of this distribution (Fig. 39) is a measure of $\delta_{E_{\mathrm{CM}}}$, which is an essential input to the measurement of certain observables, such as the Z

mass and widths. Again, the foreseen statistical precision on these quantities is excellent. For example, the energy spread can be measured to one part in a thousand with one million dimuon events. Recent work [68] has investigated how sensitive the determination of $\delta_{E_{\mathrm{CM}}}$ is to the knowledge of the ISR corrections in dimuon production. The conclusion is that the measurement is robust; even if it is assumed that the second-order corrections from ISR are unknown (which is not the case), the resulting bias on the extraction of $\delta_{E_{\mathrm{CM}}}$ is far smaller than the statistical uncertainty.

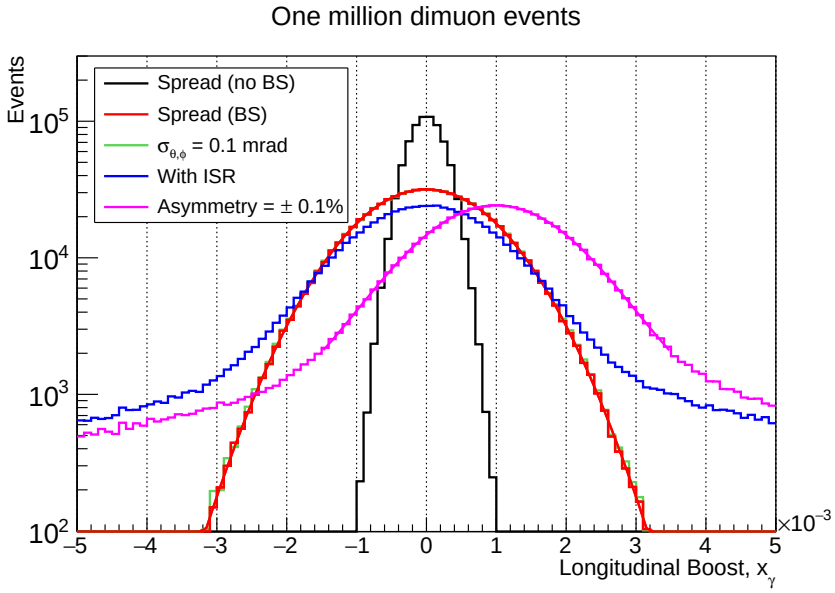

Figure 39: Fitted value of longitudinal boost from one million dimuon events at one of the FCC-ee IPs [19]. Once the ISR is unfolded, this distribution can be used to measure the energy spread. The magenta line shows the impact of a centre-of-mass boost on the distribution. The shift can be measured with a statistical precision of 40 keV. The other curves indicate the impact of beamstrahlung, angular resolution on the track directions, and ISR.

12.3 Relative E_{CM} determination in the Z-resonance scan

The reconstructed peak position of the dimuon invariant-mass distribution provides an excellent proxy for the collision energy. The difference in this reconstructed position between the points of the Z-resonance scan provides a measure of the change in collision energy, which is a critical input for several analyses, in particular the measurement of the Z boson width. The distribution is fitted in bins of the polar angle for back-to-back events. An example fit is shown in Fig. 40 (left). The statistical precision on this pseudo-E_{CM} measurement, when summing the samples from four experiments, is around 20 keV for each of the two off-peak running points, assuming the momentum resolution of the IDEA detector. The momentum scale stability must be controlled at this level, so that the detector does not introduce a bias in the measurement larger than the statistical precision.

The field stability can be tracked with NMR probes and the momentum scale can be

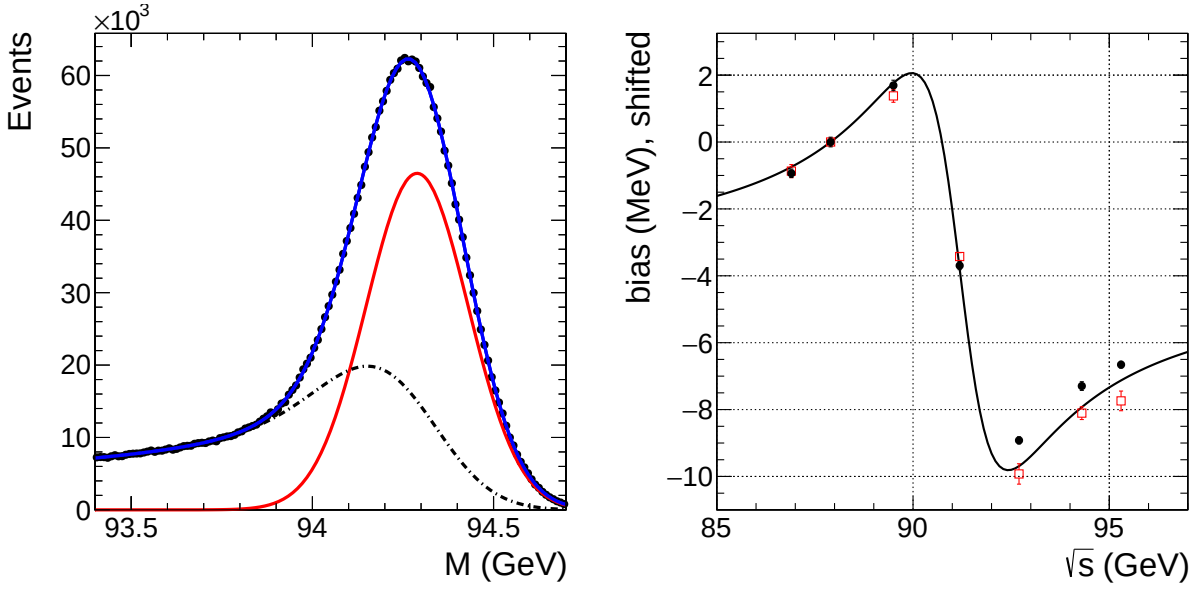

Figure 40: Left: Example fit to the dimuon invariant-mass distribution at $E_{\mathrm{CM}} = 94.3\,\mathrm{GeV}$, where the peak is modelled with the superposition (blue) of a Gaussian function (red) and two exponential functions (black). Right: The difference (bias) between the E_{CM} extracted from the dimuon invariant-mass fit and the true value. Results are shown for the simulated performance of the IDEA detector (red points) and for the expected dependence, including (black points) or not (black curve) ISR/FSR effects. Each set of results also has an overall overset of a few MeV, which is energy independent and, hence, not relevant for the determination of the Z width. A single shift has been applied to the bias, to correct for these offsets, so that the bias is zero at 87.9 GeV, for all sets of results.

directly monitored through the reconstruction of low-mass resonances. However, even with a perfect detector, there is a bias in the pseudo-E_{CM} measurement in the Z resonance scan arising from ISR/FSR effects, and from the product of the Breit–Wigner shape of the resonance and the Gaussian distribution of the energy spread of the colliding beams. The value of this bias varies by about 8 MeV when going from $E_{\mathrm{CM}} = 87.9$ to 94.3 GeV, as can be seen in Fig. 40 (right). This difference must be corrected for in the measurement, which requires a good understanding of the ISR/FSR effects. In a generator-level study, disabling ISR/FSR changes the difference in the bias between the two off-peak points by around 500 keV. Therefore, the theoretical prediction of these ISR/FSR effects to the 1% level would be sufficient to render their impact negligible for the Z-width measurement.

12.4 Absolute E_{CM} determination

At collision energies above the Z boson mass, the dimuon events may be used to provide an absolute measurement of E_{CM}. Radiative returns, in which the emission of an initial-state photon means that the dimuon has the Z mass, allows for the calibration of events unaffected by ISR. The method can be extended to also include multihadron final states. This method can be calibrated at the W-pair production threshold with RDP, and is of

great value for physics studies in the regime where no RDP is possible, i.e., collision energies above 200 GeV. This approach also provides a useful complementary measurement of E_{CM} in the intermediate energies where RDP is possible but challenging. The foreseen statistical uncertainty is around 280 keV for 6 ab^{-1} of integrated luminosity at $E_{\mathrm{CM}} = 125$ GeV and 260 keV for 20 ab^{-1} at $E_{\mathrm{CM}} = 160$ GeV. The performance of the tracking system must be sufficiently good that the precision is not compromised.

13 Expected precision on EW observables from the collision energy and its spread

Several of the most important electroweak observables are expected to have a dominant or significant systematic uncertainty associated with the knowledge of the collision energy and collision-energy spread. The collision-energy uncertainties can be classed in three distinct categories, itemised below. These uncertainties propagate to the physics results in an observable-dependent manner, as discussed in Ref. [19].

- Uncertainties that are fully correlated between measurements propagate to the knowledge of the absolute energy scale. Examples include the values of the anomalous magnetic moment and the mass of the electron, the frequency of the RF system, and any other systematic biases that occurs at all times and all energies. At this stage in the studies, it is estimated that this uncertainty will be around 100 keV on the collision energy at the Z pole and 300 keV at the W^+W^- threshold. This contribution is expected to be the dominant systematic uncertainty in the measurements of the Z and W boson masses.

- A point-to-point contribution comprises biases that occur at all times, or lead to an average shift, but are different for each energy setting. The principal method of determining this uncertainty will be based on the dimuon invariant-mass distribution, as reconstructed by the experiments. The estimated magnitude of this uncorrelated uncertainty is 20 keV for each off-peak point of the Z-resonance scan. The understanding gained at the Z pole and complementary measurements will lead to a corresponding uncertainty of around 100 keV at the W^+W^- threshold. The point-to-point uncertainty is expected to be the dominant contribution in the measurement of the Z width.

- The uncertainty on each individual RDP measurement is dominated by an uncertainty that is set by the frequency of the polarimeter sampling or the size of the energy bins where the depolarisation can be located. A reasonable estimate of this uncertainty is 200 keV at the Z pole and 300 keV at the W^+W^- threshold. As this component is statistical in nature, its impact decreases with the square-root of the number of events. As it is planned to collect $\sim 10^4$ measurements at each energy point, the final uncertainty from this source will be essentially negligible, compared to other contributions. However, the importance of making each measurement as precise as possible, and of collecting the largest possible number of measurements, will become more evident when the data set is split into smaller samples to perform systematic checks.

Table 4: Current projected E_{CM}-related uncertainties on selected electroweak observables.

	Observable				
Uncertainty	m_Z	Γ_Z	$\sin^2\theta_W^{\mathrm{eff}}$	$\frac{\Delta\alpha_{\mathrm{QED}}(m_Z^2)}{\alpha_{\mathrm{QED}}(m_Z^2)}$	m_W
Unit	keV	keV	$\times 10^{-6}$	$\times 10^{-5}$	keV
Absolute	100	2.5	–	0.1	150
Point-to-point	14	11	1.2	0.5	50
Sample size	1	1	0.1	–	3
Energy spread	–	5	–	0.1	–
Total E_{CM}-related	101	12	1.2	0.5	158
FCC-ee statistical	4	4	1.2	3.9	180

The contributions from each uncertainty category, and their quadratic sum, are listed in Table 4 for several key electroweak observables. This table also shows the contribution from the uncertainty in the knowledge of the energy spread, which affects quantities with a strong quadratic dependence on the collision energy. Observables that are most susceptible to this uncertainty include the Z cross section and the Z width. A collision-energy spread of 70 MeV, determined with a precision of $\pm\,0.05$ MeV, leads to a sub-dominant systematic uncertainty in the measurement of these observables.

With the current expectations, it will be possible to reduce the uncertainty from energy-related quantities by an order of magnitude or more with respect to what was achieved at LEP, such that they will be smaller than, or similar to, the statistical uncertainty for all observables apart from m_Z. Indeed, the entries in Table 4 for the E_{CM}-related systematic uncertainties can be compared to the corresponding LEP values of 1.7 MeV for m_Z, 1.2 MeV for Γ_Z, and 9 MeV for m_W.

14 Monochromatisation

One of the most fundamental outstanding measurements, since the Higgs boson discovery [69, 70], is determining its Yukawa couplings [71, 72]. Measuring the coupling of first-generation fermions presents significant experimental challenges due to their low masses and, consequently, small Yukawa couplings to Higgs fields. The measurement of this coupling is virtually impossible at hadron colliders because the $\mathrm{H} \to \mathrm{e^+e^-}$ decay has a tiny branching ratio, completely swamped by the Drell-Yan dielectron continuum with many orders of magnitude larger cross section. The FCC-ee, with unrivalled integrated luminosities of 10 ab^{-1} per year at 125 GeV could enable observing the resonant s-channel production of the scalar Higgs boson, namely the reaction $\mathrm{e^+e^-} \to \mathrm{H}$ on the Higgs pole [73, 74]. This possibility motivated physics [75] and accelerator studies [76, 77, 78, 79, 80, 81, 82, 83, 84] towards implementing this new operation mode.

Such a measurement is more easily feasible if the centre-of-mass (CM) energy spread of $\mathrm{e^+e^-}$ collisions, which is approximately 50 MeV due to energy spread from synchrotron radiation (SR) alone, and further enhanced by beamstrahlung, in a conventional collision

scheme, can be reduced to a level comparable to the natural width of the Standard Model Higgs boson $\Gamma_{\mathrm{H}} = 4.1$ MeV. To reduce the collision-energy spread and enhance the CM energy resolution in colliding-beam experiments, the concept of *monochromatisation* has long been proposed [85]. The basic idea consists of creating opposite correlations between spatial position and energy deviation within the colliding beams, which can be accomplished in beam-optics terms by introducing a non-zero dispersion function with opposite signs for the two beams at the interaction point (IP), as sketched in Fig. 41 for a crossing-angle configuration.

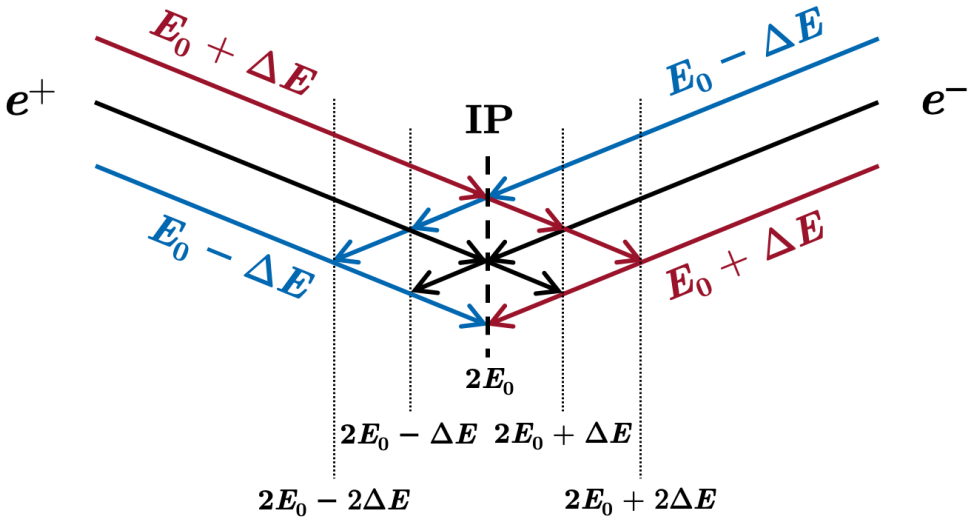

Figure 41: Schematic of crossing-angle collision with monochromatisation based on nonzero horizontal IP dispersion, showing trajectories at the nominal energy E_0 and with an energy offset of $\pm\Delta E$.

Taking as a starting point the GHC optics [86, 87, 88, 89], for the $\mathrm{t\bar{t}}$ mode, different monochromatisation schemes implying non-zero horizontal or vertical or both types of dispersion function at the IP ($D^*_{x,y}$) have been studied. All newly proposed IR optics has been designed to remain compatible with a standard operation mode without dispersion at the IP and also with the present tunnel configuration.

Given the presence of horizontal bending magnets in the vertical local chromaticity correction of the FCC-ee GHC Interaction Region (IR), the most natural way to implement monochromatisation in this FCC-ee lattice type is reconfiguring these IR dipoles so as to generate a non-zero D^*_x while maintaining the same crossing angle θ_c. Indeed, a wide σ^*_x helps mitigate the impact of the beamstrahlung (BS) on the energy spread σ_δ, while preserving a small σ^*_y is crucial for attaining high $\mathcal{L}$. Taking into account the baseline parameters for the FCC-ee GHC lattice with horizontal betatron sizes ($\sigma^*_{x,\beta} = \sqrt{\varepsilon_x \beta^*_x}$) at the IP of the order of 10 µm and a $\sigma_{\delta,SR}$ of ~ 0.05 % at s-channel Higgs production energy (∼125 GeV), a D^*_x of around 10 cm is required to achieve a monochromatisation factor (λ) of ∼5-8.

Because $\sigma^*_{y,\beta}$ ($\sim$ nm) $\ll \sigma^*_x$ (∼µm) for getting high luminosities, about 100 times smaller D^*_y ($\sim$ mm) is needed to get a similar λ. A nonzero D^*_y of this magnitude could be generated by simply using skew quadrupole correctors around the IP [90, 91, 92]. These quadrupoles

could be located close to the sextupole pairs in the IR.

As an illustration, a monochromatisation IR optics with combined 0.105 m of horizontal and 1 mm vertical IP dispersion) based on the FCC-ee GHC $t\bar{t}$ optics as starting point has been developed using MAD-X [93]. It is shown in Fig. 42. Different monochromatised beam-optics designs, including ones based on the lower-energy Z lattice, are detailed in Ref. [94].

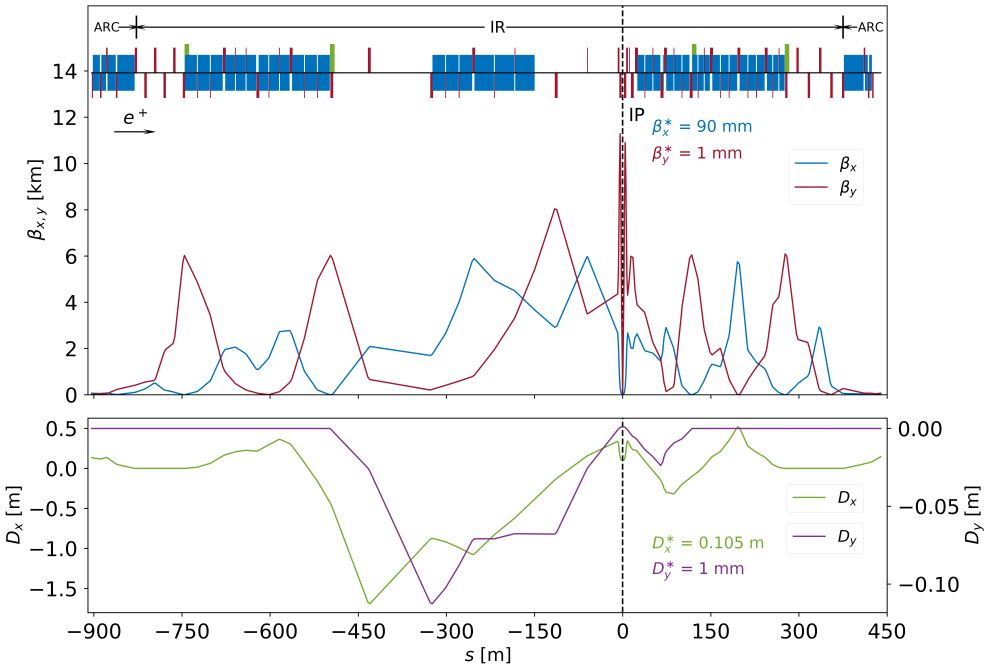

Figure 42: Monochromatisation IR lattices and optics with combined 0.105 m horizontal and 1 mm vertical IP dispersion, based on the FCC-ee GHC $t\bar{t}$ optics, developed using MAD-X. The beam direction is from left to right and the dashed line $s = 0$ marks the location of IP. In the lattice, dipoles, quadrupoles and sextupoles are shown in blue, red and green respectively, while focusing and defocusing elements are positioned above and below the orbit. In the optics, horizontal and vertical betatron functions are displayed in blue and red respectively, while horizontal and vertical dispersion functions are shown in green and purple, respectively.

After global implementation, the results of the analytical global performance evaluation for the monochromatisation IR optics based on the 'FCC-ee GHC $t\bar{t}$' are summarised in Table 5, for the crossing-angle configuration. Parameters due only to synchrotron radiation are marked with 'SR', while those including the impact of beamstrahlung are marked with 'BS'. For comparison, the first column labelled Standard ZES, presents an energy-scaled (ES) optics configuration. Its performance parameters were calculated after increasing the FCC-ee V22 $t\bar{t}$ optics from 45.6 GeV to 62.5 GeV, followed by completing all corrections and synchrotron radiation power loss compensation. The optics labelled MonochroM ZH4IP integrate the IP horizontal dispersion generation monochromatisation optics at all four IPs, while MonochroM ZH2IP does so at only two of the four IPs. The designation MonochroM

ZHS refers to the re-matched standard optics design that is orbit-compatible with the MonochroM ZH4IP optics. The number of bunches per beam n_b is constrained by the maximum beam-beam tune shift, taken to be 0.14, and by a minimum bunch spacing of 25 ns at FCC-ee. To select an appropriate n_b, studies optimising the luminosity per IP $\mathcal{L}$ and the CM energy spread σ_W of the MonochroM ZH4IP optics, as a function of n_b were conducted, including the beamstrahlung impact under the crossing-angle collision configuration.

Table 5: Global performance parameters of monochromatisation IR optics with nonzero horizontal IP dispersion based on the 'FCC-ee GHC $t\bar{t}$' optics under the crossing-angle configuration.

Parameter	[Unit]	Standard ZES	MonochroM ZH4IP	MonochroM ZH2IP	MonochroM ZHS
# of IPs n_{IP}		4			
Full crossing angle θ_c	[mrad]	30			
SR power / beam P_{SR}	[MW]	50	50	49	50
Beam energy E_0	[GeV]	62.5			
Energy loss / turn U_0	[GeV]	0.138	0.143	0.141	0.143
Beam Current I	[mA]	360	350	350	350
Bunches / beam n_b		12000			
Bunch population N_b	[10^{11}]	0.57	0.55	0.55	0.55
Hor. emittance (SR/BS) ε_x	[nm]	0.17 / 0.17	1.48 / 7.27	0.84 / 4.23	0.35 / 0.35
Vert. emittance (SR/BS) ε_y	[pm]	0.35 / 0.35	2.96 / 2.96	1.68 / 1.68	0.71 / 0.71
Mom. comp. factor α_{C}	[10^{-6}]	7.31	6.92	7.12	7.06
$\beta^*_{x/y}$	[mm]	1000 / 1.6	90 / 1	90 / 1	1000 / 1.6
$D^*_{x/y}$	[m]	0 / 0	0.105 / 0	0.105 / 0	0 / 0
Rel. en. spread (SR/BS) σ_δ	[%]	0.054 / 0.076	0.055 / 0.057	0.054 / 0.057	0.055 / 0.068
Bunch length (SR/BS) σ_z	[mm]	3.86 / 5.49	4.05 / 4.20	3.95 / 4.12	4.09 / 5.07
RF voltage 400/800 MHz V_{RF}	[GV]	0.170 / 0			
RF frequency (400MHz) f_{RF}	[MHz]	399.994581			
Synchrotron tune Q_s		0.015	0.014	0.014	0.014
Long. damping time τ_E/T_{rev}	[turns]	454	436	445	436
Hor. beam-beam (SR/BS) ξ_x		0.059 / 0.030	0.0025 / 0.0022	0.0027 / 0.0024	0.049 / 0.033
Vert. beam-beam (SR/BS) ξ_y		0.24 / 0.17	0.044 / 0.041	0.060 / 0.056	0.15 / 0.12
CM en. spread (SR/BS) σ_W	[MeV]	47.45 / 67.58	13.41 / 25.75	10.25 / 20.95	48.80 / 60.47
Luminosity / IP (SR/BS) $\mathcal{L}$	[10^{34}/(cm^{2}s)]	72.8 / 51.9	20.9 / 19.5	28.3 / 26.6	44.6 / 36.6

To accurately assess the performance of the FCC-ee monochromatisation IR optics, which features non-zero dispersion at the IP, the σ_W and luminosity per IP $\mathcal{L}$ were calculated for the different configurations using the simulation tool Guinea-Pig [95] and taking into account the impact of beamstrahlung. In these calculations, the particle distribution at the IP was modelled as an ideal Gaussian distribution, characterised by the global optical parameters of each optics configuration.

It is noted that while the physics performance of a nonzero-D^*_y scheme is less favourable, it would be easier to implement without altering the IR orbit, rendering it an attractive option for existing low-energy e^+e^- colliders. Without the ϵ_y blow-up due to BS, this scheme could potentially achieve better performance in such settings.

Looking ahead, the optical parameters for the monochromatisation mode will be further optimised for enhanced performance. Second, the dynamic aperture optimisation for these

new types of monochromatisation optics will be carried out step-by-step by adjusting arc sextupole families according to particle tracking results. This will allow beam-beam simulations with non-zero IP dispersion in the code XSUITE, incorporating the hourglass and BS effects rather than relying solely on analytical evaluations. Implementations of monochromatisation in more symmetric IRs, such as those in the FCC-ee LCC optics, will also be explored. Finally, studies are underway to validate the monochromatisation concept experimentally in existing low-energy circular e^+e^- colliders, such as BEPC II, DAΦNE, and SuperKEKB [96, 97, 98]. These efforts will be essential for achieving the full potential of monochromatisation in future collider projects.

15 Outlook

The studies performed before and during the Feasibility Study established a baseline scheme for calibration of the collision energy, ensuring that the physics goals of FCC-ee can be met. Nevertheless, these studies must be refined in certain areas and alternative schemes should be considered to further improve performance and operational efficiency.

The absolute uncertainties in E_{CM} arising from RDP are the dominant systematic uncertainties in the measurements of the Z and W masses. Future studies will investigate whether these uncertainties can be reduced beyond the currently assumed values: 100 keV at the Z pole and 150 keV at the W^+W^- threshold.

The measurements of energy-related quantities made by the experiments using dimuon events are a critical ingredient in the E_{CM} calibration, at all centre-of-mass energies. Recently, several of these studies have been deepened to validate their robustness with respect to the uncertainties in the knowledge of higher-order ISR/FSR effects; this work will be extended further. It is also important to consolidate the strategy for understanding how the measurement of the crossing angle is affected by changes in the bunch intensity. The impact of detector performance and the interplay with alignment studies will be another focus of attention. Finally, the use of other categories of physics events, beyond dimuons, will be investigated.

It is important to have a reliable procedure to accurately translate the mean beam energy, measured by RDP, to the local collision energy, relevant for the physics measurements. Full simulations of this procedure will be conducted, at each interaction point, incorporating the in-situ measurement of the longitudinal boosts of the collisions and the knowledge of the machine impedances. Attention will also be paid to the control of energy shifts from possible dispersion effects at each interaction point, as well as to the related requirements on the precision of the system of beam-position monitors.

More detailed simulations of the level and lifetime of transverse polarisation will be performed, in parallel with changes to account for any evolution in the proposed optics of the accelerator. A deeper understanding will be sought of any effects that might bias the assumed proportionality between the spin tune and the mean beam energy. It will be particularly important to monitor the expected level of polarisation at the W^+W^- threshold and the RDP strategy in this challenging regime. Detailed technical designs will be made of the polarimeter and depolariser systems.

So far, the baseline strategy to get transversally polarised pilot bunches has been to

inject unpolarised beams and to stimulate the growth of polarisation by activating wigglers at the start of each fill. This is a robust approach but has the disadvantage of introducing dead-time, during which no collisions are possible. To overcome this inconvenience, studies are underway to investigate the possibility of injecting already-polarised pilot bunches, for which the design of the injection system must be modified. When these studies are sufficiently advanced, it will be possible to decide whether the baseline strategy should be retained or updated in favour of the alternative approach.

Further investigations will also take place regarding the feasibility of the electron Yukawa measurement. In particular, new and refined schemes will be investigated with the aim of improving the monochromatisation of the collision energy. It will also be necessary to develop and simulate a procedure to monitor and adjust the collision energy in real time, to ensure that it remains centred at the Higgs pole. Further physics studies will be performed to improve the signal yield and the signal-to-background discrimination. Investigations will be performed to evaluate if the significance of the signal can be improved with differential measurements, accounting for the expected correlations between the monochromatisation and the longitudinal coordinate of the e^+e^- collision.

16 Summary

A strategy has been developed for the calibration of the centre-of-mass energy, and energy spread, with a precision that allows for a precise measurement of many important electroweak observables at FCC-ee. Further improvements will allow for even higher sensitivity to be gained, in particular for the Z width. This strategy has important consequences for machine operation, the necessary instrumentation and the measurements that are expected from the physics experiments themselves. Requirements are being formulated for critical items such as the depolariser and polarimeters. A set of goals is being defined for the next phase of the project.

17 Acknowledgements

FCCIS – The Future Circular Collider Innovation Study. This INFRADEV Research and Innovation Action project receives funding from the European Union's H2020 Framework program under grant agreement no. 951754. This work was performed under the auspices and with support from the Swiss Accelerator Research and Technology (CHART) program. Furthermore, the authors would like to thank E. Blomley and B. Härer for fruitful discussions. Z. Duan would like to thank A. Chance and B. Danela for sharing the high energy booster lattice files and error correction scripts, and A. Vanel for providing the energy ramp data.

References

[1] FCC Collaboration, Michael Benedikt et al. "Future Circular Collider Feasibility Study Report Volume 1: Physics, experiments, detectors". In: (2025). Submitted to the 2025–

2026 Update of the European Strategy for Particle Physics. DOI: 10.17181/CERN.9DKX.TDH9.

[2] FCC Collaboration, Michael Benedikt et al. "Future Circular Collider Feasibility Study Report Volume 2: Accelerators, technical infrastructure and safety". In: (2025). Submitted to the 2025–2026 Update of the European Strategy for Particle Physics. DOI: dx.doi.org/10.17181/CERN.EBAY.7W4X.

[3] R. Aßmann et al. "Calibration of center-of-mass energies at LEP-1 for precise measurements of Z properties". In: *Eur. Phys. J.* C6 (1999), pp. 187–223. DOI: 10.1007/s100529801030.

[4] V.V. Anashin et al. "Final analysis of KEDR data on J/ψ and ψ(2S) masses". In: *Phys. Lett. B* 749 (2015), p. 50. ISSN: 0370-2693. DOI: https://doi.org/10.1016/j.physletb.2015.07.057.

[5] I.M. Ternov, Y.M. Loskutov and L.I. Korovina. *Possibility of polarizing an electron beam by relativistic radiation in a magnetic field*. Sov. Phys. JETP, **14**, p. 921, 1962.

[6] A. A. Sokolov and I. M. Ternov. *On Polarization and spin effects in the theory of synchrotron radiation. Sov. Phys. Dokl.* **8** (1964) 1203–1205, http://inspirehep.net/record/918891/files/HEACC63_II_576-581.pdf. 1964.

[7] L. H. Thomas. "The Kinematics of an electron with an axis". In: *Phil. Mag. Ser.7* 3 (1927), pp. 1–21. DOI: 10.1080/14786440108564170.

[8] V. Bargmann, Louis Michel and V. L. Telegdi. "Precession of the polarization of particles moving in a homogeneous electromagnetic field". In: *Phys. Rev. Lett.* 2 (1959), pp. 435–436. DOI: 10.1103/PhysRevLett.2.435.

[9] Y. Wu. *Comparison of Harmonic Spin Matching Schemes using Orbit Bumps in the FCC-ee*. FCC Week 2023, London, UK, https://indico.cern.ch/event/1202105/contributions/5390923/attachments/2661382/4611071/FCC_Week_Yi.pdf. June 2023.

[10] Desmond Paul Barber and G Ripken. *Section 2.7.8 computing algorithms and spin matching, in Handbook of Accelerator Physics and Engineering, edited by A. W. Chao et al.,* (World Scientific, Singapore, 2006), 1st ed., 3rd printing. 2006.

[11] Desmond Paul Barber and G Ripken. *ection 2.6.7, computing algorithms for e-/e+ polarization in storage rings, in Handbook of Accelerator Physics and Engineering, edited by A. W. Chao et al.,* (World Scientific, Singapore, 2023), 3rd ed. 2023.

[12] R. Tomas et al. "Progress of the FCC-ee optics tuning working group". In: International Particle Accelerator Conference. presented at IPAC'23, Venice, Italy, May 2023, paper WEPL023, this conference. JACoW Publishing, Geneva, Switzerland.

[13] D. P. Barber et al. "High spin polarization at the HERA electron storage ring". In: *Nuclear Instruments and Methods in Physics Research Section A: Accelerators, Spectrometers, Detectors and Associated Equipment* 338.2-3 (1994), pp. 166–184.

[14] D. P. Barber et al. *A general harmonic spin matching formalism for the suppression of depolarisation caused by closed orbit distortion in electron storage rings*. Tech. rep. Deutsches Elektronen-Synchrotron (DESY), 1985.

[15] R. Rossmanith and R. Schmidt. "Compensation of depolarizing effects in electron-positron storage rings". In: *Nuclear Instruments and Methods in Physics Research Section A: Accelerators, Spectrometers, Detectors and Associated Equipment* 236.2 (1985), pp. 231–248.

[16] R. Schmidt. *Polarisationsuntersuchungen am Speicherring PETRA*. Tech. rep. DESY, 1982.

[17] RW Assmann. "Optimierung der transversalen Spin-Polarisation im LEP-Speicherring und Anwendung für Präzisionsmessungen am Z-Boson". PhD thesis. Munich U., 1994.

[18] Y. Wu et al. "Spin-polarization simulations for the Future Circular Collider e+e- using Bmad". In: International Particle Accelerator Conference. presented at IPAC'23, Venice, Italy, May 2023, paper MOPL055, this conference. JACoW Publishing, Geneva, Switzerland.

[19] Alain Blondel et al. "Polarization and Centre-of-mass Energy Calibration at FCC-ee". In: (Sept. 2019). arXiv: 1909.12245 [physics.acc-ph].

[20] John M Jowett and T M Taylor. "Wigglers for control of beam characteristics in LEP". In: *IEEE Trans. Nucl. Sci.* 30 (1983), pp. 2581–2583. DOI: 10.1109/TNS.1983.4332889. URL: https://cds.cern.ch/record/143604.

[21] Jack Heron. *Update of availability studies*. presented at the ATDC 16 availability and operation model meeting, 23 January 2025.

[22] J. Weninger. *Polarization transport from linac to booster*. https://indico.cern.ch/event/1513476/. Feb. 2025.

[23] T. et al Risselada. "Geometrical alignment and associated beam optics issues of transfer lines with horizontal and vertical deflection". In: *The Large Hadron Collider Project* (2004).

[24] Marcel Froissart and Raymond Stora. "Depolarisation d'un faisceau de protons polarises dans un synchrotron". In: *Nuclear Instruments and Methods* 7.3 (June 1960), pp. 297–305. ISSN: 0029554X. DOI: 10.1016/0029-554X(60)90033-1. (Visited on 04/05/2022).

[25] Z Duan. *Intrinsic spin resonances for FCC-ee Booster lattices*. 179th FCC-ee Optics Design Meeting & 50rd FCCIS WP2.2 Meeting, 23 Feb 2024.

[26] Tao Chen et al. "Booster free from spin resonance for future 100-km-scale circular e+e- colliders". In: *Physical Review Accelerators and Beams* 26 (2023), p. 051003. DOI: 10.1103/PhysRevAccelBeams.26.051003.

[27] Z Duan. *Imperfection spin resonances for FCC-ee Booster lattices*. 182nd FCC-ee Optics Design Meeting & 53rd FCCIS WP2.2 Meeting, 4 April 2024.

[28] E. D. Courant and R. D. Ruth. *The acceleration of polarized protons in circular accelerators*. BNL 51270, BNL, 1980.

[29] Ivan Koop. *Local bump depolarizer review*. presented at the FCC-FS EPOL group and FCCIS WP2.5 meeting 34, 7 November 2024.

[30] G. Iadarola et al. "Xsuite: An Integrated Beam Physics Simulation Framework". In: *Proc. 68th Adv. Beam Dyn. Workshop High-Intensity High-Brightness Hadron Beams (HB'23)* (Geneva, Switzerland, 9th–13th Oct. 2023). ICFA Advanced Beam Dynamics Workshop on High-Intensity and High-Brightness Hadron Beams 68. JACoW Publishing, Geneva, Switzerland, Apr. 2024, pp. 73–80. ISBN: 978-3-95450-253-0. DOI: 10.18429/JACoW-HB2023-TUA2I1. URL: https://jacow.org/hb2023/papers/tua2i1.pdf.

[31] V.I. Ptitsyn, Yu.M. Shatunov and S.R. Mane. "*Spin response formalism in circular accelerators*". In: *Nuclear Instruments and Methods in Physics Research Section A: Accelerators, Spectrometers, Detectors and Associated Equipment* 608.2 (2009), pp. 225–233. ISSN: 0168-9002. DOI: https://doi.org/10.1016/j.nima.2009.06.066. URL: https://www.sciencedirect.com/science/article/pii/S0168900209013333.

[32] Clara Kiel, Jacqueline Keintzel and Frank Zimmermann. "Modelling resonant depolarization". In: *to be preseted at the IPAC 2025*. 2025.

[33] V. Bargmann, Louis Michel and V. L. Telegdi. "Precession of the Polarization of Particles Moving in a Homogeneous Electromagnetic Field". In: *Phys. Rev. Lett.* 2 (10 May 1959), pp. 435–436. DOI: 10.1103/PhysRevLett.2.435. URL: https://link.aps.org/doi/10.1103/PhysRevLett.2.435.

[34] A. W. Chao. "Evaluation of Radiative Spin Polarization in an Electron Storage Ring". In: *Nucl. Instrum. Meth.* 180 (1981), p. 29. DOI: 10.1016/0029-554X(81)90006-9.

[35] E. D. Courant and R. D. Ruth. "The Acceleration of Polarized Protons in Circular Accelerators". In: *BNL-51270* (1980).

[36] N.Yu. Muchnoi. "Electron beam polarimeter and energy spectrometer". In: *Journal of Instrumentation* 17.10 (Oct. 2022), P10014. DOI: 10.1088/1748-0221/17/10/P10014. URL: https://dx.doi.org/10.1088/1748-0221/17/10/P10014.

[37] A. Martens, F. Mawas and F. Zomer. "A quantitative study of systematic uncertainties due to QED corrections in accurate Compton polarimetry experiments". In: *Journal of Instrumentation* 18.10 (Oct. 2023), P10001. DOI: 10.1088/1748-0221/18/10/P10001. URL: https://dx.doi.org/10.1088/1748-0221/18/10/P10001.

[38] R. Assmann et al. and The LEP Energy Working Group. "Calibration of centre-of-mass energies at LEP1 for precise measurements of Z properties". In: *The European Physical Journal C - Particles and Fields* 6.2 (Jan. 1999), pp. 187–223. ISSN: 1434-6052. DOI: 10.1007/s100529801030. URL: https://doi.org/10.1007/s100529801030.

[39] I. Koop. "Free Spin Precession as an Alternative to the Resonant Depolarization Method in Future Electron-Positron Colliders". In: *Physics of Particles and Nuclei Letters* 21.3 (2024), pp. 305–309. DOI: https://doi.org/10.1134/S154747712470016X.

[40] Nickolai Muchnoi. "FCC-ee polarimeter". In: (Mar. 2018). arXiv: 1803.09595 [physics.ins-det

[41] A. Narayan et al. "Precision Electron-Beam Polarimetry at 1 GeV Using Diamond Microstrip Detectors". In: *Phys. Rev. X* 6 (1 Feb. 2016), p. 011013. DOI: 10.1103/PhysRevX.6.011013. URL: https://link.aps.org/doi/10.1103/PhysRevX.6.011013.

[42] N. Vansteenkiste, P. Vignolo and A. Aspect. "Optical reversibility theorems for polarization: application to remote control of polarization". In: *J. Opt. Soc. Am. A* 10.10 (Oct. 1993), pp. 2240–2245. DOI: 10.1364/JOSAA.10.002240. URL: https://opg.optica.org/josaa/abstract.cfm?URI=josaa-10-10-2240.

[43] Luc Couturier et al. "Laser frequency stabilization using a commercial wavelength meter". In: *Review of Scientific Instruments* 89.4 (2018), p. 043103. DOI: 10.1063/1.5025537. eprint: https://doi.org/10.1063/1.5025537. URL: https://doi.org/10.1063/1.5025537.

[44] Etienne Cantin et al. "An accurate and robust metrological network for coherent optical frequency dissemination". In: *New Journal of Physics* 23.5 (May 2021), p. 053027. DOI: 10.1088/1367-2630/abe79e. URL: https://dx.doi.org/10.1088/1367-2630/abe79e.

[45] https://www.refimeve.fr/index.php/fr/presentation/com-allevents-settings/t-refimeve.html.

[46] L.J. Nevay et al. "BDSIM: An accelerator tracking code with particle–matter interactions". In: *Computer Physics Communications* 252 (2020), p. 107200. ISSN: 0010-4655. DOI: https://doi.org/10.1016/j.cpc.2020.107200. URL: https://www.sciencedirect.com/science/article/pii/S0010465520300400.

[47] D. Charlet et al. "Conceptual study of a Compton polarimeter for the upgrade of the SuperKEKB collider with a polarized electron beam". In: *JINST* 18.10 (2023), P10014. DOI: 10.1088/1748-0221/18/10/P10014.

[48] Adriana Simancas et al. "Simulations and performance studies of a MAPS in 65 nm CMOS imaging technology". In: *Nuclear Instruments and Methods in Physics Research Section A: Accelerators, Spectrometers, Detectors and Associated Equipment* 1064 (July 2024), p. 169414. ISSN: 0168-9002. DOI: 10.1016/j.nima.2024.169414. URL: http://dx.doi.org/10.1016/j.nima.2024.169414.

[49] J. List, A. Vauth and B. Vormwald. "A quartz Cherenkov detector for Compton-polarimetry at future e+e− colliders". In: *Journal of Instrumentation* 10.05 (May 2015), P05014. DOI: 10.1088/1748-0221/10/05/P05014. URL: https://dx.doi.org/10.1088/1748-0221/10/05/P05014.

[50] A. D. Bukin et al. "Absolute Calibration of Beam Energy in the Storage Ring. Phi-Meson Mass Measurement". In: *Proceedings, International symposium on high-energy and elementary particles: Warsaw, Poland, September 3-9, 1975*. 1975, pp. 138–147.

[51] A.A. Zholentz, L.M. Kurdadze, M.Yu. Lelchuk et al. "High precision measurement of the Ψ- and Ψ'-meson masses". In: *Phys. Lett. B* 96.1 (1980), pp. 214–216. ISSN: 0370-2693. DOI: 10.1016/0370-2693(80)90247-6. URL: https://www.sciencedirect.com/science/article/pii/0370269380902476.

[52] V. E. Blinov et al. "Beam Energy Measurement by Resonant Depolarization Method at VEPP-4M". In: *CERN-BINP Workshop for Young Scientists in e+e- Colliders*. 2017, pp. 109–118. DOI: 10.23727/CERN-Proceedings-2017-001.109.

[53] W. W. MacKay et al. "Measurement of the ϒ mass". In: *Phys. Rev. D* (June 1984), pp. 2483–2490. DOI: 10.1103/PhysRevD.29.2483. URL: https://link.aps.org/doi/10.1103/PhysRevD.29.2483.

[54] L Arnaudon et al. "Accurate determination of the LEP beam energy by resonant depolarization". In: *Z. Phys. C* 66 (1995), pp. 45–62. DOI: 10.1007/BF01496579. URL: https://cds.cern.ch/record/267514.

[55] V N Baier and V A Khoze. "Effects of Particle Scattering within a Beam of Polarized Electrons in a Storage Ring". In: *At. Energ. (USSR), 25: 440-2 (1968)* (Jan. 1968). DOI: 10.1007/BF01239705. URL: https://www.osti.gov/biblio/4821078.

[56] Tae-Yeon Lee, Jinhyuk Choi and H.S. Kang. "Simple determination of Touschek and beam-gas scattering lifetimes from a measured beam lifetime". In: *Nucl. Instr. Methods A* 554 (2005), pp. 85–91. ISSN: 0168-9002. DOI: doi.org/10.1016/j.nima.2005.08.049. URL: https://www.sciencedirect.com/science/article/pii/S0168900205016438.

[57] F. Zimmermann et al. "Probing FCC-ee energy calibration through resonant depolarization at KARA". English. In: *Proc. IPAC'24* (Nashville, TN). IPAC'24 - 15th International Particle Accelerator Conference 15. JACoW Publishing, Geneva, Switzerland, May 2024, pp. 2516–2519. ISBN: 978-3-95450-247-9. DOI: 10.18429/JACoW-IPAC2024-WEPR20. URL: https://indico.jacow.org/event/63/contributions/4464.

[58] E. Blomley et al. "Resonant spin depolarization at the test facility KARA: overview of recent efforts". English. In: *Proc. IPAC'24* (Nashville, TN). IPAC'24 - 15th International Particle Accelerator Conference 15. JACoW Publishing, Geneva, Switzerland, May 2024, pp. 2335–2338. ISBN: 978-3-95450-247-9. DOI: 10.18429/JACoW-IPAC2024-WEPG51. URL: https://indico.jacow.org/event/63/contributions/4343.

[59] J. Keintzel et al. "Investigations in turn-by-turn optics measurements at KARA". English. In: *Proc. IPAC'24* (Nashville, TN). IPAC'24 - 15th International Particle Accelerator Conference 15. JACoW Publishing, Geneva, Switzerland, May 2024, pp. 1294–1297. ISBN: 978-3-95450-247-9. DOI: 10.18429/JACoW-IPAC2024-TUPG33. URL: https://indico.jacow.org/event/63/contributions/3846.

[60] URL: https://docs.scipy.org.

[61] I Morozon, I Nikolaev and S Nikitin. *Updated version of depolarizer system concept for FCC-ee*. presented at the FCC-FS EPOL group and FCCIS WP2.5 meeting no. 24, 16 November 2023.

[62] J. Keintzel et al. "FCC-ee Lattice Design". In: *65th ICFA Adv. Beam Dyn. Workshop High Luminosity Circular e+ e- Colliders (eeFACT2022), Frascati, Italy, September 12-16, 2022* (Frascati, Italy,). ICFA Adv. Beam Dyn. Workshop 65. https://doi.org/10.18429/JAC eeFACT2022-TUYAT012. Geneva, Switzerland: JACoW Publishing, Feb. 2023, pp. 52–60. ISBN: 978-3-95450-236-3. DOI: doi:10.18429/JACoW-eeFACT2022-TUYAT012. URL: https://accelconf.web.cern.ch/eefact2022/papers/tuyat0102.pdf.

[63] E. Carideo et al. *Local energy deviations due to impedances - estimations and uncertainties*. Second FCC workshop on Polarization, center-of-mass energy calibration and monochromatization, https://indico.cern.ch/event/1181966/. Sept. 2022.

[64] J. Keintzel et al. "Centre-of-Mass Energy in FCC-ee". In: *Proc. IPAC'22* (Bangkok, Thailand). International Particle Accelerator Conference 13. JACoW Publishing, Geneva, Switzerland, July 2022, pp. 1683–1686. ISBN: 978-3-95-450227-1. DOI: 10.18429/JACoW-IPAC2022-WEPOST007. URL: https://jacow.org/IPAC2022/papers/WEPOST007.pdf.

[65] C. Bovet et al. "Luminosity optimization using beam-beam deflections at LEP". In: *Conf. Proc. C* 960610 (1996). Ed. by S. Myers et al., pp. 325–327.

[66] Manfred Wendt. *Challenges for the IR BPMs*. FCC Week 2023, London, UK, https://indico.cern.ch/event/1202105/. June 2023.

[67] Francesco Fransesini. *IR BPMs integration*. FCC-ee MDI meeting 47 and FCCIS WP2.3 meeting 18, https://indico.cern.ch/event/1292318/. July 2023.

[68] Kazanecki, Michal. *Impact of the uncertainty in the ISR prediction on determination of $\sqrt{s}$ energy spread using dimuon events*. FCC Physics Performance meeting, 16 September 2024. 2024. URL: https://indico.cern.ch/event/1453429/.

[69] Georges Aad et al. "Observation of a new particle in the search for the Standard Model Higgs boson with the ATLAS detector at the LHC". In: *Phys. Lett. B* 716 (2012), pp. 1–29. DOI: 10.1016/j.physletb.2012.08.020. arXiv: 1207.7214 [hep-ex].

[70] Serguei Chatrchyan et al. "Observation of a New Boson at a Mass of 125 GeV with the CMS Experiment at the LHC". In: *Phys. Lett. B* 716 (2012), pp. 30–61. DOI: 10.1016/j.physletb.2012.08.021. arXiv: 1207.7235 [hep-ex].

[71] A. Abada et al. "FCC Physics Opportunities: Future Circular Collider Conceptual Design Report Volume 1". In: *Eur. Phys. J. C* 79.6 (2019), p. 474. DOI: 10.1140/epjc/s10052-019-6904-3.

[72] A. Abada et al. "FCC-ee: The Lepton Collider: Future Cirular Collider Conceptual Design Report Volume 2". In: *Eur. Phys. J. ST* 228.2 (2019), pp. 261–623. DOI: 10.1140/epjst/e2019-900045-4.

[73] David d'Enterria. "Higgs physics at the Future Circular Collider". In: *PoS* ICHEP2016 (2017), p. 434. DOI: 10.22323/1.282.0434. arXiv: 1701.02663 [hep-ex].

[74] Wolfgang Altmannshofer, Joachim Brod and Martin Schmaltz. "Experimental constraints on the coupling of the Higgs boson to electrons". In: *JHEP* 05 (2015), p. 125. DOI: 10.1007/JHEP05(2015)125. arXiv: 1503.04830 [hep-ph].

[75] David d'Enterria, Andres Poldaru and George Wojcik. "Measuring the electron Yukawa coupling via resonant s-channel Higgs production at FCC-ee". In: *Eur. Phys. J. Plus* 137.2 (2022), p. 201. DOI: 10.1140/epjp/s13360-021-02204-2. arXiv: 2107.02686 [hep-ex].

[76] Marco Alan Valdivia García, Angeles Faus-Golfe and Frank Zimmermann. *Towards a Monochromatization Scheme for Direct Higgs Production at FCC-ee. in Proc.* 7th International Particle Accelerator Conference, IPAC'16, Busan, Korea. 2016. DOI: 10.18429/JACoW-IPAC2016-WEPMW009.

[77] Marco Alan Valdivia García and Frank Zimmermann. "Towards an Optimized Monochromatization for direct Higgs Production in Future Circular e^+e^- Colliders". In: *CERN-BINP Workshop for Young Scientists in e^+e^- Colliders*. 2017, pp. 1–12. DOI: 10.23727/CERN-Proceedings-2017-001.1.

[78] Marco Alan Valdivia García and Frank Zimmermann. *Optimized Monochromatization for Direct Higgs Production in Future Circular e^+e^- Colliders. in Proc.* 8th International Particle Accelerator Conference, IPAC'17, Copenhagen, Denmark. May 2017. DOI: 10.18429/JACoW-IPAC2017-WEPIK015.

[79] H. Jiang et al. "Update on the monochromatization studies". In: *FCC-FS EPOL group and FCCIS WP2.5 meeting 4*. Jan. 2022. URL: https://indico.cern.ch/event/1108961/.

[80] Angeles Faus-Golfe, Marco Alan Valdivia García and Frank Zimmermann. "The challenge of monochromatization: direct s-channel Higgs production: $e^+e^- \to H$". In: *Eur. Phys. J. Plus* 137.1 (2022), p. 31. DOI: 10.1140/epjp/s13360-021-02151-y.

[81] Hongping Jiang et al. "First optics design for a transverse monochromatic scheme for the direct s-channel Higgs production at FCC-ee collider". In: *JACoW* IPAC2022 (2022), pp. 1878–1880. DOI: 10.18429/JACoW-IPAC2022-WEPOPT017.

[82] Zhandong Zhang et al. "Monochromatization Interaction Region Optics Design for Direct s-channel production at FCC-ee". In: *JACoW* IPAC2023 (2023), MOPL079. DOI: 10.18429/JACoW-IPAC2023-MOPL079.

[83] Zhandong Zhang et al. "Update in the optics design of monochromatization interaction region for direct Higgs s-channel production at FCC-ee". In: *JACoW* IPAC2024 (2024), WEPR21. DOI: 10.18429/JACoW-IPAC2024-WEPR21.

[84] Angeles Faus-Golfe. "Monochromatization a new operation mode for e^+e^- circular colliders". In: *Proc. IPAC'24* (Nashville, TN). May 2024. URL: https://indico.jacow.org/event/63/contributions/3067/.

[85] A. Renieri. *Possibility of Achieving Very High-Energy Resolution in electron-Positron Storage Rings*. Tech. rep. LNF-75/6-R. LNF, Feb. 1975.

[86] K. Oide et al. "Design of beam optics for the Future Circular Collider e^+e^- collider rings". In: *Phys. Rev. Accel. Beams* 19.11 (2016). [Addendum: Phys.Rev.Accel.Beams 20, 049901 (2017)], p. 111005. DOI: 10.1103/PhysRevAccelBeams.19.111005. arXiv: 1610.07170 [physics.acc-ph].

[87] Katsunobu Oide. "IR optics for FCC-ee". In: *Proc. FCC-EIC Joint & MDI Workshop* (Geneva, Switzerland). Oct. 2022. URL: https://indico.cern.ch/event/1186798/contributions/5062582/.

[88] Jacqueline Keintzel et al. "FCC-ee Lattice Design". In: *JACoW* eeFACT2022 (2023), pp. 52–60. DOI: 10.18429/JACoW-eeFACT2022-TUYAT0102.

[89] *CERN optics repository*. https://acc-models.web.cern.ch/acc-models/fcc/.

[90] Pantaleo Ramondi. "Final Focus design with local compensation of geometric and chromatic aberrations". In: *Proc. FCCIS 2022 Workshop* (CERN). Dec. 2022. URL: https://indico.cern.ch/event/1203316/contributions/5156515/.

[91] Pantaleo Ramondi. "Alternative optics and variants". In: *Proc. FCCIS 2023 WP2 Workshop* (Roma, Italy). Nov. 2023. URL: https://indico.cern.ch/event/1326738/contributions/5654524/.

[92] Andrea Ciarma et al. "Alternative solenoid compensation scheme for the FCC-ee interaction region". In: *JACoW* IPAC2024 (2024), TUPC68. DOI: 10.18429/JACoW-IPAC2024-TUPC68.

[93] *MAD - Methodical Accelerator Design*. https://mad.web.cern.ch/mad/.

[94] Zhandong Zhang et al. "Monochromatization interaction region optics design for direct s-channel Higgs production at FCC-ee". In: (2024). arXiv: 2411.04210v1 [physics.acc-ph].

[95] D. Schulte. "Beam-beam simulations with Guinea-Pig". In: *eConf* C980914 (1998). Ed. by Kwok Ko and Robert D. Ryne, pp. 127–131.

[96] Institute of High Energy Physics, Beijing. *BEPCII Design Report*. Beijing, China, 2009.

[97] C. Milardi, M. Preger and P. Raimondi. *The DAFNE interaction region for the KLOE-2 run*. Mar. 2010.

[98] Yukiyoshi Ohnishi et al. "Accelerator design at SuperKEKB". In: *PTEP* 2013 (2013), 03A011. DOI: 10.1093/ptep/pts083.